Prifysgol Abertawe
Swansea University

Design and Implementation of Control Techniques of Power Electronic Interfaces for Photovoltaic Power Systems:

Cascade PI Controller-Based Model Reference Adaptive Control, Notch Filter Dynamics-based PR-P Controller Designed by Symmetrical Pole Placement Method, Extremum Seeking Adaptive Control

Cagfer Yanarates

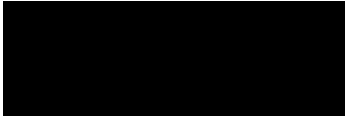Submitted to Swansea University in Partial fulfilment of the requirements for the Degree of Doctor of Philosophy
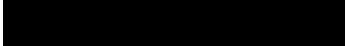
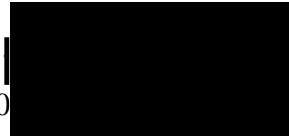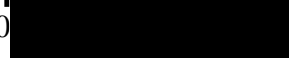Swansea University, Swansea, UK

May 2022

Declaration of authorship

This work has not previously been accepted in substance for any degree and is not being concurrently submitted in candidature for any degree.
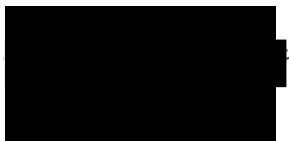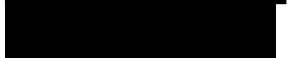
Signed: ███████████ candidate)
Date: 05/ ██████████

This thesis is the result of my own investigations, except where otherwise stated. Where correction services have been used, the extent and nature of the correction is clearly marked in a footnote(s).

Other sources are acknowledged by footnotes giving explicit references. A bibliography is appended.

Signed: ████████████ (candidate)
Date: 05/0 ███████

I hereby give consent for my thesis, if accepted, to be available for photocopying and for inter-library loan, and for the title and summary to be made available to outside organisations.

Signed: ████████████ (candidate)
Date: 05/ ████████

The University's ethical procedures have been followed and, where appropriate, that ethical approval has been granted.

Signed: ████████████ (candidate)
Date: 05/ ████████

Abstract

The aim of this thesis is to scrutinize and develop four state-of-the-art power electronics converter control techniques utilized in various photovoltaic (PV) power conversion schemes accounting for maximum power extraction and efficiency.

First, Cascade Proportional and Integral (PI) Controller-Based Robust Model Reference Adaptive Control (MRAC) of a DC-DC boost converter has been designed and investigated. Non-minimum phase behaviour of the boost converter due to right half plane zero constitutes a challenge and its non-linear dynamics complicate the control process while operating in continuous conduction mode (CCM). The proposed control scheme efficiently resolved complications and challenges by using features of cascade PI control loop in combination with properties of MRAC. The accuracy of the proposed control system's ability to track the desired signals and regulate the plant process variables in the most beneficial and optimised way without delay and overshoot is verified. The experimental results and analysis reveal that the proposed control strategy enhanced the tracking speed two times with considerably improved disturbance rejection.

Second, (P)roportional Gain (R)esonant and Gain Scheduled (P)roportional (PR-P) Controller has been designed and investigated. The aim of this controller is to create a variable perturbation size real-time adaptive perturb and observe (P&O) maximum power point tracking (MPPT) algorithm. The proposed control scheme resolved the drawbacks of conventional P&O MPPT method associated with the use of constant perturbation size that leads to a poor transient response and high continuous steady-state oscillations. The prime objective of using the PR-P controller is to utilize inherited properties of the signal produced by the controller's resonant path and integrate it to update best estimated perturbation that represents the working principle of extremum seeking control (ESC) to use in a P&O algorithm that characterizes the overall system learning-based real time adaptive (RTA). Additionally, utilization of internal dynamics of the PR-P controller overcome the challenges namely, complexity, computational burden, implantation cost and slow tracking performance in association with commonly used soft computing intelligent systems and adaptive control strategies. The experimental results and analysis reveal that the proposed control

strategy enhanced the tracking speed five times with reduced steady-state oscillations around maximum power point (MPP) and more than 99% energy extracting efficiency.

Third, the interleaved buck converter based photovoltaic (PV) emulator current control has been investigated. A proportional-resonant-proportional (PR-P) controller is designed to resolve the drawbacks of conventional PI controllers in terms of phase management which means balancing currents evenly between active phases to avoid thermally stressing and provide optimal ripple cancellation in the presence of parameter uncertainties. The proposed controller shows superior performance in terms of 10 times faster-converging transient response, zero steady-state error with significant reduction in current ripple. Equal load sharing that constitutes the primary concern in multi-phase converters has been achieved with the proposed controller. Implementing of robust control theory involving comprehensive time and frequency domain analysis reveals 13% improvement in the robust stability margin and 12-degree bigger phase toleration with the PR-P controller.

Fourth, a symmetrical pole placement Method-based Unity Proportional Gain Resonant and Gain Scheduled Proportional (PR-P) Controller has been designed and investigated. The proposed PR-P controller resolved the issues associated with the use of the PI controller which are tracking repeating control input signal with zero steady-state and mitigating the 3rd order harmonic component injected into the grid for single-phase PV systems. Additionally, the PR-P controller has overcome the drawbacks of frequency detuning in the grid and increase in the magnitude of odd number harmonics in the system that constitute the common concerns in the implementation of conventional PR controller. Moreover, the unprecedented design process based on changing notch filter dynamics with symmetrical pole placement around resonant frequency overcomes the limitations that are essentially complexity and dependency on the precisely modelled system.

The verification and validation process of the proposed control schemes has been conducted using MATLAB/Simulink and implementing MATLAB/Simulink/State flow on dSPACE Real-time-interface (RTI) 1007 processor, DS2004 High-Speed A/D and CP4002 Timing and Digital I/O boards.

Acknowledgement

First and foremost, as someone who has adopted the saying " Science is the only true guide in life" as principle, I would like to convey my sincere gratitude and appreciation to the Republic of Turkey, Ministry of National Education for Graduate Education Scholarship (YLSY).

I would like to say a special thank you to my supervisor, Dr. Zhongfu Zhou, who enabled me to complete this thesis with his patience, motivation, enthusism and immense knowledge. His expertise and assistance helped me get through all of the tough stages of my PhD degree quickly and efficiently.

Finally, I would like to thank my family for supporting me during the compilation of this dissertation. I am very thankfull for all opportunities that appear in my life and thanks for everyone, better or worse, who had contributed a lot to my progress.

List of contributions

Publications

C. Yanarates and Z. Zhou, "Symmetrical Pole Placement Method-Based Unity Proportional Gain Resonant and Gain Scheduled Proportional (PR-P) Controller With Harmonic Compensator for Single Phase Grid-Connected PV Inverters," in IEEE Access, vol. 9, pp. 93165-93181, 2021, doi: 10.1109/ACCESS.2021.3092827.

C. Yanarates, Y. Wang and Z. Zhou, "Unity Proportional Gain Resonant and Gain Scheduled Proportional (PR-P) Controller-Based Variable Perturbation Size Real-Time Adaptive Perturb and Observe (P&O) MPPT Algorithm for PV Systems," in IEEE Access, vol. 9, pp. 138468-138482, 2021, doi: 10.1109/ACCESS.2021.3119042.

Yanarates, C, Zhou, Z. "Fast-converging robust PR-P controller designed by using symmetrical pole placement method for current control of interleaved buck converter based PV emulator, " in Energy Sci Eng. 2021; 00: 1– 22. Doi:10.1002/ese3.1018.

C. Yanarates and Z. Zhou, "Design and Cascade PI Controller-Based Robust Model Reference Adaptive Control of DC-DC Boost Converter," in *IEEE Access*, vol. 10, pp. 44909-44922, 2022, doi: 10.1109/ACCESS.2022.3169591.

Y. Wang, C. Yanarates, and Z. Zhou, "External Current Source–Based Unilluminated PV Partial Shading Emulation System Verified Through the Hybrid Global Search Adaptive Perturb and Observe MPPT Algorithm," *Front. Energy Res.*, vol. 10, no. April, pp. 1–14, 2022, doi: 10.3389/fenrg.2022.868951.

C. Yanarates and Z. Zhou "Design and Cascade PI Controller-Based Robust Model Reference Adaptive Control of DC-DC Boost Converter," Centre for Power Electronics Annual Conference – July 2022.

Table of Contents

List of Figures

List of Tables

List of Acronyms

$A(.)$	State (system) matrix	d_{pwm}^1	Fundamental component of the PWM
ABC	Artificial bee colony	d_{pwm}^h	Harmonics of the PWM
ACO	Ant colony optimization	$dSPACE$	Digital Signal Processor for Applied and Control Engineering
ANN	Artificial neural network	ESC	Extremum seeking control
$B(.)$	Input matrix	F	Multiplicative factor
C	Capacitance	FF	Firefly
$C(.)$	Output matrix	FL	Fuzzy logic
CCM	Continuous conduction mode	$FNLMS$	Fractional normalized least mean square
CS	Cuckoo search	FOH	First-order hold
C_{dc}	DC link capacitance	f_{sw}	Switching frequency
$C(s)$	Controller transfer function	GA	Genetic algorithm
D	Duty ratio- Steady state duty cycle	$G(s)$	Unrealizable transfer function-Plant transfer function
DBC	DC-to-DC Boost converter	$G_{boost}(s)$	Boost converter transfer function
DC	Direct current	GCI	Grid connected inverter
DE	Differential evaluation	$G_{CL}(s)$	Closed-loop transfer function of the buck converter
D_{MAX}	Approximate maximum duty ratio	G_f	Filter transfer function
D_{max}	Maximum duty cycle	$G_H(s)$	Selective harmonics compensator transfer function
D_{min}	Minimum duty cycle	$G_{inner,PI}(s)$	Inner loop PI controller transfer function
$DNLMS$	Decorrelation normalized least mean square	G_{inv}	Inverter transfer function
D_{nom}	Nominal duty cycle	$G_{inv}(s)$	Inverter transfer function
d_{pwm}	PWM signal	$G_{notch}(s)$	Notch filter transfer function
$G_{outer,PI}(s)$	Outer loop PI controller transfer function	K_{PR}	PR controller proportional gain

G_{PR}	PR controller		L	Inductance
$G_{PR}(s)$	Transfer function of PR path		$LHPZ$	Left half plane zero
$G_{PRP}(s)$	Transfer function of the PR-P controller		L_{inv}	Filtering inductor
$G_{PVE}(s)$	Buck converter-based PV emulator transfer function		LMS	Least mean square
G_{PWM}	PWM transfer function		LQR	Linear quadratic regulator
GW	Grey Wolf		LTI	Linear-time-invariant
HC	Hill climbing		M_{cs}	Complementary sensitivity peak
HIL	Hardware-in-the-loop		ML	Machine learning
$H_R(s)$	Resonant path		MP	Minimum phase
i_C	Capacitor current		MPP	Maximum power point
IC	Incremental condcutance		$MPPT$	Maximum power point tracking
I_{cs}	External excitation current		$MRAC$	Model reference adaptive control
i_g^1	Fundamental grid current		M_s	Nominal sensitivity peak
I_g^1	Amplitude of fundamental grid current		NMP	Non-minimum phase
i_g^h	Grid current harmonics		P	Proportional gain
i_L	Inductor current		P_{dc}	DC side instantaneous power
i_{pv}	PV current		PI	Proportional-integral
IRP	Instantaneous reactive power		P_{inv}	Inverter output power
$I\text{-}V$	Current voltage characteristics		$P\&O$	Perturb and observe
k	Notch filter width adjustment parameter		PR	Resonant path of the PR-P
K_I	Integral gain		$PR\text{-}P$	Proportional resonant-proportional controller
K_P	Proportional gain		PSO	Particle swarm optimization
K_{P2}	Additional proportional gain		PV	Photovoltaic
$K_{P(ex)}$	Scheduled proportional gain		$P\text{-}V$	Power voltage characteristics
PVE	Photovoltaic emulator		V_D	Diode forward voltage
PWM	Pulse width modulation		V_{dc}	DC voltage

R_1	Resistance of MOSFET	V_g^1	Amplitude of fundamental grid voltage
R_2	Resistance of synchronous MOSFET	v_g^1	Fundamental grid voltage
RC	Resistor capacitor	Vin	Input voltage
$RHPZ$	Right half plane zero	$V_{in(\text{max})}$	Maximum input voltage
R_L	Inductor resistance	$V_{in(\text{nom})}$	Nominal input voltage
R_{Load}	Load resistance	V_{inv}^1	Amplitude of fundamental inverter output voltage
R_s	Series resistor	v_{inv}^1	Inverter output voltage
R_{sh}	Shunt resistor of photovoltaic cell	v_{inv}^h	Inverter voltage harmonics
RTA	Real time adaptive	$VMPP$	Maximum power point voltage
RTI	Real time interface	$Vout$	Output voltage
S	Contrallable switch	V_{pv}	DC component of the PV voltage
$S_\alpha^T(s)$	Sensitivity of $T(s)$ due to α	v_{pv}	PV voltage
$S_\beta^T(s)$	Sensitivity of $T(s)$ due to β	$\tilde{v}_{pv}$	AC component of the PV voltage
$SMPS$	Switch mode power supply	$V_{ref(out)}$	Reference model out voltage
SRF	Synchronous reference frame	X	State variable vector
SW	Switch	$x(t)$	State vector
THD	Total harmonics distortions	$y(t)$	Output vector
t_{off}	Off time	ZOH	Zero-order hold
t_{on}	On time	ξ	Damping ratio
T_s	Switching Period-Sample time	Φ	Adaptation parameter
		Υ	Learning rate
$T(s)$	Closed-loop transfer function of PR-P controller inverter system	φ_1	Inverter voltage leading angle
		ω_0	Fundamental angular frequency
$u(t)$	Input vector	φ	Power angle
		ω_c	Bandwidth
V_C	Capacitor voltage	ω_r	Resonant frequency
		ω_n	Natural frequency

Chapter 1

Introduction

1.1 Background

Over the last two decades, energy generation has shown a great tendency to utilize the renewable sources due to the facts that depletion of the fossil fuels, increasing concern of the environmental issues, energy security, productivity growth and reduction of the overall cost of power generation-distribution systems as a result of technological developments [1], [2]. Photovoltaic (PV) energy is a clean, renewable source of direct current (DC) energy generated from the sunlight, which attracts considerable attention due to remarkable advantages such as reliability and long-life, advanced manufacturing process, static and noise-free operations, increasing efficiency, decreasing prices, flexibility of construction and availability of government support and incentives [3], [4]. The increasing demand of PV energy systems has leaded to comprehensive studies in this field, common ground of these studies aims at achieving the increase in the efficiency, reliability and useful life-span of the PV systems and on the contrary the reduction in cost and space from generation to delivering of the energy [5], [6].

Due to inconsistent power generation from sustainable energy sources, which is dependent on the environment, they are difficult to be utilised without switching power supply, including the power conditioner. According to the statistics in [7],[8],[9] most of the electricity generated in developed countries, i.e., over 90% of generated power, is handled by power electronic circuits before being transmitted to the utility [10],[11],[12]. As a result, switching power supply energy efficiency (environmental protection), footprints (smart packaging technologies), power density (to reduce weight/volume) and reliability to achieve zero defect design for components and systems is critical in the renewable energy system applications [13],[14],[15].

Switched-mode power supplies (also known as a switched-mode power supply, switched power supply, SMPS, or switcher) are electronic power supplies that include switching regulators to efficiently convert electrical power. While converting voltage and current characteristics, an SMPS, like other power supplies, transforms power from a DC or AC source to DC loads. Because the switching transistor dissipates less power when serving as a switch, SMPS has a high efficiency up to 96 percent [16],[17]. Other benefits include reduced size, noise, and weight due to the absence of heavy line-frequency transformers, as well as reduced heat generation [18],[19]. The circuit topology of the SMPS can be used to classify them. The most significant distinctions to consider are isolated and non-isolated converters [20],[21],[22].

Single-phase PV inverter systems have been widely applied in photovoltaic power generation. Inverter current control with the object of injecting smooth current with less harmonics to the grid is the key aspect of the PV power sourced grid connected inverter (GCI) systems [7]. The main reasons of harmonic generation in single phase PV inverter systems are basically due to distortion in the grid voltage, switching harmonics (high frequency) and DC-link voltage variations arising from the MPPT [8], [9].

Employing MPPT algorithms is essential in terms of improving energy harvesting efficiency in PV systems since electrical characteristics of PV modules are weather dependent and manifested in the output current and voltage waveforms under variations of irradiance and ambient temperature [10]. A series of recent studies indicated that soft computing intelligent systems such as particle swarm optimization (PSO) [11], fuzzy logic (FL) [12], [13], genetic algorithms (GA) [14], artificial neural networks (ANN) [15], machine learning (ML) [16], differential evolution (DE) [17], ant colony optimization (ACO) [18], artificial bee colony (ABC) [19], grey wolf (GW), firefly (FF) [20] and cuckoo search (CS) [21] have come into widespread use in the development of MPPT techniques for the PV systems as a result of increasing use of hardware-in-the-loop (HIL) and RTI applications. Soft computing intelligent systems, although having higher efficiency in the presence of abrupt and dynamic irradiance and temperature changes, have several evident disadvantages; for instance, complexity, computational burden, implementation cost, slow tracking speed, lacking flexibility, sensitivity of initialization for multi-level optimization [22],[10]. Consequently, many existing studies in the literature have re-visited the conventional

MPPT methods such as P&O, hill climbing (HC) and incremental conductance (IC) for further examination to improve [23].

P&O MPPT technique is one of the most common and the simplest algorithms that stands out amongst others with its fast convergence to maximum power point (MPP) [24], [25]. However, continuous oscillations around the MPP with respect to the imposed perturbation and production of average MPP value lower than it could be due to large step size are considered as shortcomings of this method [26]. Depending on the perturbation size, the oscillation results in certain amount of power loss and improper choice of the step size leads to poor tracking performance [27].

Testing the performance of the MPPT algorithms and the power electronic converters with real installed solar panels is a considerable challenge because of the constraints such as need for wide surrounding space, high installation cost and the lack of control over the environmental conditions [28],[29]. Under such constraints, the use of PVEs is the most cost-effective solution to test MPPT algorithms and power electronics converters [30],[31]. The use of cost-effective emulators provides a clear incentive for global enterprise and scientific development [32]. For the ideal PVE, there are specific requirements which include a proper emulation of non-linear I-V and P-V characteristics of a PV panel, which function under varying atmospheric conditions (temperature and irradiance) [33]. The emulator must be able to integrate Power Electronics Converter interfaces for testing [29]. It must also be able to function appropriately under frequent load changes [34]. Contemporary scientific enquiry has found that emulated I-V and P-V curves produce similar results to real PV panel outcomes (in terms of the datasheet) [35]. However, advantages and disadvantages have been identified in terms of performance criteria, such as implementation costs; efficiency; accuracy; the level of complexity; sensitivity to variable environmental conditions and frequent load changes [28],[36],[37].

In this thesis, Cascade PI Controller-Based Robust Model Reference Adaptive Control (MRAC) of a DC-DC boost converter, Proportional Gain Resonant and Gain Scheduled Proportional (PR-P) Controller based variable perturbation size real-time adaptive perturb and observe (P&O) maximum power point tracking (MPPT) algorithm, the interleaved buck converter based photovoltaic (PV) emulator current control and a symmetrical pole placement Method-based Unity Proportional Gain

Resonant and Gain Scheduled Proportional (PR-P) Controller for single phase PV inverter systems have been reviewed and discussed.

Cascade PI Controller-Based Robust Model Reference Adaptive Control (MRAC) scheme efficiently resolved complications and challenges by using features of cascade PI control loop in combination with properties of MRAC. The accuracy of the proposed control system's ability to track the desired signals and regulate the plant process variables in the most beneficial and optimised way without delay and overshoot is verified using MATLAB/Simulink by applying comparative analysis with single PI and cascade PI controllers.

Proportional Gain Resonant and Gain Scheduled Proportional (PR-P) Controller based variable perturbation size real-time adaptive perturb and observe (P&O) maximum power point tracking (MPPT) algorithm resolved the drawbacks of conventional P&O MPPT method associated with the use of constant perturbation size that leads to poor transient response and high continuous steady-state oscillations. The prime objective of using the PR-P controller is to utilize inherited properties of the signal produced by the controller's resonant path and integrate It to update best estimated perturbation that represents the working principle of extremum seeking control (ESC) to use in P&O algorithm that characterizes the overall system learning-based real time adaptive (RTA). Additionally, utilization of internal dynamics of the PR-P controller overcome the challenges namely, complexity, computational burden, implantation cost and slow tracking performance in association with commonly used soft computing intelligent systems and adaptive control strategies.

A proportional-resonant-proportional (PR-P) controller is designed to resolve the drawbacks of conventional PI controllers in terms of phase management which means balancing currents evenly between active phases to avoid thermally stressing and provide optimal ripple cancellation in the presence of parameter uncertainties for the interleaved buck converter based photovoltaic (PV) emulator current control.

The symmetrical pole placement Method-based Unity Proportional Gain Resonant and Gain Scheduled Proportional (PR-P) Controller resolved the issues that are tracking repeating control input signal with zero steady-state and mitigating of ^{3r}d order harmonic component injected into the grid associated with the use of PI controller for single-phase PV systems. Additionally, the PR-P controller has overcome the

4

drawbacks of frequency detuning in the grid and increase in the magnitude of odd number harmonics in the system that constitute the common concerns in the implementation of conventional PR controller developed as an alternative to PI controller.

1.2 Aims and Objectives

This thesis builds upon design and implementation of sophisticated control techniques of power electronic interfaces which are the most essential components of photovoltaic power systems. The proposed contribution has been aimed to investigate and resolve the problems associated with DC boost converter, interleaved buck converter, maximum power point tracking, single phase inverter current control and harmonic compensation for photovoltaic power generation systems. The scope of this research entails the following:

- Investigate and analyse non-minimum phase behaviour of the DC-to-DC boost converter due to right half plane zero which constitutes a challenge and its non-linear dynamics which complicate the control process while operating in continuous conduction mode (CCM). In this regard, designing a controller to resolve the complications and challenges.

- To investigate and study the Perturb and Observe (P&O) maximum power point tracking (MPPT) technique along with its merits and limitations, employed in operating a PV panel at maximum power point and to design a control algorithm to resolve the drawbacks of conventional P&O MPPT method associated with the use of constant perturbation size that leads to poor transient response and high continuous steady-state oscillations.

- To investigate and study the tracking problem of repeating control input signal with zero steady-state and mitigating of 3rd order harmonic component (the cause of the greatest level of distortion amongst harmonic components) injected into the grid associated with the use of PI controller for single-phase PV systems. Accordingly, to design a controller to overcome these issues.

- To investigate and study the interleaved buck converter based photovoltaic (PV) emulator (the most common switch-mode power supply-based emulator) current control drawbacks (e.g., phase management which means balancing currents evenly between active phases to avoid thermally stressing and provide optimal ripple cancellation in the presence of parameter uncertainties) associated with the use of conventional PI controllers. To design a novel controller by taking these issues into consideration.

- To derive the transfer functions of all switch mode power supplies by using state-space average method for time and frequency domain analysis.

- To validate the performance of the proposed control schemes experimentally with the implementation of MATLAB/Simulink/Stateflow on dSPACE Real-time-interface (RTI) 1007 processor board, DS2004 A/D and CP4002 Digital I/O boards.

1.3 Contributions

- Non-minimum phase behaviour of the boost converter due to right half plane zero constitutes a challenge and its non-linear dynamics complicate the control process while operating in continuous conduction mode (CCM). Cascade PI Controller-Based Robust Model Reference Adaptive Control (MRAC) scheme efficiently resolved complications and challenges by using features of cascade PI control loop in combination with properties of MRAC. The accuracy of the proposed control system's ability to track the desired signals and regulate the plant process variables in the most beneficial and optimised way without delay and overshoot is verified. The experimental results and analysis reveal that the proposed control strategy enhanced the tracking speed two times with considerably improved disturbance rejection.

- Proportional Gain Resonant and Gain Scheduled Proportional (PR-P) Controller based variable perturbation size real-time adaptive perturb and observe (P&O) maximum power point tracking (MPPT) algorithm resolved the

6

drawbacks of conventional P&O MPPT method associated with the use of constant perturbation size that leads to poor transient response and high continuous steady-state oscillations. The prime objective of using the PR-P controller is to utilize inherited properties of the signal produced by the controller's resonant path and integrate it to update best estimated perturbation that represents the working principle of extremum seeking control (ESC) to use in P&O algorithm that characterizes the overall system learning-based real time adaptive (RTA). Additionally, utilization of internal dynamics of the PR-P controller overcome the challenges namely, complexity, computational burden, implantation cost and slow tracking performance in association with commonly used soft computing intelligent systems and adaptive control strategies. The experimental results and analysis reveal that the proposed control strategy enhanced the tracking speed five times with reduced steady-state oscillations around maximum power point (MPP) and more than 99% energy extracting efficiency.

- The proportional-resonant-proportional (PR-P) controller resolved the drawbacks of conventional PI controllers in terms of phase management which means balancing currents evenly between active phases to avoid thermally stressing and provide optimal ripple cancellation in the presence of parameter uncertainties. The proposed controller shows superior performance in terms of 10 times faster-converging transient response, zero steady-state error with significant reduction in current ripple. Equal load sharing that constitutes the primary concern in multi-phase converters has been achieved with the proposed controller. Implementing of robust control theory involving comprehensive time and frequency domain analysis reveals 13% improvement in the robust stability margin and 12-degree bigger phase toleration with the PR-P controller.

- The symmetrical pole placement Method-based Unity Proportional Gain Resonant and Gain Scheduled Proportional (PR-P) Controller resolved the issues that are tracking repeating control input signal with zero steady-state and mitigating of 3rd order harmonic component injected into the grid associated

with the use of PI controller for single-phase PV systems. Additionally, the PR-P controller has overcome the drawbacks of frequency detuning in the grid and increase in the magnitude of odd number harmonics in the system that constitute the common concerns in the implementation of conventional PR controller developed as an alternative to PI controller. Moreover, the application of an unprecedented design process based on changing notch filter dynamics with symmetrical pole placement around resonant frequency overcomes the limitations that are essentially complexity and dependency on the precisely modelled system associated with the use of various controllers such as Adaptive, Predictive and Hysteresis in grid connected PV power generation systems.

- Sensitivity analysis has been implemented to the system to observe the impact of variations in inverter input voltage and filtering inductance. Thus, controller parameters are selected in a way that the closed-loop system ensures that design requirements are met, even fluctuations in process dynamics occur when the system is in operation. It has been observed that the overall system is more sensitive to the variations in the inverter filtering inductance compared to the inverter input voltage. However, both cases have met the requirement which is having small nominal sensitivity peak for low frequencies. This provides better reference tracking and disturbance rejection.

1.4 Research Outline

This thesis is organised as follows.:

Chapter 1: introduces renewable energy, with a focus on the generation of solar power. The chapter also introduces the many tasks that will be examined and implemented as part of this study.

Chapter 2: introduces the notch filter dynamics-based PR-P controller designed by complementary symmetrical pole placement method. The chapter also introduces the state-space average technique as well as small signal analysis which is used to derive transfer functions of switch mode power supplies.

Chapter 3: presents design and implementation of cascade PI controller-based model reference adaptive control of the DC-to-DC boost converter. This chapter introduces the problems associated with the control of the boost converter and commonly used control method with their advantages, disadvantages, and limitations.

Chapter 4: presents design and implementation of unity proportional gain resonant and gain scheduled proportional (PR-P) controller-based variable perturbation size real-time adaptive perturb and observe (P&O) MPPT algorithm for PV systems.

Chapter 5: presents fast converging robust PR-P controller designed by using complementary symmetrical pole placement method for current control of interleaved buck converter-based PV emulator.

Chapter 6: presents symmetrical pole placement method-based unity proportional gain resonant and gain scheduled proportional (PR-P) controller with harmonic compensator for single phase grid-connected PV inverters.

Chapter 7: the conclusion of the thesis is summarised in this chapter, and future work is proposed based on current work and research demand.

Chapter 2

The Proposed PR-P Controller Design Process and Mathematical Modelling of Switch Mode Power Converters

2.1 The Notch Filter Dynamics-based PR-P Controller Designed by Symmetrical Pole Placement Method

The PR controller has become widely used current regulator for grid-connected single-phase inverter systems [1], [2], [3]. The most important feature of the PR controller is its capability of tracking repeating signals with zero steady-state error by producing high gain at specified frequency. The PR controller offers several advantages, such as resolving the computational burden and complexity due to removal of Park transformations, providing great convenience and simplicity to implement [4].

The PR controller itself is not a method used in DC-to-DC converters but its property that enables control of gain at a specified frequency range is instrumental in developing of the proposed control methods in this thesis. Transfer function of the ideal PR controller in continuous time (the s domain) is represented by:

$$G_{PR}(s) = K_P + K_I \frac{s}{s^2 + \omega_r{}^2} \tag{2.1}$$

where K_P, K_I and ω_r are defined as proportional gain, integral gain, and resonant frequency, respectively. The problem associated with the use of the ideal PR controller transfer function is that it attains infinite gain at ω_r. The introduced infinite gain leads to an infinity quality factor which cannot be achieved in either analog or digital applications [5]. Stability problems associated with the infinite gain at the resonant frequency are prevented with a non-ideal PR controller which is generated by introducing damping to the ideal transfer function [6], [7]. The non-ideal PR controller

transfer function with addition of the bandwidth (ω_c) around the ac resonant frequency (ω_r) is represented by:

$$G_{PR}(s) = K_P + K_I \frac{2\omega_c s}{s^2 + 2\omega_c s + \omega_r^2} \tag{2.2}$$

The generic frequency response of a notch filter and a PR controller is given in Figure 2.1. Attaining phase shift at the resonant frequency is one of the key points of the PR-P controller-based variable perturbation size real-time adaptive P&O MPPT algorithm. In extremum seeking control (ESC), this phase shift is a tuning parameter to line up better with the perturbation signal. In the proposed method, the inherited dynamics of the resonant path is used for this purpose that simplifies control strategy.
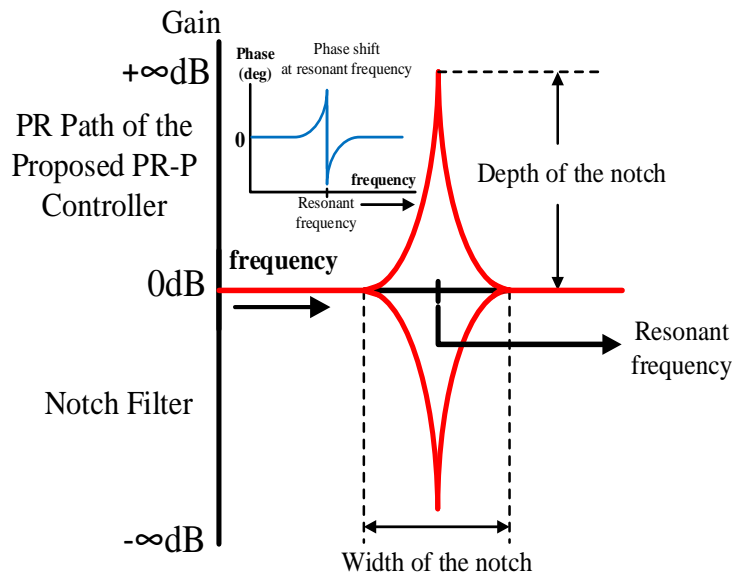
Figure 2.1: Generic frequency response of a notch filter and PR path of the PR-P controller.

The design process of the PR controller in the study is based on notch filter dynamics and subsequently taking reciprocal of the generated notch filter transfer function at intended frequency [8]. Designing method of the notch filter involving parameters with their functions is given in Figure 2.2.
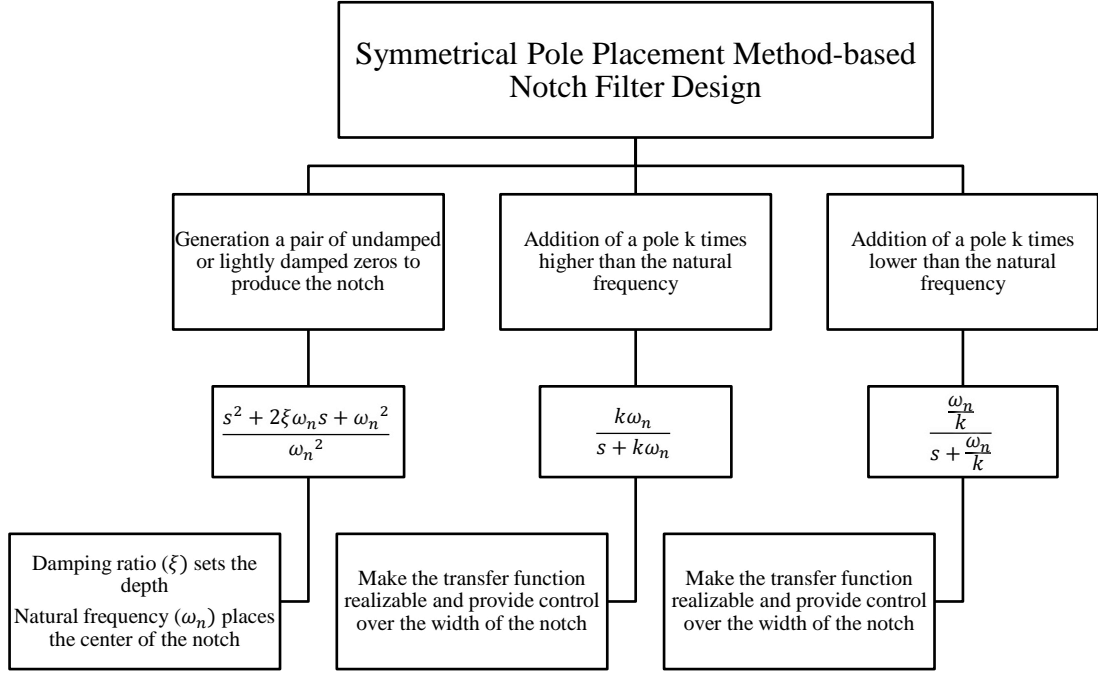
Figure 2.2: Complementary (symmetrical) pole placement method-based notch filter design process.

The effects of variations in the damping ratio (ξ) and the parameter k on frequency response of the notch characterized by magnitude and phase responses is given in Figure 2.3. The parameter k is set to adjust the width of the notch, the damping ratio (ξ) is set to adjust the depth of the notch and the natural frequency (ω_n) is set to adjust the location of the notch that refers to resonant frequency for the PR path of the proposed PR-P controller.

(a) Frequency response with varying ξ (b) Frequency response with varying k
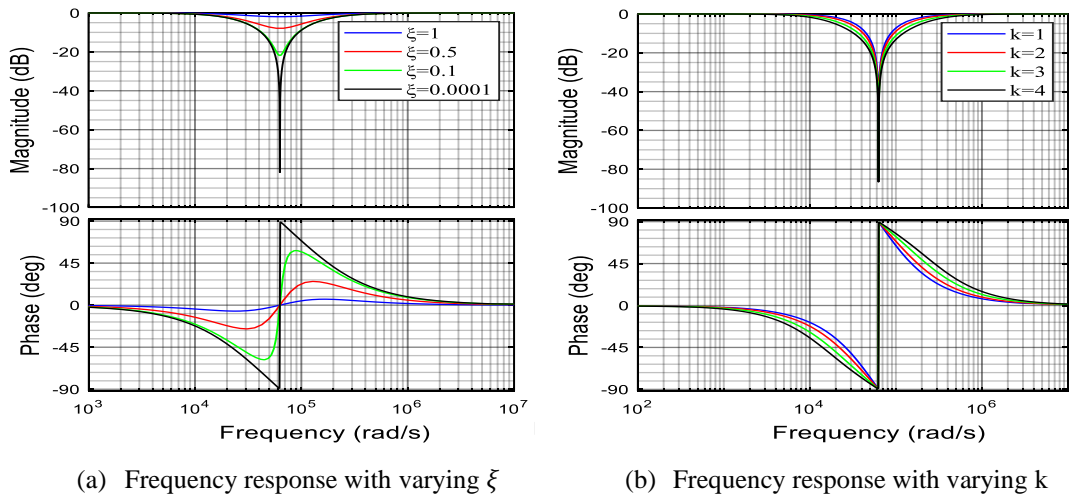
Figure 2.3: Phase and magnitude responses of the notch filter.

The variable k will be defined as the ratio of each pole located on both sides of the natural frequency that determines cut-off frequencies of the complementary poles. The parameter k can be adjusted according to the requirement. The larger value of k corresponds with a wider notch, and vice versa. An unrealizable transfer function $G(s)$ generated by locating a pair of zeros with lightly damping ratios (0.5 for the boost converter and 0.001 for the buck converter in this study) at the PWM switching frequencies of switch mode power supply ($20\ kHz$ for boost converter and $10\ kHz$ for buck converter in this study) corresponding to the resonant frequency of the PR path and setting the parameter k value to 2 for the application is given by:

$$G(s) = \frac{s^2 + 2\xi\omega_n s + \omega_n{}^2}{\omega_n{}^2} \qquad (2.3)$$

First pole s_1 with a cut-off frequency k time larger than the natural frequency is given by:

$$s_1 = \frac{k\omega_n}{s + k\omega_n} \qquad (2.4)$$

Second pole s_2 with a cut-off frequency k time smaller than the natural frequency is given by:

$$s_2 = \frac{\dfrac{\omega_n}{k}}{s + \dfrac{\omega_n}{k}} \qquad (2.5)$$

Addition of both poles s_1 and s_2 to the transfer function $G(s)$ results in a formation of a second-order band-stop filter whose transfer function $G_{notch}(s)$ is given by:

$$G_{notch}(s) = G(s).s_1.s_2$$

$$= \frac{s^2 + 2\xi\omega_n s + \omega_n{}^2}{\omega_n{}^2} \cdot \frac{k\omega_n}{s + k\omega_n} \cdot \frac{\dfrac{\omega_n}{k}}{s + \dfrac{\omega_n}{k}} \qquad (2.6)$$

2.2 State-Space Average and Small Signal Modelling of the Switch Mode Power Supplies

Analysis of a plant requires developing a mathematical input-output model that best approximates a system's physical reality. A method of constructing a mathematical description of a system is referred to as system modelling. A properly modelled system enables to predict plant response and to observe its behaviours in both time and

frequency domains. Transfer function of a plant defines the relation between the output and the input of the system and provides a lot of information about the dynamics of the plant. Furthermore, precisely derived transfer function of a system has great importance for an effective controller design. Control systems are designed and implemented to improve important dynamic properties of the plant such as stability, speed of response, steady-state error, oscillations which constitute the transient and the steady-state responses of the system [9].

Transfer function model of the intended buck converter is derived by using dynamic (AC small signal) state-space technique [10],[11]. This process includes taking the Laplace Transform (with zero initial condition) of both the state and output equations in the state-space model of the buck converter [12]. The most general state-space representation of a system with p inputs, q outputs and n state variables is given in Figure 2.4.

Input
$u(t)$

$$\dot{x} = Ax + Bu$$
$$y = Cx + Qu$$

System described by state variables $\{x_1, x_2 \ldots\}$

Output
$y(t)$

$x(t)$ State Variables
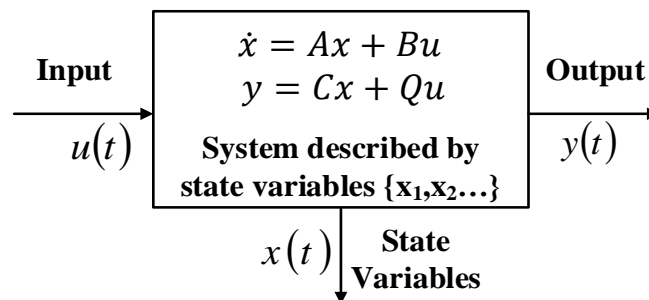
Figure 2.4: The generic representation of the state-space equations.

where $x(.)$, $y(.)$, $u(.)$, $A(.)$, $B(.)$, $C(.)$ and $Q(.)$ are state vector with $x(t) \in \mathbb{R}^n$, output vector with $y(t) \in \mathbb{R}^q$, input (control) vector with $u(t) \in \mathbb{R}^p$, state (system) matrix with $dim[A(.)] = n \times n$, input matrix with $dim[B(.)] = n \times p$, output matrix with $dim[C(.)] = q \times n$ and feedthrough (feedforward) matrix with $dim[Q(.)] = q \times p$, respectively. The flowchart of the state-space averaging technique is given in Figure 2.5.

1 — Description of Notations	2 — ON and OFF States	3 — Basic Averaged Model

Box 1:
$d \equiv duty\ ratio$
$d' \equiv 1 - d$
$T_s \equiv switching\ period$

Box 2:
Interval dT_s
$\dot{x} = A_1 x + B_1 v_{in}$
Interval $d'T_s$
$\dot{x} = A_2 x + B_2 v_{in}$

Box 3:
$\dot{x} = Ax + Bv_{in}$
$A = dA_1 + d'A_2$
$B = dB_1 + d'B_2$

Box 4 — Perturbation:
$d = D + \hat{d}$
$x = X + \hat{x}$
$y = Y + \hat{y}$
$v_{in} = V_{in} + \hat{v}_{in}$

Box 5 — Steady-state DC Model:
$AX + BV_{in} = 0$
$X = -A^{-1}BV_{in}$

Box 6 — Dynamic (AC small signal) Model:
$\hat{\dot{x}} = A\hat{x} + B\hat{v}_{in} + [(A_1 - A_2)X + (B_1 - B_2)V_{in}]\hat{d}$
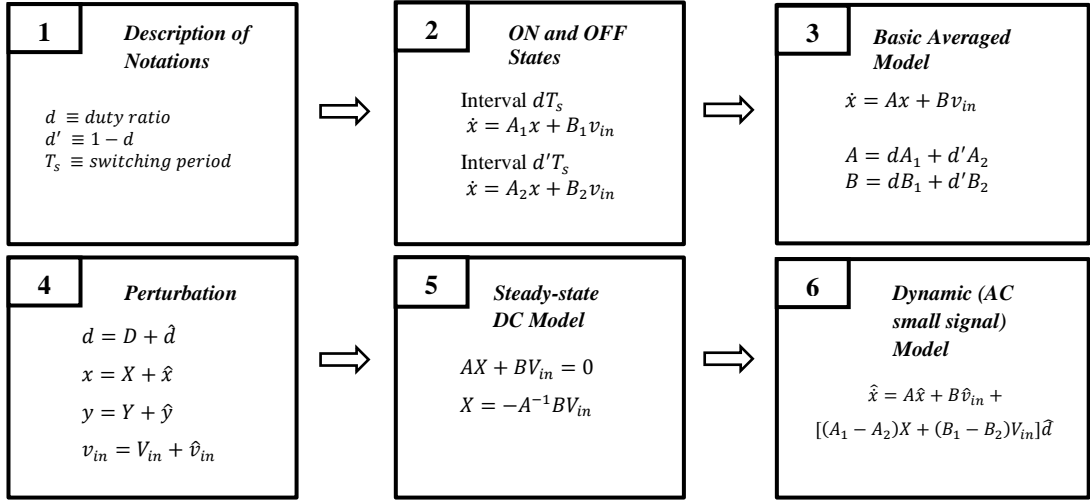
Figure 2.5: Flowchart of the state-space averaging of switch mode power supplies.

State-Space Average Method is one of the developed techniques to obtain the transfer function of the plant, analyse properties and behaviours of the switch mode power supplies (SMPS) [12],[13]. Providing a substantial insight and its simplicity for both derivation and implementation has made the method a very useful and convenient tool in the applications of power electronics devices [12],[14]. The outline of the modelling is summarized in Figure 2.5. There are two states determined according to ON-and-OFF the transistor in the circuit, so SMPS circuit analysis consists of two topologies. Description of operating range (intervals) for each state has been made by commonly used conversions and notations are given by:

$$d \equiv duty\ ratio$$
$$d' \equiv 1 - d \tag{2.7}$$
$$T_s \equiv switching\ period$$

A linear-time-invariant (LTI) system model in the state-space form can be represented as given by [10]:

$$\dot{x} = Ax + Bu$$
$$y = Cx + Du \tag{2.8}$$

Each state of the SMPS can be described as a set of linear-time-invariant differential equations. The state and output equations with input voltage v_{in} for the ON state during the interval of dT_s is given by:

$$\dot{x} = A_1 x + B_1 v_{in}$$
$$y_1 = C_1 x \tag{2.9}$$

15

The state and output equations for the OFF state during the interval of $d'T_s$ is given by:

$$\dot{x} = A_2 x + B_2 v_{in}$$
$$y_2 = C_2 x$$

(2.10)

The elements of the state vector x are inductor currents and capacitor voltages as inductor and capacitor are the only energy storage components of the SMPS. To obtain a single continuous state-space equation (single matrix differential equation) (2.9) and (2.10) must be combined in a sense of averaging the system, input and output matrices to result in A, B and C matrices. The averaging process purely depends on the duty ratio (d), and it is executed as:

$$A = dA_1 + d'A_2$$
$$B = dB_1 + d'B_2$$
$$C = dC_1 + d'C_2$$

(2.11)

The vector block diagram for a linear-time-invariant system in terms of state-space dynamics is given in Figure 2.6 and the average state-space equation of the system is given by:
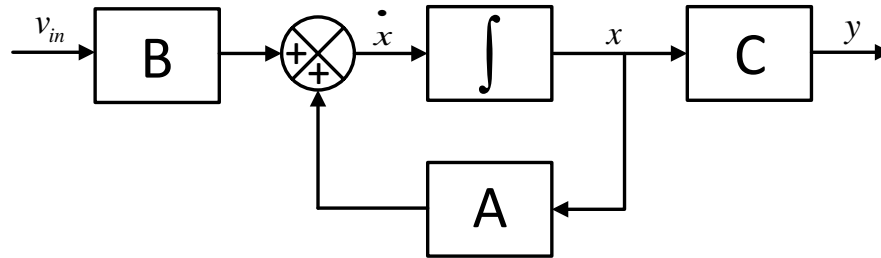
Figure 2.6: Linear system state-space vector diagram.

$$\dot{x} = Ax + Bv_{in}$$
$$y = Cx$$

(2.12)

Equation (2.12) describes the averaged behaviour of the SMPS, and it basically removes ripples of the inductor current and capacitor voltage that are the inherent property of the state variables. One of the significant points to note here is that the system matrix A and the input matrix B may be duty ratio dependent, which leads to the conclusion that the averaged equation may be non-linear regarding the duty ratio (d). The purpose of using state-space model of the SMPS is to generate an equivalent circuit model and carrying out the analysis of the system around a linearization point

by perturbing the averaged equation about this operation point. Small signal variation with the steady state values is represented as:

$$d = D + \hat{d}$$
$$x = X + \hat{x}$$
$$y = Y + \hat{y} \qquad (2.13)$$
$$v_{in} = V_{in} + \hat{v}_{in}$$

The capitalized quantities in (2.13) represent the steady state values and the carets are small perturbations. The perturbation is performed by making substitution (2.13) into (2.12) and the expanding of the new state-space equation is obtained in (2.14) as the following:

$$\dot{X} + \dot{x} = \left[(D + \hat{d})A_1 + (1 - D - \hat{d})A_2\right](X + \hat{x}) +$$
$$\left[(D + \hat{d})B_1 + (1 - D - \hat{d})B_2\right](V_{in} + \hat{v}_{in}) \qquad (2.14)$$
$$Y + \hat{y} = \left[(D + \hat{d})C_1 + (1 - D - \hat{d})C_2\right](X + \hat{x})$$

The equation of steady state operating point when the small signal perturbations are zero is given by:

$$0 = AX + BV_{in}$$
$$Y = CX \qquad (2.15)$$

Discarding of the second order small signal variation terms in (2.14) results in AC small signal (dynamic) model of the system given by as the following:

$$\hat{x} = A\hat{x} + B\hat{v}_{in} + \left[(A_1 - A_2)X + (B_1 - B_2)V_{in}\right]\hat{d}$$
$$\hat{y} = C\hat{x} + (C_1 - C_2)X\hat{d} \qquad (2.16)$$

The expansion of the A, B and C matrices in (2.16) are given by:

$$A = DA_1 + D'A_2$$
$$B = DB_1 + D'B_2$$
$$C = DC_1 + D'C_2 \qquad (2.17)$$

Setting $\hat{v}_{in} = 0$ produces the response to the variation of the duty factor and (2.16) transforms into the following equation.

$$\hat{x} = A\hat{x} + \left[(A_1 - A_2)X + (B_1 - B_2)V_{in}\right]\hat{d}$$
$$\hat{y} = C\hat{x} + (C_1 - C_2)X\hat{d} \qquad (2.18)$$

The simplified representation of the state equation in (2.18) is given by:

$$\hat{\dot{x}} = A\hat{x} + F\hat{d} \qquad (2.19)$$

Variation of state variables to the duty factor can be easily solved by application of the Laplace Transform as the following:

$$\frac{\hat{\dot{x}}}{\hat{d}} = [sI - A]^{-1}F \qquad (2.20)$$

In (2.20), notation I stands for the unit matrix that is the same size of the system matrix A and $[sI - A]^{-1}$ is the inverse of the matrix $[sI - A]$.

Thus far, the state-space modelling of the DC-to-DC switch mode power converters is represented in terms of small-signal and low-frequency behaviour by deriving an equivalent linear circuit description comprising of averaging, perturbation, and linearization process.

2.3 Summary

In this Chapter, the Notch Filter Dynamics-based PR-P Controller designed by symmetrical pole placement method and state-space average and small signal modelling of the switch mode power supplies which have been utilized for various purposes and in different applications have been presented inclusively. The resonant path of the PR-P controller (PR) with a constant proportional unity gain has been designed considering the changing dynamics of a notch filter by pole placement method (adding mutually complementary poles to the notch transfer function) at PWM switching frequency. The proportional gain path (P) of the PR-P controller is used to determine the compatibility of the controller with parameter uncertainty of the system and designed by utilizing loop-shaping method.

State-space average and small signal modelling of the studied boost, buck converters and single-phase inverter has been used to derive the transfer functions of these switch mode power supplies. The primary purpose of deriving transfer functions of the systems was to benefit from the advantages of this mathematical modelling. A transfer function is a useful approach to express the input-output relationship of a linear, time-invariant system. It is derived by performing a Laplace transform on the differential

equations describing system dynamics with zero initial conditions. Transfer functions are also used for performing time-domain and frequency-domain analysis and controller design and are commonly employed in block diagram representations of systems. The main benefit of transfer functions is that they allow engineers to analyse and build systems using simple algebraic equations rather than sophisticated differential equations.

Chapter 3

Design and Cascade PI Controller-Based Robust Model Reference Adaptive Control of DC-DC Boost Converter

3.1 Introduction

The energy problem linking between energy access and greenhouse gas emissions has been given more attention recently, and consequently there has been a noticeable increase in the use of renewable energy sources for power generation around the world [1],[2],[3],[4],[5],[6].

Because of inconsistent power generation from sustainable energy sources, which is dependent on the environment, they are difficult to utilise without switching power supply, including the power conditioner. According to the statistics in [7],[8],[9] the vast majority of electricity generated in developed countries, i.e. over 90% of generated power, is handled by power electronic circuits before being transmitted to the utility [10],[11],[12]. As a result, switching power supply energy efficiency (environmental protection), footprints (smart packaging technologies), power density (to reduce weight/volume) and reliability to achieve zero defect design for components and systems is critical in the renewable energy system applications [13],[14],[15].

Switched-mode power supplies (also known as a switched-mode power supply, switched power supply, SMPS, or switcher) are electronic power supplies that include switching regulators to efficiently convert electrical power. While converting voltage and current characteristics, an SMPS, like other power supplies, transforms power from a DC or AC source to DC loads. Because the switching transistor dissipates less power when serving as a switch, SMPS has a high efficiency up to 96 percent [16],[17].

Other benefits include reduced size, noise, and weight due to the absence of heavy line-frequency transformers, as well as reduced heat generation [18],[19]. The circuit topology of the SMPS can be used to classify them. The most significant distinctions to consider are isolated and non-isolated converters [20],[21],[22].

The three fundamental forms of non-isolated converters all use a single inductor for energy storage given in Table 3.1. D is the duty cycle of the converter in the voltage relation column, and it can range from 0 to 1. The input voltage (Vin) is expected to be larger than zero; if it is negative, negate the output voltage for consistenc''s sake (Vout).

Table 3.1: The fundamental forms of non-isolated converters. D is the duty cycle of the converter in the voltage relation column, and it can range from 0 to 1.

Type	Typical Power (W)	Energy Storage	Voltage Relation	Features
Buck Converter	0-1,000	Single Inductor	$0 \leq V_{out} \leq V_{in}$ $V_{out} = DV_{in}$	Continuous current at output
Boost Converter	0-5,000	Single Inductor	$V_{out} \geq V_{in}$ $V_{out} = \dfrac{1}{1-D}V_{in}$	Continuous current at input
Buck-boost Converter	0-150	Single Inductor	$V_{out} \leq 0$ $V_{out} = -\dfrac{D}{1-D}V_{in}$	Discontinuous current at both input and output

The DC-DC boost converter (DBC) is the simplest converter topology for effectively reproducing increased output voltage for a given input voltage [23]. It has been used in a wide range of applications such as automotive industry (hybrid electric vehicles), power amplifications, adaptive control applications, battery power systems, consumer electronics, robotics, DC motor drives, communication applications (radar systems), wind power and photovoltaic (PV) systems (e.g., DC micro-grid) [24],[25],[26].

Because of exhibiting non-minimum phase (NMP) behaviour due to right half plane zero (RHPZ) and non-linear dynamics, controller design for DBCs is more complex and challenging than for buck converters [27],[28]. The comparative analysis of the most common developed control techniques for SMPS applications in terms of their features, advantages, and limitations is given in Table 3.2. The phenomenon commonly known as the NMP behaviour is the phase lag caused by transfer of accumulated energy of the inductor when the switch is on to the load during off time.

This attribute is reflected by the existence of a RHPZ in the control to output voltage transfer function [26]. By restricting the closed loop bandwidth feasible by feedback control, the NMP nature complicates the control effort. The dynamic change in positive zero location induced by varying converter settings such as load resistance and voltage gain exacerbates the NMP problem. Moreover, a reduction in input voltage or load resistance tends to destabilise the closed loop system by shifting the RHPZ towards origin.

The following two categories can be used to categorise the methods offered in the literature to address the NMP problem in a DBC: (i) converter topology modification approaches to achieve minimum phase (MP) dynamics. (ii) specially built controllers that correct for NMP dynamics. In this study, the second strategy is used by utilizing the properties of both cascade PI controller and reference model adaptive control in consideration of the inherent challenges, such as non-linearity, NMP nature, time discontinuities, and model uncertainty (unknown parasitic values, resistance and voltage drops across switching element and diode, uncertainty in the value of inductance, etc.).

Table 3.2: Comparative analysis of the most common control techniques used for SMPS applications.

Control Technique	Features	Advantages	Limitations	References
Proportional-Integral (PI)	•Suitable for linear control •Low-complexity	•Simple implementation •Fast transient response •Easy integration with various control techniques	•Incapable of responding to external distubance (e.g., load variations) •High settling time, steady-state error, overshoots	[32],[33],[34],[35],[36]
Sliding Mode Control (SMC)	•Robust and suitable for non-linear control •Converge towards sliding surface	•Simple Implementation •Capable of responding to external disturbance •Fast dynamics (e.g., settling time) •Robust	•Chattering issues due to discontinuous control law •Excessive overshoots	[33],[36],[37],[38],[39],[40]
Model Predictive Control (MPC)	•Easy for online iteration •Robust and suitable for non-linear control •Eanble to predict furure states	•Enhanced transient performance with external constraints •Fast response •Efficient tracking with estimation-based techniques	•Sensitive to circuit parameters •High computational burden •Required for detailed knowledge of the model	[32],[36],[41],[42],[43]
State-space Modeling (SSM)	•Robust and suitable for non-linear control •Suitable for multiple-input and multiple-output systems •Enable to estimate plant states continuously	•Improved transient response •Less overshoot during load varying conditions	•Longer period of time required for initial implementation •Required for detailed knowledge of the model	[36],[44],[45],[46],[47]
Fuzzy Logic Control (FLC)	•Robust and suitable for non-linear control •Providing stability in the presence of large variations •Suitable for the systems with imprecise boundary conditons	•Less overshoots •Efficient tracking response •Do not require the mathematical model of the plant	•High computational burden •Required for properly defined rules for operation •Longer settling time	[36],[48],[49],[50],[51]

3.2 Transfer Function Estimation of The Boost Converter

3.2.1 Computer Aided Transfer Function Estimation

Transfer function of the boost converter is derived by using Simulink® Control Design™. The transfer function estimation process is based on collecting frequency response data from the Simulink model of the proposed converter whose parameters are given in Table 3.3.

Table 3.3: Design parameters of the boost converter.

Parameter	Value
Input voltage(V_{dc})	20 V
Switching frequency (f_{sw})	20 kHz
Inductance (L)	100 µH
Output capacitance (C_{out})	440 µF
Constant voltage load (V_{out})	40 V
Resistance (R)	16 Ω

Transfer function of a boost converter can be modelled using the relationship of various interacting parameters of the device. In this chapter, transfer function from the PWM duty cycle set-point to the load voltage is the subject of the study to be interested and designing controllers depends on this association. Collecting frequency response data is executed by adding perturbation to the duty cycle set-point with sinusoids of different frequencies and storing the load voltage accordingly. Carried out frequency is in the range of 10 to 1/10th rad/s of the switching frequency. The main purpose of this implementation is to figure out how the system modifies the magnitude and phase of the injected sinusoidal signals. Alternatively stated, frequency input point is the duty cycle, and the output is the load voltage. The sinusoids injected at the input point is chosen as 0.03 which is the perturbation of the operating duty cycle (D) in the steady state which is calculated as:

$$\frac{V_{out}}{V_{dc}} = \frac{1}{1-D} \Longrightarrow D = 0.5 \tag{3.1}$$

The magnitude and phase plot from duty cycle to load voltage in terms of discrete points on the intended frequency range is given in Figure 3.1.
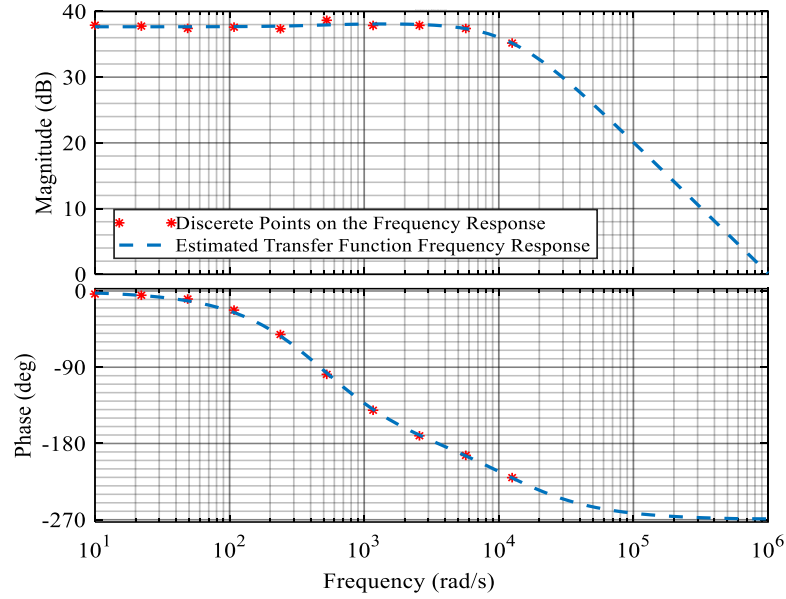
Figure 3.1: The magnitude and phase plot from duty cycle to load voltage on the intended frequency range.

The Bode plot of the proposed boost converter in Figure 1. shows that the magnitude is 38 dB. There is inconsiderable resonance around 2670 rad/s and a high frequency roll-off of around 20 dB/decade. According to these collected discrete frequency points, an estimated transfer function of the proposed boost converter in a continuous time (the s domain) is given by:

$$G_{boost}(s) = \frac{V_{out}(s)}{d(s)} = \frac{-1.018 \times 10^6 s + 4.821 \times 10^8}{s^2 + 1.302 \times 10^4 s + 6.307 \times 10^6} \qquad (3.2)$$

3.2.2 State-space Averaging Method Transfer Function Estimation of the Proposed Boost Converter

One of the developed ways for obtaining the plant's transfer function and analyzing the features and behaviors of switch mode power supplies is state space averaging method [29]. The approach has shown to be a very useful and convenient tool in the applications of power electronics devices due to its great understanding and ease of derivation and implementation [30],[31]. Block diagram of a boost converter is given in Figure 3.2.

24
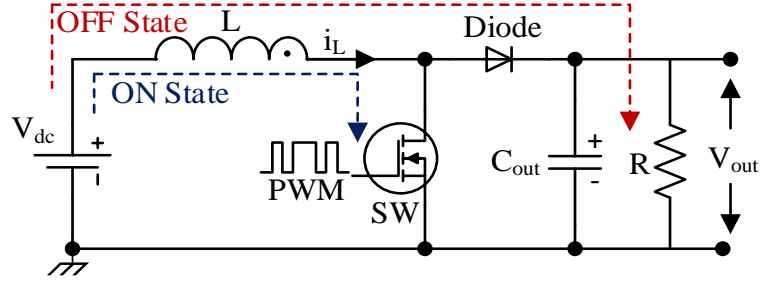
Figure 3.2: The block diagram of a boost converter.

Depending on the state of switch SW, the DBC has two current paths which is defined as ON and OFF operating states. Accordingly, the circuit analysis will be performed in two topologies. Circuit analysis of the DBC in both states is given in Table 3.4.

Table 3.4: Circuit analysis of the DBC in ON-OFF states.

[$State\ 1: SW\ ON, D\ OFF$]
$V_{dc} = L\dfrac{di_L}{dt};\ i_C = C\dfrac{dV_C}{dt};\ V_C = -i_C R;\ V_{out} = V_C$
[$State\ 2: SW\ OFF, D\ ON$]
$V_{dc} = L\dfrac{di_L}{dt} + V_{out};\ i_C = C\dfrac{dV_C}{dt};\ i_L = i_C + \dfrac{V_{out}}{R};\ V_{out} = V_C$

where $V_{dc}, L, i_L, i_C, C, V_C, R, V_{out}, V_{out}/R$ are input DC voltage, inductance, inductor current, capacitor current, capacitance, capacitor voltage, resistive load, output voltage and output current, respectively.

Internal state variables are the smallest subset of system variables that can accurately describe the system's overall state at any given time. The number of state variables in electric circuits is frequently, but not always, the same as the number of energy storage devices in the circuit, such as capacitors and inductors. Accordingly, current flowing through the inductor i_L and voltage across the capacitor V_C are the state variables since

25

the proposed boost converter consist of one inductor and one capacitor. State vector of the system is given by:

$$x = \begin{bmatrix} x_1 \\ x_2 \end{bmatrix} = \begin{bmatrix} i_L \\ V_C \end{bmatrix} \tag{3.3}$$

The state-space equations of the proposed boost converter are given by:

$$\dot{x} = \frac{dx}{dt} = \begin{bmatrix} \dfrac{di_L}{dt} \\ \dfrac{dV_C}{dt} \end{bmatrix} = Ax + BV_{dc} \tag{3.4}$$

$$y = V_{out} = Cx$$

Table 3.5 shows the analysis of the DBC in CCM and the derivation of its averaged state-space equations.

Table 3.5: Derivation of averaged state-space equations for the DBC in CCM.

$[State\ 1{:}\ SW\ ON, D\ OFF]$	$[State\ 2{:}\ SW\ OFF, D\ ON]$
(Time interval: 0<t<dT$_s$)	**(Time interval: dT$_s$<t<T$_s$)**
$\dot{x} = A_1 x + B_1 V_{dc}$	$\dot{x} = A_2 x + B_2 V_{dc}$
$y_1 = C_1 x$	$y_2 = C_2 x$
$A_1 = \begin{bmatrix} 0 & 0 \\ 0 & \frac{-1}{RC_{out}} \end{bmatrix}; B_1 = \begin{bmatrix} \frac{1}{L} \\ 0 \end{bmatrix}; C_1 = [0 \quad 1]$	$A_2 = \begin{bmatrix} 0 & \frac{-1}{L} \\ \frac{1}{C_{out}} & \frac{-1}{RC_{out}} \end{bmatrix}; B_2 = \begin{bmatrix} \frac{1}{L} \\ 0 \end{bmatrix}; C_2 = [0 \quad 1]$
$\begin{bmatrix} \dot{x}_1 \\ \dot{x}_2 \end{bmatrix} = \begin{bmatrix} 0 & 0 \\ 0 & \frac{-1}{RC_{out}} \end{bmatrix} \begin{bmatrix} x_1 \\ x_2 \end{bmatrix} + \begin{bmatrix} \frac{1}{L} \\ 0 \end{bmatrix} V_{dc}$	$\begin{bmatrix} \dot{x}_1 \\ \dot{x}_2 \end{bmatrix} = \begin{bmatrix} 0 & \frac{-1}{L} \\ \frac{1}{C_{out}} & \frac{-1}{RC_{out}} \end{bmatrix} \begin{bmatrix} x_1 \\ x_2 \end{bmatrix} + \begin{bmatrix} \frac{1}{L} \\ 0 \end{bmatrix} V_{dc}$
$V_{out} = [0 \quad 1] \begin{bmatrix} x_1 \\ x_2 \end{bmatrix}$	$V_{out} = [0 \quad 1] \begin{bmatrix} x_1 \\ x_2 \end{bmatrix}$

Averaging of the state-space model is carried out by combining ON and OFF set of equations as:

$$\dot{x} = [A_1 D + A_2(1-D)][x] + [B_1 D + B_2(1-D)]V_{dc}$$

$$V_{out} = [C_1 D + C_2(1-D)][x] \tag{3.5}$$

Averaged system (A), input (B) and output (C) matrices are derived by using steady-state duty cycle D as:

$$A = [A_1 D + A_2(1 - D)] \Rightarrow$$

$$A = \begin{bmatrix} 0 & 0 \\ 0 & \dfrac{-1}{RC_{out}} \end{bmatrix} D + \begin{bmatrix} 0 & \dfrac{-1}{L} \\ \dfrac{1}{C_{out}} & \dfrac{-1}{RC_{out}} \end{bmatrix} (1 - D) \tag{3.6}$$

$$A = \begin{bmatrix} 0 & 0 \\ 0 & \dfrac{-D}{RC_{out}} \end{bmatrix} + \begin{bmatrix} 0 & \dfrac{(D-1)}{L} \\ \dfrac{(1-D)}{C_{out}} & \dfrac{(D-1)}{RC_{out}} \end{bmatrix} \Rightarrow \tag{3.7}$$

$$A = \begin{bmatrix} 0 & \dfrac{(D-1)}{L} \\ \dfrac{(1-D)}{C_{out}} & \dfrac{-1}{RC_{out}} \end{bmatrix}$$

$$B = [B_1 D + B_2(1 - D)] \Rightarrow B = \begin{bmatrix} \dfrac{1}{L} \\ 0 \end{bmatrix} D + \begin{bmatrix} \dfrac{1}{L} \\ 0 \end{bmatrix} (1 - D) \tag{3.8}$$

$$B = \begin{bmatrix} \dfrac{D}{L} \\ 0 \end{bmatrix} + \begin{bmatrix} \dfrac{(1-D)}{L} \\ 0 \end{bmatrix} = \begin{bmatrix} \dfrac{1}{L} \\ 0 \end{bmatrix} \tag{3.9}$$

$$C = [C_1 D + C_2(1 - D)] \Rightarrow$$
$$C = [0 \quad 1] D + [0 \quad 1] (1 - D) \tag{3.10}$$

$$C = [0 \quad D] + [0 \quad (1 - D)] = [0 \quad 1] \tag{3.11}$$

The equation for steady-state operating point is written as:

$$\dot{x} = AX + BV_{dc} = 0 \tag{3.12}$$

$$AX = -BV_{dc} \tag{3.13}$$

$$A^{-1}(AX) = A^{-1}(-BV_{dc}) \Rightarrow X = A^{-1}(-BV_{dc}) \tag{3.14}$$

$$A^{-1} = \frac{adj(A)}{\det(A)} \Rightarrow adj(A) = \begin{bmatrix} \dfrac{-1}{RC_{out}} & \dfrac{(1-D)}{L} \\ \dfrac{(D-1)}{C_{out}} & 0 \end{bmatrix} \tag{3.15}$$

$$\det(A) = 0 - \left(\frac{1-D}{C_{out}} \times \frac{D-1}{L} \right) = \frac{(D-1)^2}{C_{out}L}$$

27

$$A^{-1} = \frac{1}{\dfrac{(D-1)^2}{C_{out}L}} \times \begin{bmatrix} \dfrac{-1}{RC_{out}} & \dfrac{(1-D)}{L} \\ \dfrac{(D-1)}{C_{out}} & 0 \end{bmatrix} \Rightarrow$$

(3.16)

$$A^{-1} = \begin{bmatrix} \dfrac{-L}{(D-1)^2 R} & \dfrac{-C_{out}}{(D-1)} \\ \dfrac{L}{(D-1)} & 0 \end{bmatrix}$$

$$B = \begin{bmatrix} \dfrac{1}{L} \\ 0 \end{bmatrix} \Rightarrow BV_{dc} = \begin{bmatrix} \dfrac{V_{dc}}{L} \\ 0 \end{bmatrix}$$

(3.17)

$$X = \begin{bmatrix} i_L \\ V_C \end{bmatrix} = \begin{bmatrix} \dfrac{-L}{(D-1)^2 R} & \dfrac{-C_{out}}{(D-1)} \\ \dfrac{L}{(D-1)} & 0 \end{bmatrix} \begin{bmatrix} \dfrac{-V_{dc}}{L} \\ 0 \end{bmatrix} \Rightarrow$$

(3.18)

$$X = \begin{bmatrix} \dfrac{V_{dc}}{(D-1)^2 R} \\ \dfrac{-V_{dc}}{(D-1)} \end{bmatrix}$$

Converting the state-space representation of the boost converter into an equivalent transfer function is performed as the followings:

$$sx(s) = Ax(s) + [(A_1 - A_2)X + (B_1 - B_2)V_{dc}]d(s)$$

(3.19)

$$V_{out}(s) = Cx(s) + [(C_1 - C_2)X]d(s)$$

(3.20)

$$x(s) = (sI - A)^{-1}[(A_1 - A_2)X + (B_1 - B_2)V_{dc}]d(s)$$

(3.21)

$$V_{out}(s) = C[(sI - A)^{-1}[(A_1 - A_2)X + (B_1 - B_2)V_{dc}]d(s)] \\ + [(C_1 - C_2)X]d(s)$$

(3.22)

$$\frac{V_{out}(s)}{d(s)} = C[(sI - A)^{-1}[(A_1 - A_2)X + (B_1 - B_2)V_{dc}] \\ + [(C_1 - C_2)X]$$

(3.23)

$$\frac{V_{out}(s)}{d(s)} = \frac{-sLV_{dc} + RV_{dc}(D-1)^2}{s^2[LRC_{out}(D-1)^2] + s[L(D-1)^2] + R(1-D)^4}$$

(3.24)

28

$$\frac{V_{out}(s)}{d(s)} = \frac{\left(\frac{-V_{dc}}{RC_{out}(D-1)^2}\right)s + \frac{V_{dc}}{C_{out}L}}{s^2 + \left(\frac{1}{RC_{out}}\right)s + \frac{(D-1)^2}{C_{out}L}} \tag{3.25}$$

$$= \frac{-0.002s + 1}{2.2 \times 10^{-9}s^2 + 2.5 \times 10^{-5}s + 1.25 \times 10^{-2}}$$

Step response characteristics of the proposed boost converter transfer functions derived by using Simulink® Control Design™ and state-space averaging techniques in terms of open-loop is given in Table 3.6.

Table 3.6: Open-loop step responses of the derived transfer functions.

Step Response Characteristics	Simulink® Control Design™	State-space Averaging Method
Rise Time (s)	0.0044	0.0042
Settling Time (s)	0.0081	0.0078
Settling Minimum	68.8104	72.0324
Settling Maximum	76.4336	79.9377
Overshoot (%)	0	0
Undershoot (%)	85.1766	81.2702
Peak	76.4336	79.9377
Peak Time (s)	0.0305	0.0151

System identification and properly developed model which should adequately capture the essential features of the system is of prime importance. Because of the presence of typical energy-storing components (capacitors and inductors) in power electronics, it will take some time for the system's energy state to change if it is disturbed. Transient time is the certain amount of time required by the system to transition from one energy state to another, and transient response is the measure of the magnitude and pattern of voltages and currents during this time. In this regard, a conducting time domain analysis of the system in terms of the step response characteristics given in Table 3.6 is required to derive a precise model. The open-loop step response characteristics of two techniques ensure that the transfer function estimation process has been accomplished successfully. The slight differences are caused by the properties of implemented techniques. In the Simulink Control Design, frequency response data of the converter is collected by applying perturbation to the duty cycle set-point with sinusoids of various frequencies and storing the load voltage correspondingly. On the

other hands, the state-space averaging is a formal process for obtaining the switching converter's small signal ac equations in vector and matrix forms.

Open-loop step, phase and magnitude responses of the transfer functions are given in Figure 3.3.

(a) Open-loop step response   (b) Open-loop frequency response
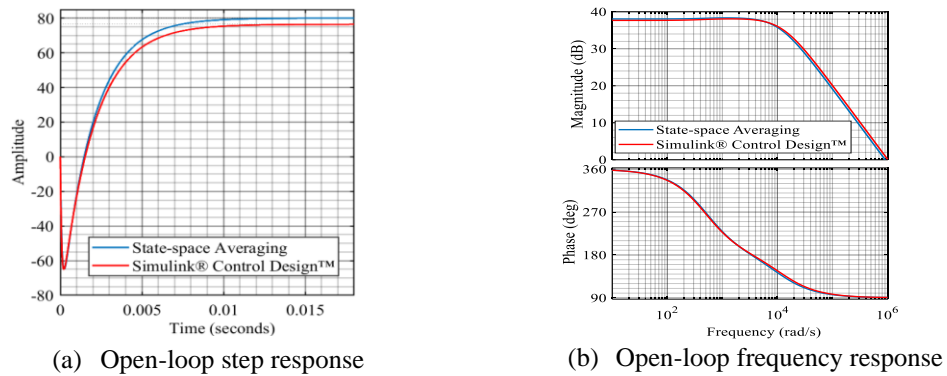
Figure 3.3: Time and frequency responses of derived transfer functions

3.3 Comparison of Commonly Used Mathematical Modelling Techniques

A mathematical model is a set of mathematical equations that are used to describe control systems. These models are useful for control system analysis and design. While analysis of a control system means finding the output by utilizing the input and the mathematical model of the system, designing of a control system refers to determining of the mathematical model by using the input and output of the system. Commonly used mathematical models are differential equation model, transfer function model and block diagram model. Figure 3.2 shows the block diagram of the proposed boost converter, and the transfer function model has been derived by using both Simulink® Control Design™ and state-space averaging technique. The differential equation model is given in Figure 3.4.
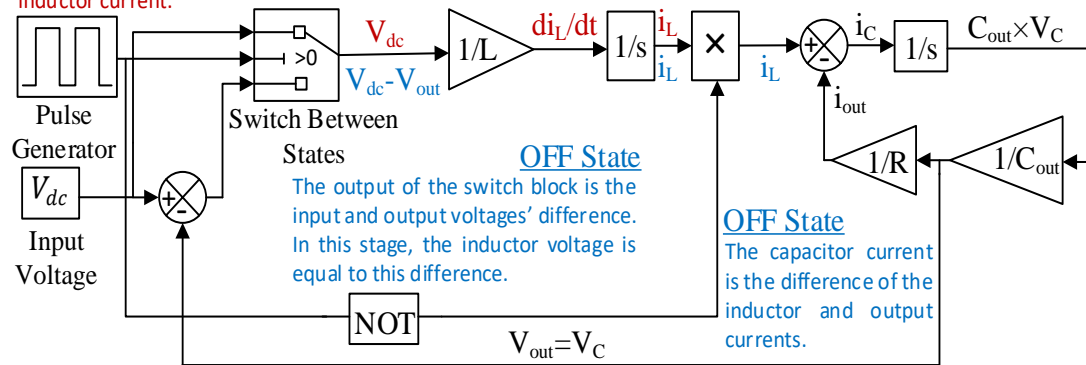
Figure 3.4: Differential equation model of the DBC.

Open-loop simulation output voltages of three mathematical models of the proposed boost converter are given in Figure 3.5. The figure shows that differential equation and transfer function models' transient responses resemble each other but differential equation model has a steady-state error. However, block diagram model exhibits better transient response with a steady-state error. In the controller design process, transfer function model of the boost converter will be used due to the following advantages:

- Easy determination of the system response to any given input.
- No differential terms are present as transfer function of a system consists of simple algebraic terms.
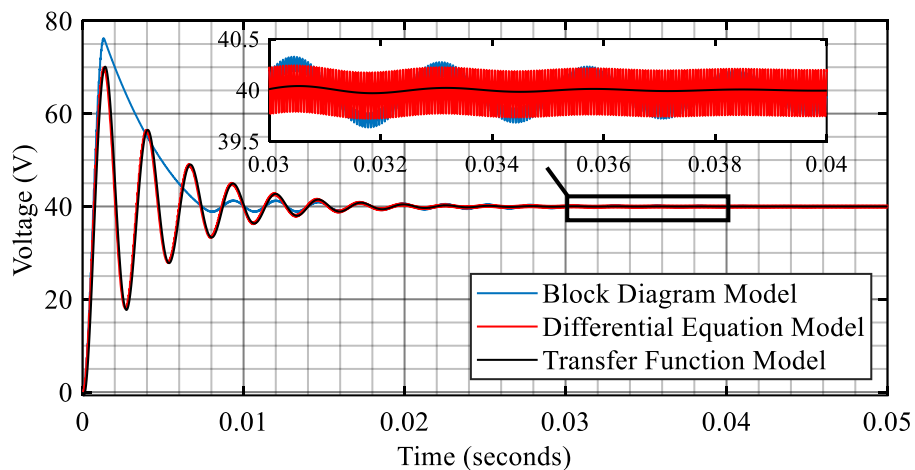
Figure 3.5: Comparison of output voltages for different mathematical models.

3.4 Controller and Reference Model Design

Due to the boost converters' intrinsic RHPZ, a voltage-mode controlled boost converter operating in CCM is more difficult to stabilize compared to other DC switch mode power supplies (SMPS) with Left Half Plane-zero (LHPZ). The input voltage, output voltage, load resistance, inductance, and output capacitance all affect the boost converter's double-pole and RHP-zero, further complicating the transfer function. To ensure proper functioning, it is necessary to understand the transfer function and have a mechanism to stabilize the converter. Plants whose input-output transfer functions have right half plane zeros are described as non-minimum phase systems. RHPZs are the mathematical description of the non-minimum phase systems. Physically, it refers to emergent of undershoot or to the systems goes in the wrong direction initially as impulse or step inputs are applied. Generation of the undershoot can be considered as some amount of time delay due to similar characteristics although it is not exactly time delay in terms of mathematical representation of the control systems. RHPZs have fundamental limits on the robustness on the system such as limitation on the bandwidth which is how fast of a change can be tracked. In this chapter, single PI, cascade PI and cascade PI controller-based model reference adaptive controller will be designed and implemented in the control of the proposed DBC. Additionally, their performances will be evaluated regarding transient and steady-state response characteristics.

3.4.1 PI Controller Design

The mathematical model of the plant is appropriately obtained by using both the Simulink® Control Design™ and the state-space averaging technique to forecast its response and observe its behaviors in both the time and frequency domains. Control systems are planned and executed in this regard to improve critical dynamic properties of the plant, such as stability, response time, steady-state error, and oscillations that make up the transient and steady-state. Because of its features of being simple to design, easily comprehensible, and very understandable, the Proportional-Integral (PI) feedback compensator structure is a commonly used controller. The general effects of each controller parameter proportional gain (K_p) and integral gain (K_i) on a closed-loop system are summarized in Table 3.7.

Table 3.7: The effects of PI controller parameters on transient response.

Closed-loop Response	Rise Time	Overshoot	Settling Time	Steady-state Error
K_p	Decrease	Increase	Small Change	Decrease
K_i	Decrease	Increase	Increase	Decrease

The unity feedback structure of the proposed DBC is given in Figure 3.6.
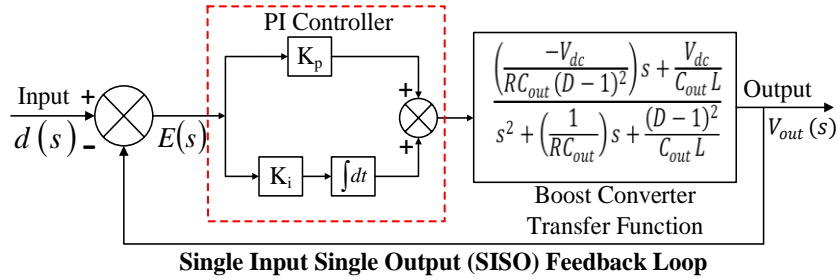
Figure 3.6: The unity feedback structure of the proposed DBC.

PI controller transfer function of the proposed DCB is given by:

$$G_{PI}(s) = \frac{0.0114s + 2.82}{s} \tag{3.26}$$

3.4.2 Cascade PI Controller Design

Cascade control is primarily utilized to ensure rapid disturbance rejection before it spreads to other parts of the plant. As illustrated in the block diagram in Figure 3.7, the simplest cascade control system has two control loops (inner and outer).
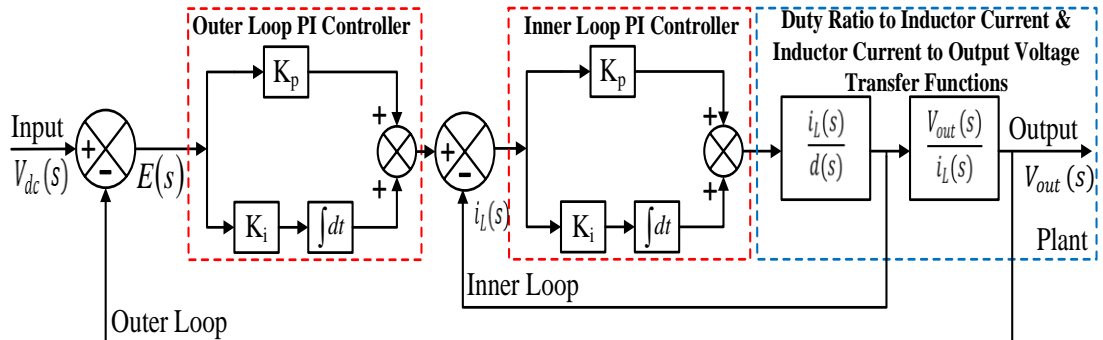
Figure 3.7: The cascade PI controller structure of the proposed DBC.

The inner loop of the proposed system is the transfer function of duty ratio to inductor current which is derived by using state-space averaging method as:

$$sx(s) = Ax(s) + [(A_1 - A_2)X + (B_1 - B_2)V_{dc}]d(s) \tag{3.27}$$

$$i_L(s) = Cx(s) + [(C_1 - C_2)X]d(s) \tag{3.28}$$

$$x(s) = (sI - A)^{-1}[(A_1 - A_2)X + (B_1 - B_2)V_{dc}]d(s) \tag{3.29}$$

$$i_L(s) = C[(sI - A)^{-1}[(A_1 - A_2)X + (B_1 - B_2)V_{dc}]d(s)] + [(C_1 - C_2)X]d(s) \tag{3.30}$$

$$\frac{i_L(s)}{d(s)} = C[(sI - A)^{-1}[(A_1 - A_2)X + (B_1 - B_2)V_{dc}] + [(C_1 - C_2)X] \tag{3.31}$$

$$\frac{i_L(s)}{d(s)} = \frac{sRC_{out}V_{dc} + 2V_{dc}}{s^2[LRC_{out}(1-D)] + sL(1-D) + R(1-D)^3} \tag{3.32}$$

$$\frac{i_L(s)}{d(s)} = \frac{1.76 \times 10^{-3}s + 40}{4.4 \times 10^{-9}s^2 + 0.5 \times 10^{-6}s + 0.025} \tag{3.33}$$

The inductor current to output voltage transfer function is derived in (3.34) and (3.35) as:

$$\frac{V_{out}(s)}{i_L(s)} = \frac{\frac{V_{out}(s)}{d(s)}}{\frac{i_L(s)}{d(s)}} \tag{3.34}$$

$$\frac{V_{out}(s)}{i_L(s)} = -\frac{(RV_{dc}\sigma^2 - LV_{dc}s)(R\sigma^3 + Ls\sigma + C_{out}LR\sigma s^2)}{(2V_{dc} + C_{out}RV_{dc}s)(R\sigma^4 + LsV_{dc} + C_{out}LR\sigma^2 s^2)}$$

where σ is *D-1*.

$$\frac{V_{out}(s)}{i_L(s)} = \frac{-8.8 \times 10^{-12}s^3 - 9.56 \times 10^{-8}s^2 + 0.025}{3.872 \times 10^{-12}s^3 + 1.32 \times 10^{-7}s^2 + 1.022 \times 10^{-3}s + 0.5} \tag{3.35}$$

The PI controller in the outer loop is the primary controller and it regulates the primary control variable input voltage V_{dc} by setting the set point of the inner loop. The PI controller in the inner loop is the secondary controller that ensures local disturbance

rejection before it propagates to the inductor current to output voltage transfer function. For the proper functioning of the cascade systems, the inner loop response must be faster than the outer loop. In this application, the inner loop bandwidth is selected 10 times higher than the outer loop bandwidth. Outer and inner loop PI controller transfer functions are given by:

$$G_{outer,PI}(s) = \frac{0.15s + 1000}{s} \tag{3.36}$$

$$G_{inner,PI}(s) = \frac{0.5s + 5}{s} \tag{3.37}$$

3.4.3 Cascade PI-based Model Reference Adaptive Controller Design

The control method employed by a controller which adapts to a controlled system with varying or initially uncertain parameters is known as adaptive control. Parameter estimation is the foundation of the adaptive control, which is an important constituent of system identification. In this chapter, the model reference adaptive controller (MRAC) is implemented with cascade PI controller. The main components of a MRAC system are the reference model, the adjustment mechanism, and the controller. The proposed cascade PI-based MRAC block diagram is given in Figure 3.8.
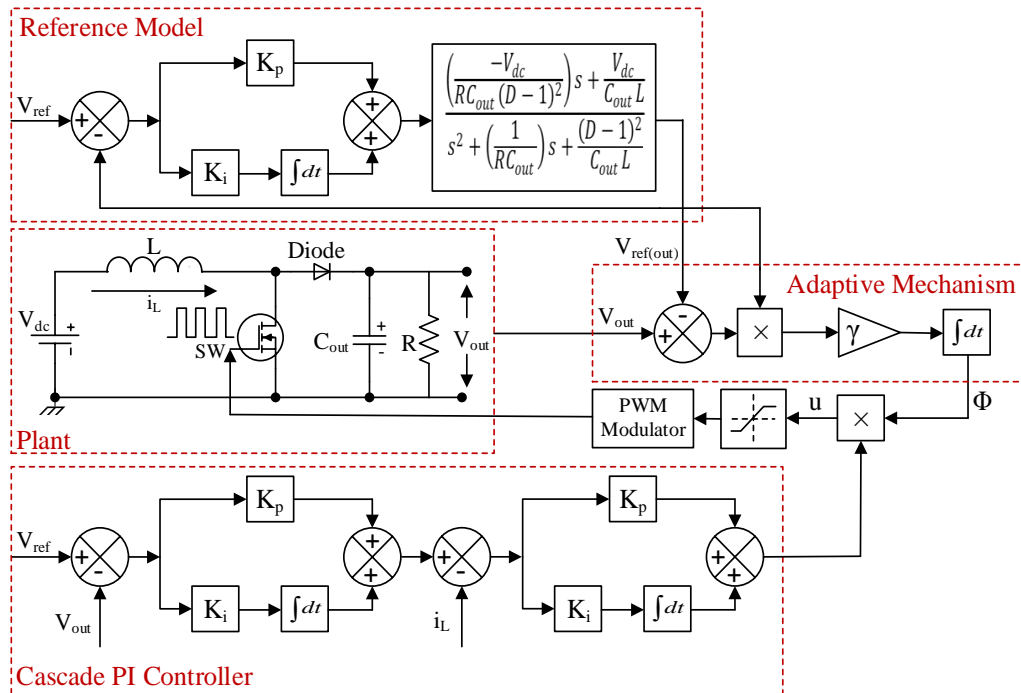
Figure 3.8: The block diagram of the proposed cascade PI controller based MRAC.

In the proposed control scheme, the adaptation mechanism adjusts the control action based on the error between the plant output V_{out} and the reference model output $V_{ref(out)}$ as given by:

$$\Phi = (V_{out} - V_{ref(out)})V_{ref(out)}\frac{-\Upsilon T_s z}{z - 1} \qquad (3.38)$$

where Φ, Υ and T_s are adaptation parameter, learning rate and sample time, respectively. The adjusted control signal u is calculated as multiplication of output of the cascade PI controller and adaptation parameter. The desired behavior of the closed-loop system is obtained by using learning rate of 0.04 and sample time of $1/10f_{sw}$ seconds.

3.4.4 Reference Model Design

The steady state duty cycle of the plant in terms of input-output voltage relationship is represented as:

$$\frac{V_{out}}{V_{dc}} = \frac{1}{(1 - D)} \qquad (3.39)$$

The maximum average inductor current is represented by the equation given by:

$$I_{L,avg,max} = \frac{V_{out}^2}{R_{out,min}V_{dc}} \qquad (3.40)$$

The maximum average inductor ripple current is the 20% of the average current that is represented by the equation given by:

$$\Delta I_L = 0.2I_{L,avg,max} \qquad (3.41)$$

Inductance value L of the inductor is represented by the equation given by:

$$L = \frac{V_{in}D}{f_{sw}\Delta I_L} \qquad (3.42)$$

Capacitor ΔV_C or output voltage ripple ΔV_{out} is the $\pm2\%$ of the average output voltage is represented by the equation given by:

$$\Delta V_C = \Delta V_{out} = 0.04 V_{out} \tag{3.43}$$

Capacitance value C of the capacitor is represented by the equation given by:

$$C = \frac{V_{in}D}{R_{out,min}f_{sw}\Delta V_C(1-D)} \tag{3.44}$$

The calculated values of the reference boost converter model parameters are given in Table 3.8.

Table 3.8: Calculated values of the reference boost converter model.

Parameters and Components	Values
Minimum Load Resistance (Ω)	10
Steady-state Duty Cycle	0.5
Maximum Average Inductor Current (A)	8
Maximum Average Inductor Current Ripple (A)	1.6
Inductor Value (mH)	0.3125
Output Voltage Ripple (V)	1.6
Capacitor Value (μF)	62.5

Transfer functions of the reference model boost converter and the PI controller are given by:

$$G_{ref,DBC}(s) = \frac{-0.0625s + 50}{4.88 \times 10^{-8}s^2 + 7.813 \times 10^{-5}s + 0.625} \tag{3.45}$$

$$G_{ref,PI}(s) = \frac{0.5 \times 10^{-5}s + 7.5}{s} \tag{3.46}$$

3.4.5 Discretization of the Designed Controllers and Reference Boost Converter Transfer Function

The controller in digital control systems is implemented on a digital computer, which means it will only run and have access to measurements at specific and discrete times before commanding the actuators. When a continuous system is converted to a discrete system, information is lost, which might have a detrimental impact on the proposed control system performance. Furthermore, discrete systems introduce delay into the feedback loop, reducing the controller's bandwidth. The bandwidth is an important

parameter since it specifies the maximum frequency at which the control system can respond. Considering these difficulties, selecting a proper discretization approach is critical.

The zero-order hold (ZOH), first-order hold (FOH), impulse invariant, bilinear (Tustin) approximation, and matched pole-zero technique are some of the most prevalent discretization methods used in control systems. The designed controllers and reference boost converter model is discretized using the bilinear (Tustin's approach) approximation. The most important argument for employing this method is that it produces the best frequency-domain match between continuous-time and discrete systems. The equation employed in the approximation of the z-domain transfer function relating to its continuous form (s-domain) with sample frequency one order of magnitude higher than the switching frequency $(T_s = 1/10f_{sw})$ is given by the following equation:

$$z = e^{sT_s} \approx \frac{1 + sT_s/2}{1 - sT_s/2} \tag{3.47}$$

3.5 Stability Analysis of the Proposed Control Scheme and Time Domain Performance Comparison

An adaptive controller adapts to variations and adjusts to changes in the process dynamics. In this regard, it must be set up in such a way that one can handle all variations in the system stated in Figure 3.9.
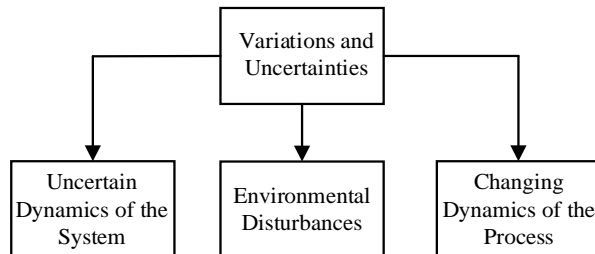
Figure 3.9: The variations in the process dynamics.

There are different techniques such as robust controller and gain scheduling developed to deal with uncertainty explicitly. Robust control approach is based on the ground of designing controller with enough stability and performance margin that it works

sufficiently well across the entire range of expected variations. The problem associated with this approach is that meeting requirements becomes more challenging as the range of uncertainty grows. At this point, gain scheduling approach can be considered as an alternative as it updates controller gains in the event of system state changes. Although gain scheduling works well for large variations, it does not work well for unexpected variations since gain sets and states must be known ahead of time. Adaptive control technique offers an effective alternative to resolve the arising problems associated with the use of both robust and gain scheduling approaches. The block diagram of the MRAC is given in Figure 3.10.
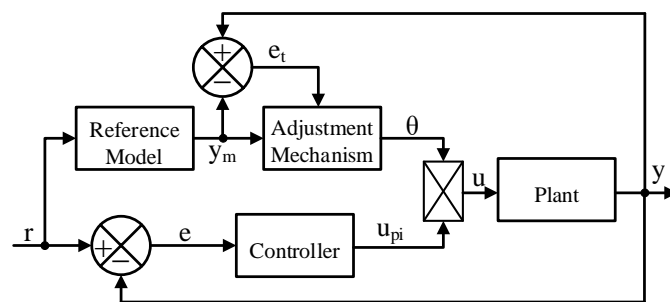
Figure 3.10: The block diagram of the MRAC.

Parameters of the PI controller based MRAC shown in Figure 3.10 with their names are given in Table 3.9.

Table 3.9: The PI controller based MRAC parameters.

Name	Parameter
Controller output	u_{pi}
Proportional gain	K_p
Intergral gain	K_i
Sample time	T_s
Error	e
Adaptation parameter	θ
Plant output	y
Reference model output	y_m
Learning rate	γ
Adjusted control signal	u

The control equation of the MRAC in discrete time (the z domain) is given by:

$$u_{pi}(k) = \left[K_p + K_i \frac{T_s z}{z-1}\right] e(k) \tag{3.48}$$

The adaptation mechanism whose function is control action adjustment based on the error between the plant output and the reference model output. The adaptation parameter equation is given by:

$$\theta = (y - y_m) y_m \frac{-\gamma T_s z}{z-1} \tag{3.49}$$

Designing principle of the MRAC by using MIT (a scalar parameter adjustment) rule requires identification of the reference model, the controller structure, and tuning gains for the adjustment mechanism [52],[53]. The formulations process of the MRAC begins with definition of the tracking error e_t given by:

$$e_t = y - y_m \tag{3.50}$$

A typical cost function of θ, $J(\theta)$, is formed by using the tracking error e_t as represented as [54]:

$$J(\theta) = \frac{1}{2} e_t{}^2(\theta) \tag{3.51}$$

The MIT rule describes the relationship between the change in theta and the cost function and it is a scalar parameter adjustment for adaptive control [55],[56]. Approximating a gradient descent process for an integral error squared performance requirement yielded this adjustment law. To determine how to update the parameter theta, an equation for the change in theta must be created [57]. Assumed that the change in $J(\theta)$ is proportional to the change in θ, the MIT sensitivity derivative equations is generated as [58]:

$$\frac{d\theta}{dt} = -\gamma \frac{\delta J(\theta)}{\delta \theta} = -\gamma e_t \frac{\delta e_t}{\delta \theta} \tag{3.52}$$

The tracking error e_t of the system regulated by implementation of the proposed Cascade PI controller based MRAC scheme under varying learning rates ($\gamma = 0.1, 0.5 \ and \ 1$) for reference voltages of 30 V, 40 V and 50 V applied at 0, 0.2 and 0.4 seconds, respectively is given in Figure 3.11. The simulation results show that the

tracking error e_t shows a tendency to become zero with a quick pace with the increasing learning rates.
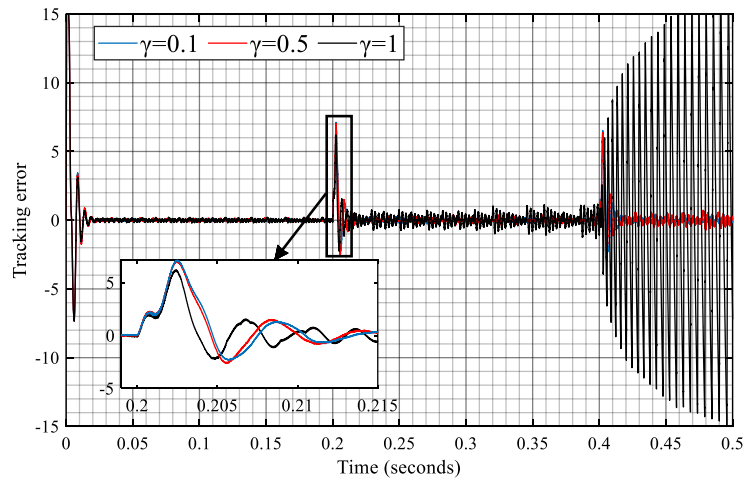
Figure 3.11: Tracking error of the system for varying learning rates.

The converging trajectories of the adaptation parameter θ for varying values of the learning rate γ when a step change from 30 V to 40 V is applied at 0.2 seconds as a controlled input to the system is shown in Figure 3.12. The simulation results indicate that the angle of inclination for the adaptation parameter decreases and consequently convergence of the adaptation parameter θ increases for larger values of γ. The settling time is reduced by increasing adaptation gain and the plant's output signal approaches the required reference model's response in less time.
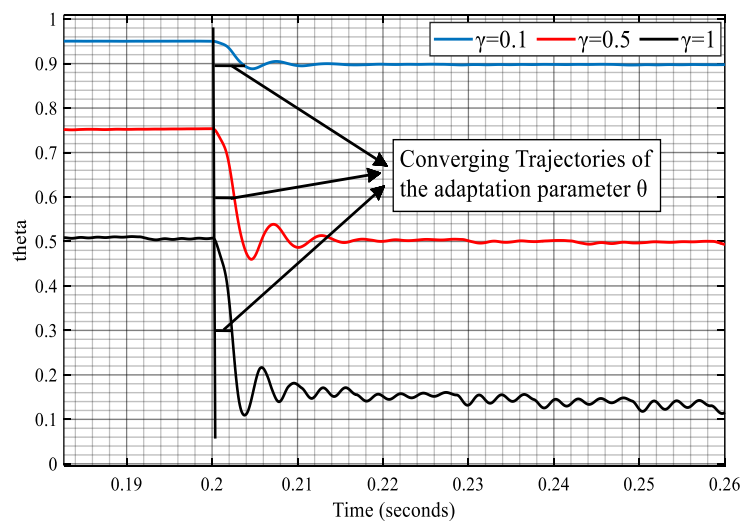
Figure 3.12: Converging trajectories of the adaptation parameter for varying learning rates.

Actual voltage outputs of the system in response to the step input voltages changing from 30 V to 40 V at 0.2 seconds and 40 V to 50 V at 0.4 seconds is applied are given in Figure 3.13.
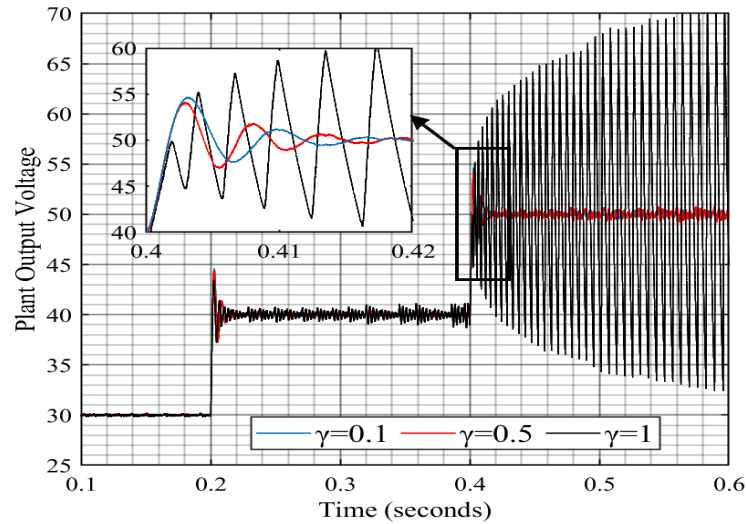
Figure 3.13: The plant output voltages for varying learning rates.

For larger γ values, the parameter'' convergence increases. This demonstrates that the controller is functional and that the equations have been correctly implemented. Larger values of γ, on the other hand, cause the control transients to oscillate as it can be seen in Figures 3.11, 3.12 and 3.13. The results of time domain performance analysis of the investigated and proposed algorithms are given in Table 3.10.

Table 3.10: Time domain performance analysis comparison.

Step Reponse Characteristics	Single PI Control	Cascade PI Control	Cascade PI-based MRAC
Rise Time (s)	5.9×10^{-4}	0.0012	0.0014
Settling Time (s)	0.0079	0.0064	0.00145
Settling Minimum	33.69	37.564	39.7
Settling Maximum	40.164	44.697	41.485
Overshoot (%)	0.41	11.7425	3.7125
Undershoot (%)	3.16	0.1	0
Peak	40.164	44.697	41.485
Peak Time (s)	0.001	0.0028	0.0025

Achieving a better tracking performance is possible with higher values of γ, however it leads to increase in the overshoot and choosing the best attainable value of the

learning rate regarding requirements for the purpose of coherent between performance parameters of the process such as rise time, overshoot and settling time.

3.6 Simulation and Experimental Results

Verification and validation of the proposed Cascade PI-based MRAC compared to the Single PI and Cascade PI controllers have been presented to illustrate the proposed controller scheme efficiency by considering the major concerns such as complex dynamics of the DBC due to NMP behavior and non-linearity. Additionally, the main issues in control system designing, e.g., uncertainty, intended simplicity, stochastic occurrences, and process variability have been considered. Accordingly, the performance of the proposed control has been evaluated by investigating three possible cases: (i) varying resistive loads, (ii) varying input voltages and (iii) varying reference voltages by using MATLAB® and Simulink®.

Figure 3.14 shows the DBC output voltages with resistive loads varying from 10 to 20 Ω (25% variation of the nominal value). The proposed Cascade PI-based MRAC strategy shows enhanced transient response with less oscillation.
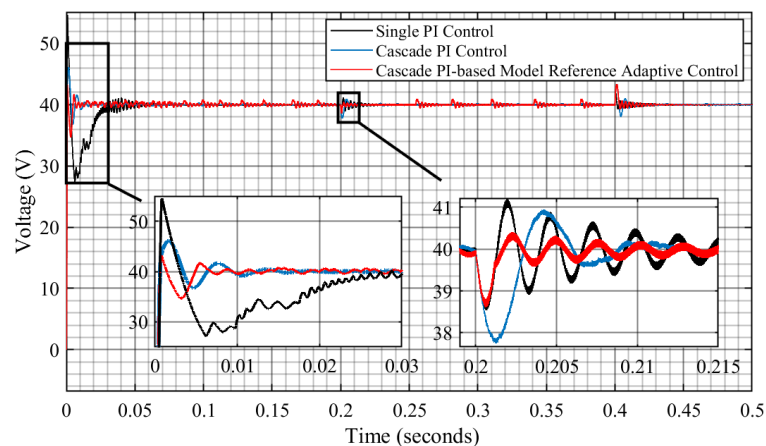
Figure 3.14: Comparison of control techniques under varying loads.

Figure 3.15 shows the DBC output voltage waveforms in the presence of both variable resistive load and different input voltages varying between 15 to 25 V (25% variation of the nominal value). Detrimental effect on the output voltage of single PI controlled DBC has been particularly clear because of implementing the load and input voltage variations together. The Cascade PI-based Reference Model Adaptive control strategy

shows enhanced transient response with less oscillation compared to other control techniques.
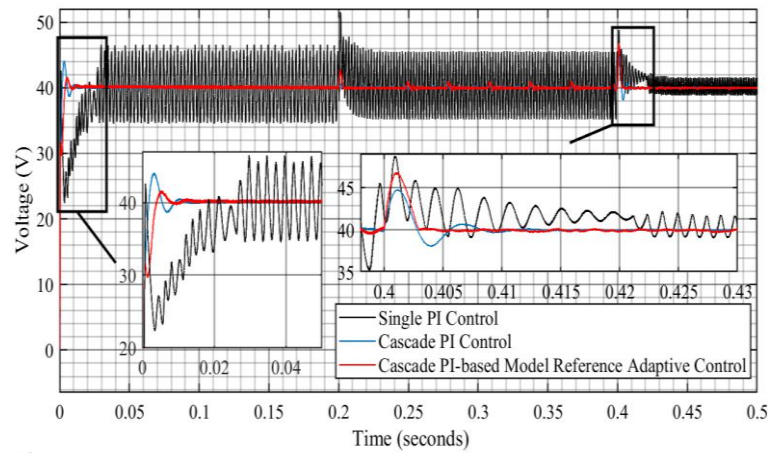
Figure 3.15: Comparison of control techniques under varying loads and different input voltages.

Figure 3.16 shows the DBC output voltage waveforms with reference voltages varying from 30 V to 50 V (25% variation of the nominal value). In comparison to other control systems, the Cascade PI-based Reference Model Adaptive control strategy shows improved transient response with less oscillation.
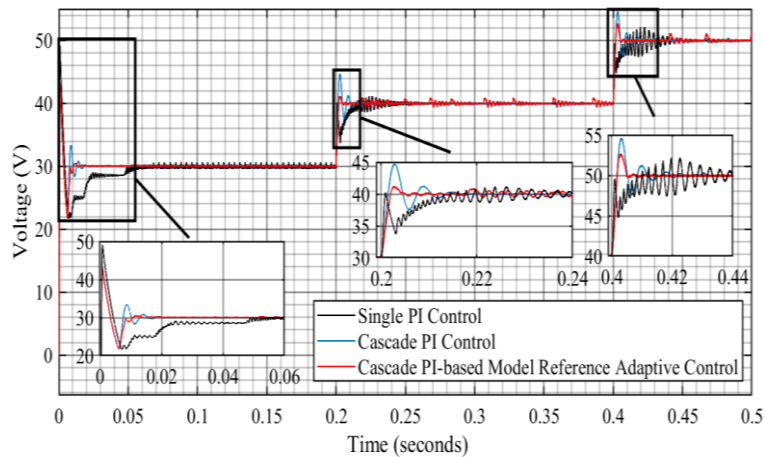
Figure 3.16: Comparison of control techniques for varying reference voltages.

Figure 3.17 shows the block diagram of the experimental set-up configuration for evaluating performance of the proposed Cascade PI-based Model Reference Adaptive Controller. The DC-DC boost converter, the electronic resistive load for continuous DC voltage output, the DC voltage source and the dSPACE real-time Interface (RTI) hardware-in-the-loop (HIL) control panels (RTI 1007 processor board, DS2004 High-

Speed A/D, and CP4002 Timing and Digital I/O boards) comprise up the overall system.
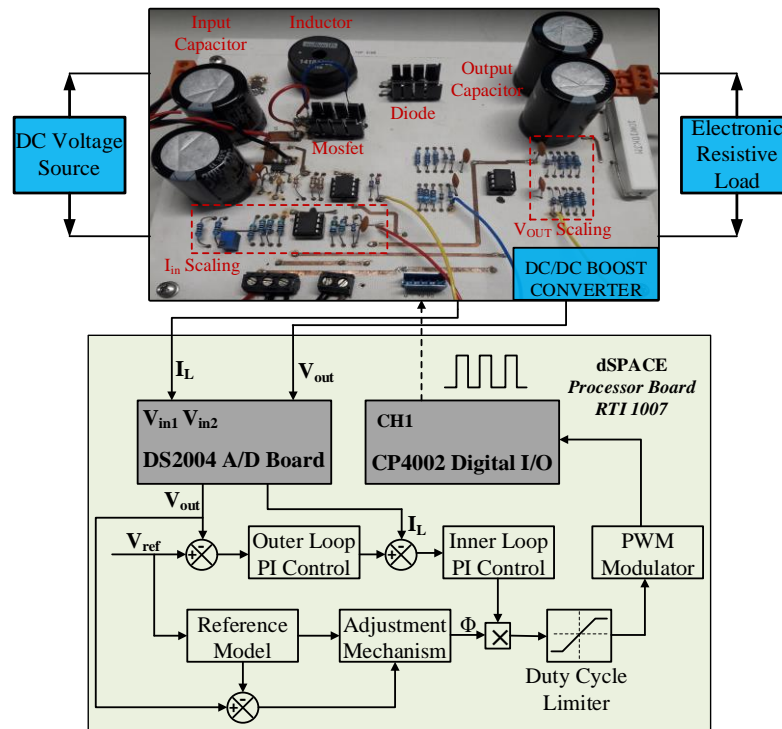
Figure 3.17: Experimental set-up for testing the proposed cascade PI controller based MRAC.

Test bench of the experiment is given in Figure 3.18. The designed boost converter relates to a 300 W programmable DC power supply (Tenma-72-2940 with 60 V maximum output voltage and 5 A maximum output current) which is used for DC input voltage. Additionally, an adjustable bench power supply with 3 outputs (AL991A-48 W power rating, -15 minimum output voltage and +15 maximum output voltage) is utilized to run the converter and a DC electronic load (3362F High Voltage DC Electronic Load 500V,60A,1800W) is used for setting the output load resistance. The proposed Cascade PI-based Model Reference Adaptive Control, Single PI and Cascade PI Control methods developed by using MATLAB/Simulink was implemented via dSPACE rapid control prototyping. The RTI block of the Modular Hardware/DS2004 High-speed A/D was used to convert the measured inductor current I_L and output voltage V_{out} as shown in Figure 3.17.
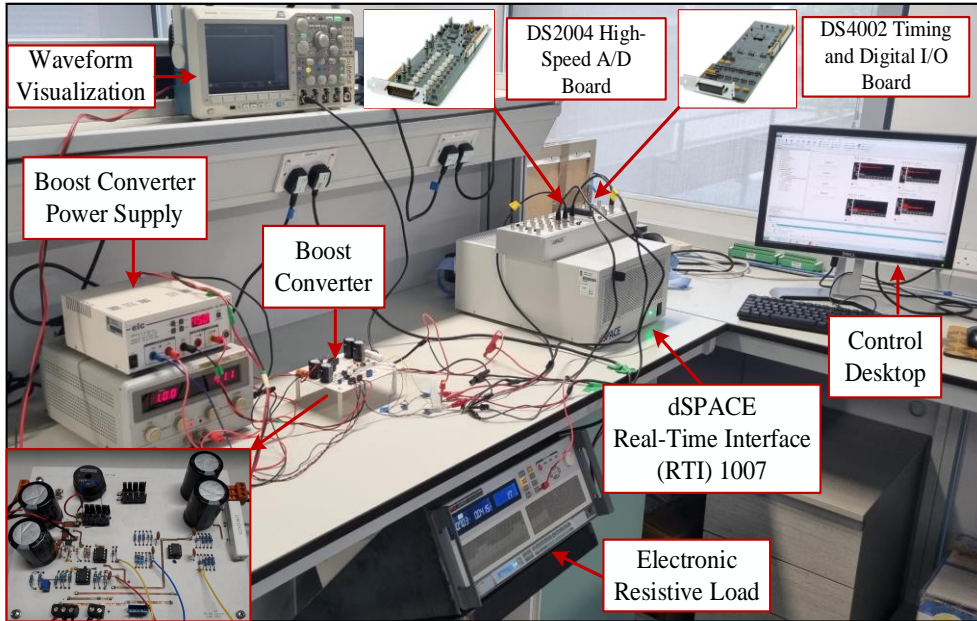
Figure 3.18: Test bench of the overall system.

The converted I_L and V_{out} were then implemented in the designed control techniques. Since the operating input voltage limits for DS2004 High-Speed A/D Board is specified as ranging from -10 V to +10 V, actual input current and output voltages are scaled down to meet the requirement. V_{out} and I_L were scaled down by a constant factor of 56 and 2.6, respectively. The scaling circuits are given in Figure 3.19.
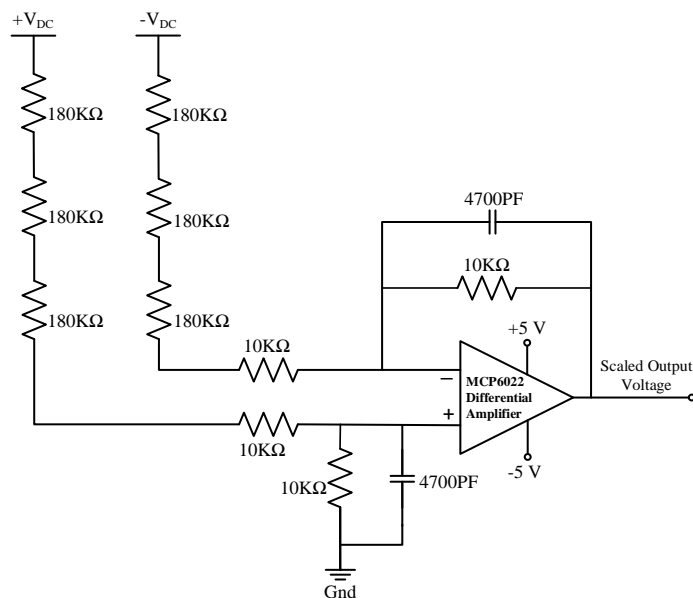
(a) Output voltage scaling circuit
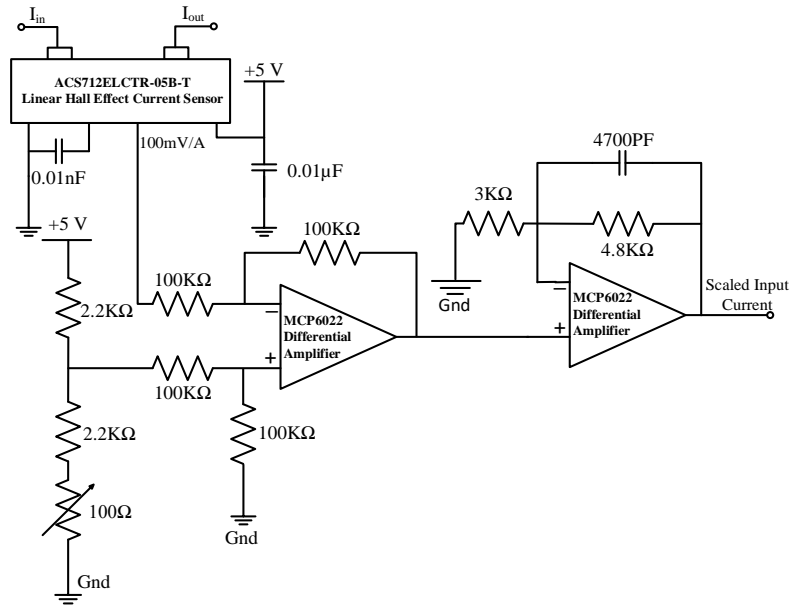
(b) Inductor current scaling circuit

Figure 3.19: Scaling circuits of output voltage and inductor current for providing their integration with dSPACE control panel.

The PWM signal for running the boost converter was generated using a regulated duty cycle in Simulink to attain the desired terminal voltage. dSPACE MATLAB/Simulink PC-based simulation platform Modular Hardware/DS4002 Timing and Digital I/O Board was used to implement the generated digital PWM signal.

Scaled output voltage and inductor current waveforms during step change of the load (reference voltage change from 25 V to 40 V) for the designed single PI controlled DBC is given in Figure 3.20.
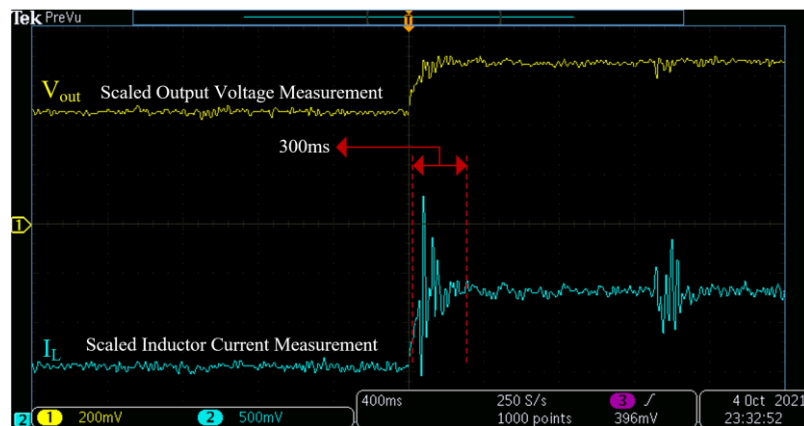
Figure 3.20: Output voltage and inductor current waveforms of the single PI controlled DBC

Scaled output voltage and inductor current waveforms during step change of the load (reference voltage change from 25 V to 40 V) for the designed cascade PI controlled DBC is given in Figure 3.21.
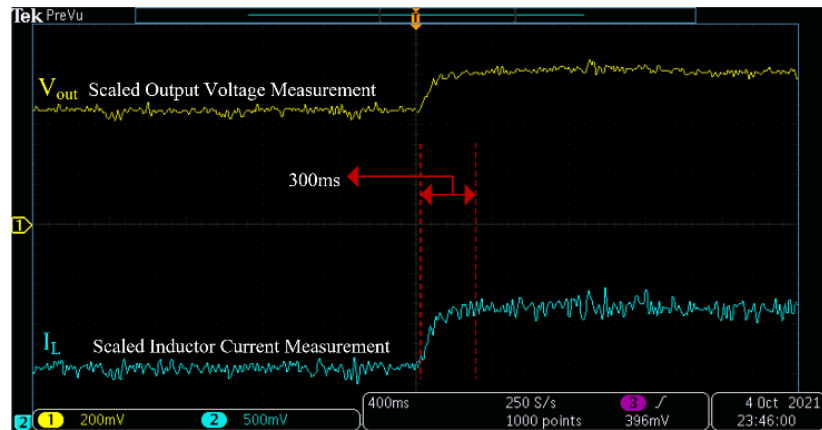
Figure 3.21: Output voltage and inductor current waveforms of the cascade PI controlled DBC

Scaled output voltage and inductor current waveforms during step change of the load (a reference voltage change from 25 V to 40 V) for the designed DBC controlled by cascade PI-based reference model adaptive control technique is given in Figure 3.22.
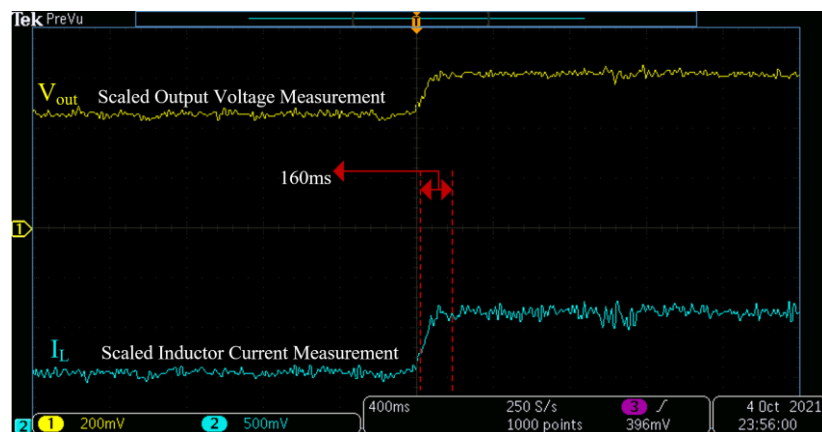
Figure 3.22: Output voltage and inductor current waveforms of the DBC controlled with the proposed cascade PI controller based MRAC

Application of the single PI controller for the boost converter refers to voltage-mode control which also known as duty-cycle control. This control scheme uses a single loop to adjust the duty cycle in direct response to changes in output voltage. Because of the boost converter's inherent RHPZ, a voltage-mode controlled boost converter

operating in continuous conduction mode is more difficult to stabilize and it means to have poor transient response with disturbance occurrence as shown in Figure 3.20.

The cascade PI control of the boost converter refers to current-mode control that contains two loops (an inner current loop and outer voltage loop) with inner and outer PI controllers. The cascade control system performs substantially better in rejecting disturbance, although the set-point tracking performances are nearly comparable, based on the two response plots given in Figures 3.20 and 3.21. Moreover, even if the RHPZ is at a low frequency, compensation for cascade PI controlled boost converters is significantly easier than compensation for single PI controlled boost converters. Since the crossover frequency has no minimum requirement in cascade control, the system can be stabilized regardless of the RHPZ frequency. The inner current loop eliminates the filter's ringing frequency, and good performance is attained even with a low voltage feedback loop crossover frequency.

The experimental results are consistent with the simulation outcomes. The suggested cascade PI-based reference model adaptive control technique compared to other two methods improved transient response with considerable disturbance rejection, according to both experimental and analytical results.

3.7 Summary

A DC-DC boost converter with Cascade PI Controller-Based Robust Model Reference Adaptive Control (MRAC) is presented in this chapter. The boost converte''s non-minimum phase behaviour owing to right half plane zero is a challenge, and its non-linear dynamics hinder the control process while in continuous conduction mode (CCM). By combining aspects of a cascade PI control loop with MRAC characteristics, the suggested control strategy effectively overcame complexities and challenges. Fundemantal objective of integrating MRAC to the cascade PI controlled boost converter was to maintain consistent performance in the presence of uncertainty, variations in plant parameters and non-linear dynamics.

Using MATLAB/Simulink, the comparative analysis with single PI and cascade PI controllers demonstrates the ability of the proposed control system to track the desired

signals and regulate the plant process variables in the most beneficial and optimised way without delay and overshoot is verified.

Furthermore, the suggested control schema performance has been experimentally evaluated by utilizing MATLAB/Simulink/Stateflow on the dSPACE RTI 1007 processor, DS2004 High-Speed A/D, and CP4002 Timing and Digital I/O boards. The performance characteristics of the proposed control technique has been compared with single and cascade PI controllers. The experimental and analytical results show that the proposed control method increased tracking speed by two times while also providing better disturbance rejection.

Chapter 4

Unity Proportional Gain Resonant and Gain Scheduled Proportional (PR-P) Controller Based Variable Perturbation Size Real-time Adaptive Perturb and Observe (P&O) MPPT Algorithm

4.1 Introduction

Photovoltaic (PV) energy has gained wide currency among prevalent renewable energy sources with significant developments in energy conversion and storage technologies. Furthermore, the PV energy systems attracts a great deal of attention owing to considerable advantages such as reliability and long-life, advanced manufacturing process, static and noise-free operations, increasing efficiency, decreasing prices, flexibility of construction and availability of government support and incentives [1], [2], [3], [4]. The evolving requirements and needs in PV energy systems has prompted authorities to do comprehensive studies in this field with primary motivations of increasing the efficiency, reliability and useful life-span of the PV systems and conversely reducing the cost and space from generation to delivering of the energy [5], [6].

Employing MPPT algorithms is essential in terms of improving energy harvesting efficiency in PV systems since electrical characteristics of PV modules are weather dependent and manifested in the output current and voltage waveforms under variations of irradiance and ambient temperature [7]. A series of recent studies indicated that soft computing intelligent systems such as particle swarm optimization (PSO) [8], fuzzy logic (FL) [9], [10], genetic algorithms (GA) [11], artificial neural networks (ANN) [12], machine learning (ML) [13], differential evolution (DE) [14],

ant colony optimization (ACO) [15], artificial bee colony (ABC) [16], grey wolf (GW), firefly (FF) [17] and cuckoo search (CS) [18] have come into widespread use in the development of MPPT techniques for the PV systems as a result of increasing use of hardware-in-the-loop (HIL) and RTI applications.

Soft computing intelligent systems, although having higher efficiency in the presence of abrupt and dynamic irradiance and temperature changes, have several evident disadvantages; for instance, complexity, computational burden, implementation cost, slow tracking speed, lacking flexibility, sensitivity of initialization for multi-level optimization [19], [7]. Consequently, many existing studies in the literature have re-visited the conventional MPPT methods such as P&O, hill climbing (HC) and incremental conductance (IC) for further examination to improve [20].

P&O MPPT technique is one of the most common and the simplest algorithms that stands out amongst others with its fast convergence to MPP [21], [22]. However, continuous oscillations around the MPP with respect to the imposed perturbation and production of average MPP value lower than it could be due to large step size are considered as shortcomings of this method [23]. Depending on the perturbation size, the oscillation results in certain amount of power loss and improper choice of the step size leads to poor tracking performance [24].

In this chapter, a novel PR-P controller based variable perturbation size real-time adaptive P&O MPPT algorithm is presented. The proposed control scheme resolved the drawbacks of conventional P&O MPPT method associated with the use of constant perturbation size that leads to poor transient response and high continuous steady-state oscillations. The prime objective of using the PR-P controller is to utilize inherited properties of the signal produced by the controller's resonant path and integrate it to update best estimated perturbation that represents the principle of ESC operation to use in P&O algorithm that characterizes the overall system learning-based RTA. Additionally, utilization of internal dynamics of the PR-P controller eliminates the necessity for assistive methods and decreases the number of control system components that overcomes the challenges namely, complexity, computational burden, implantation cost and slow tracking performance in association with commonly used soft computing intelligent systems and adaptive control strategies.

4.2 Proposed Control Structure

The proposed control method is developed by using the properties of PR-P controller, extremum seeking control (ESC) technique and conventional P&O MPPT algorithm together. Block diagram of the control structure is given in Figure 4.1.

In the proposed control structure, PR-P controller is the key component since it performs multiple tasks simultaneously that are error compensation and modulation signal generation from its resonant path as shown in Figure 4.1. The PR-P controller enables to obtain high gain at any frequency. In this study, it is designed at pulse width modulation (PWM) switching frequency where the signal distortion in the system occurs due to harmonics. Although the ESC is a relatively straightforward controller, the controller is more complicated as many parameters need to be tuned. Modulation signal generation from the unity gain resonant path of the PR-P controller dispenses with the need for using high and low pass filters as well as modulating signal in ESC implementation. Stated in other words, quickly and robustly converging of the system on the optimal solution for perturbation is achieved by utilizing the inherited properties of the PR-P controller.
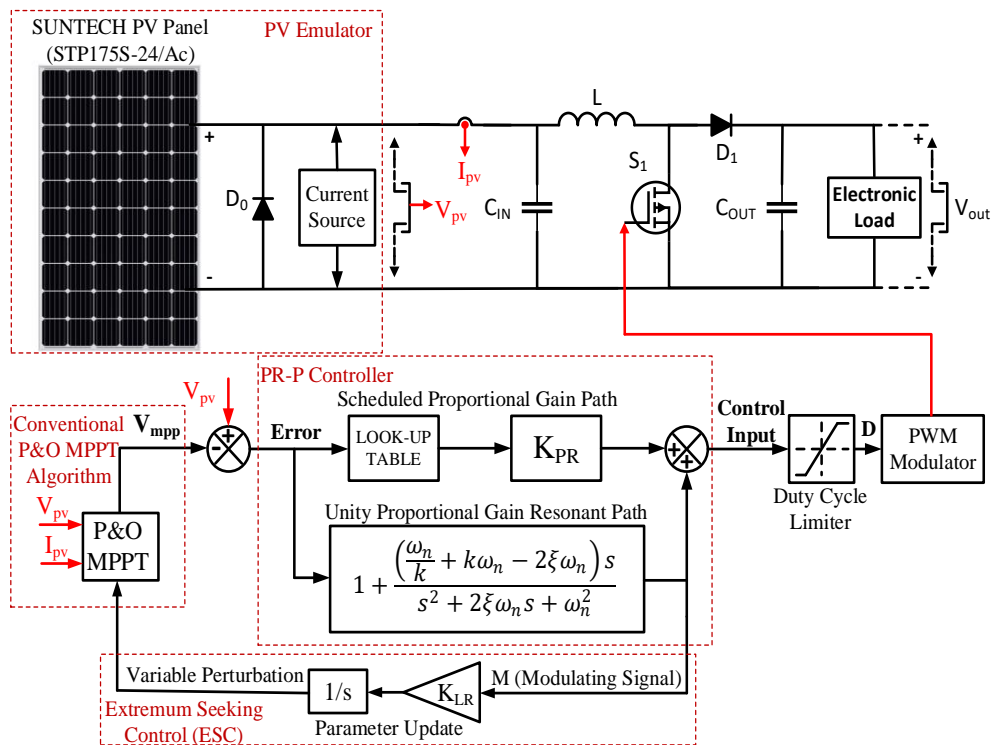
Figure 4.1: Block diagram of the proposed control structure.

4.2.1 The PR-P Controller Design

The PR controller has become widely used current regulator for grid-connected single-phase inverter systems [25], [26], [27]. The most important feature of the PR controller is its capability of tracking repeating signals with zero steady-state error by producing high gain at specified frequency.

Figure 4.2 shows the frequency response of intended notch filter. $G(s)$ is the physically unrealizable transfer function of which order of numerator is greater than denominator. There is a gain rising at 40 dB/decade since there are two unanswered zeros, thus the high frequency signals are to pass through altered. $G(s).s_1$ shows that addition of a pole with a cut-off frequency that is k times larger than the natural frequency dragged the high frequency magnitude down by 20 dB/decade. $G(s).s_1.s_2$ shows that addition of a complementary pole with a cut-off frequency that is k times smaller than the natural frequency bended down the high frequency magnitude by 20 dB/decade to the zero db. In this application, $G(s)$ is generated by locating a pair of zeros with damping ratio of 0.5 at the PWM switching frequency of the boost converter which is 20 kHz corresponding to the resonant frequency of the proposed PR-P controller. The parameter k that determines cut-off frequencies of the complementary poles (symmetrical poles located around the resonant frequency) is chosen 2 which establishes enough width for the notch and, consequently, provides a sufficient gain in the case of variation around resonant frequency.
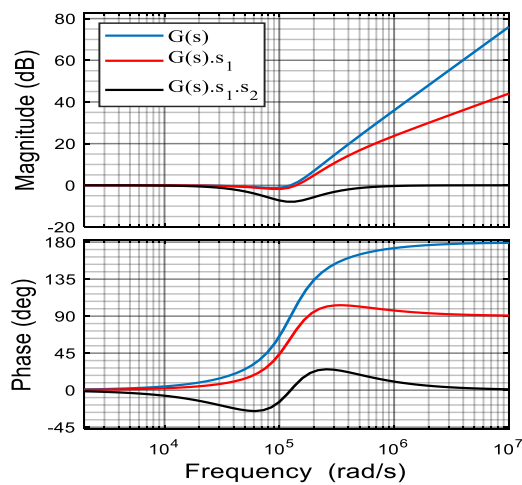
Figure 4.2: The notch filter dynamics-based PR controller.

The transfer function of the resonant path of the proposed PR-P controller $G_{PR}(s)$ is the reciprocal of the notch filter transfer function $G_{notch}(s)$ is presented as:

$$G_{notch}(s) = G(s).s_1.s_2$$

$$G_{PR}(s) = \frac{1}{G(s).s_1.s_2} = \frac{\omega_n{}^2}{s^2 + 2\xi\omega_n s + \omega_n{}^2} . \frac{s + k\omega_n}{k\omega_n} . \frac{s + \frac{\omega_n}{k}}{\frac{\omega_n}{k}} \qquad (4.1)$$

$$G_{PR}(s) = \frac{1.579 \times 10^{10}s^2 + 4.961 \times 10^{15}s + 2.494 \times 10^{20}}{1.579 \times 10^{10}s^2 + 1.984 \times 10^{15}s + 2.494 \times 10^{20}} \qquad (4.2)$$

Addition of the proportional gain K_{PR} , ($K_{PR} = 0.5$), to the PR path puts the proposed controller into final form as:

$$G_{PRP}(s) = K_{PR} + G_{PR}(s)$$

$$G_{PRP}(s) = \frac{2.369 \times 10^{10}s^2 + 5.953 \times 10^{15}s + 3.741 \times 10^{20}}{1.579 \times 10^{10}s^2 + 1.984 \times 10^{15}s + 2.494 \times 10^{20}} \qquad (4.3)$$

The magnitude and phase responses of the designed PR-P controller is given in Figure 4.3. The highest gain and phase shift of the proposed PR-P controller occurs at the PWM switching frequency of the boost converter ($\omega_n = 20\ kHz$). The phase response shows that the phase shift is zero for low and high frequencies.
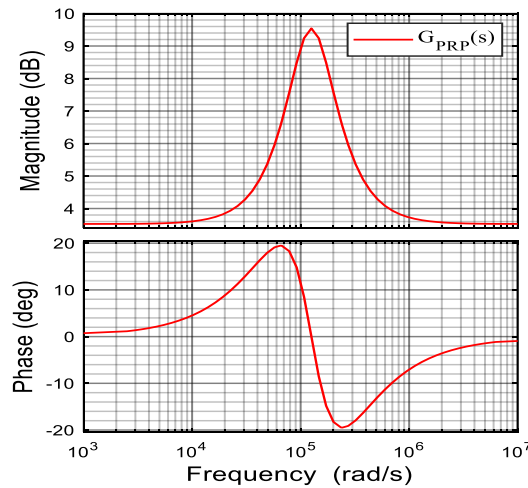
Figure 4.3: Magnitude and phase responses of the designed PR-P controller.

Unity feedback control structure of the boost converter with the proposed PR-P controller in s-domain from feedback error to control input to the plant is given in Figure 4.4.
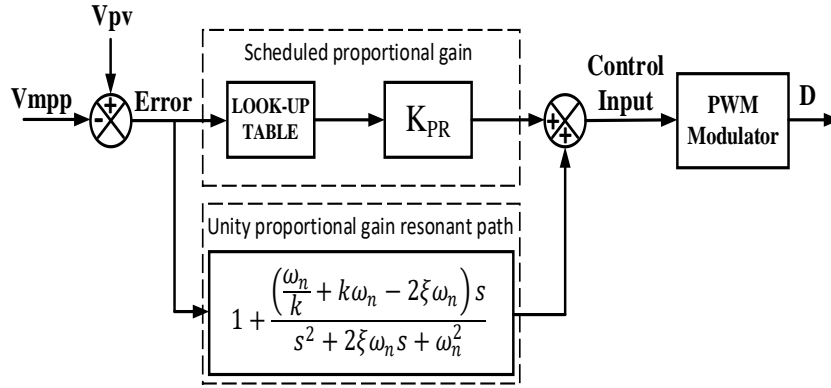
Figure 4.4: Unity feedback control structure of the boost converter with the proposed PR-P controller.

4.2.2 Discretization of the PR-P Controller

In digital control systems, the controller is implemented on a digital computer. The main benefits of digital controls are flexibility, reduced cost, improved user interface, and the ability to implement adaptive solutions. Transformation from a continuous system to a discrete system causes loss of information which may negatively impact the proposed control system performance. Additionally, discrete systems add delay into the feedback loop which decreases bandwidth of the controller. The bandwidth is very essential parameter as it determines the upper limit on the frequency that the control system can respond. Regarding these challenges, choosing a proposer discretization method is of prima importance.

There are several discretization methods commonly used in control systems, namely, zero-order hold (ZOH), first-order hold (FOH), impulse invariant, bilinear (Tustin) approximation and matched pole-zero method. Bilinear (Tustin's method) approximation is used for the discretization of the proposed PR-P controller. The Main reason of using this method is due to its property of yielding the best frequency-domain match between the continuous-time and discrete systems. The equation employed in the approximation of the z-domain transfer function relating to its continuous form (s-domain) is given by:

$$z = e^{sT_s} \approx \frac{1 + sT_s/2}{1 - sT_s/2} \tag{4.4}$$

The discretization $G_{PR}(z)$ of a continuous transfer function $G_{PR}(s)$ with sample frequency one order of magnitude higher than the switching frequency ($T_s = 1/10f_{sw}$) is given by:

$$G_{PR}(z) = G_{PR}(s'), \qquad s' = \frac{2z - 1}{T_s z + 1}$$

$$G_{PR}(z) = \frac{1.334z^2 - 1.276z + 0.2217}{z^2 - 1.2767z + 0.5553} \tag{4.5}$$

4.2.3 Extremum Seeking Control (ESC) Algorithm

Extremum seeking control (ESC) is an adaptive equation free method of controlling non-linear systems. The operating principle of this method is to add sinusoidal perturbation to the controller and consequently this perturbation allows the algorithm locally to optimize an objective function which is tracking the maximum power point in PV systems. The block diagram of the ESC is given in Figure 4.5. Unlike optimal control theory method such as linear quadratic regulator (LQR) which requires a linear model of the system and a quadratic objective function to do optimization, ESC and P&O type of algorithms do not require a system model [28]. Furthermore, the optimization is done offline and produces static gains which will stay the same even though the dynamics of the objective system changes over time in LQR. The use of ESC and P&O with the PR-P controller overcome the limitations associates with the use of several optimal control theory methods in PV systems.
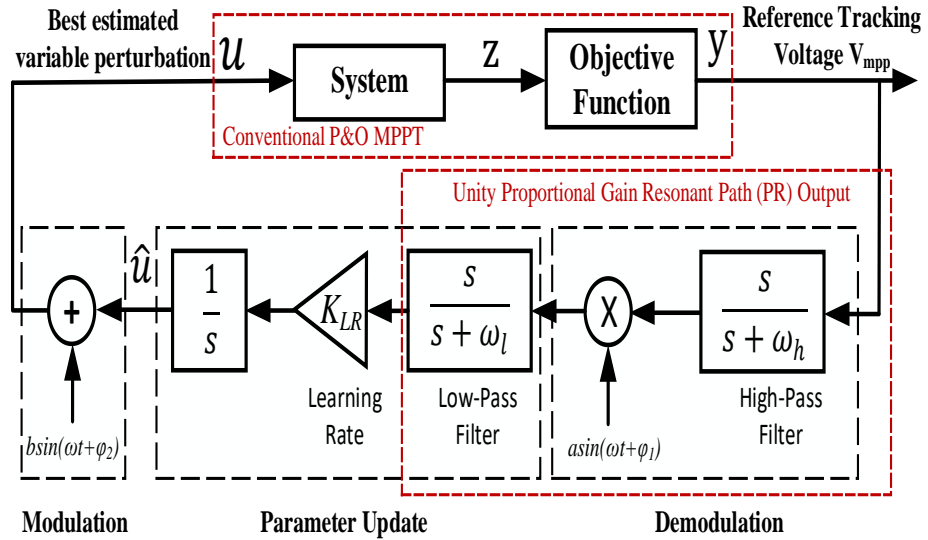
Figure 4.5: The block diagram of extremum seeking control.

ESC algorithm consists of the following stages to tune a parameter value which is generating variable perturbation for the conventional P&O MPPT algorithm that converges quickly to the maximum power point voltage and tracks it efficiently in this study:

- **Modulation:** The value of the optimization parameter is perturbed with a low-amplitude sinusoidal signal.

- **System response:** The targeting system being optimized reacts to the parameters perturbations.

- **Demodulation:** The objection function output signal is multiplied by a sinusoidal signal. The frequency of both modulation and demodulation signals must be the same. A high pass filter is used to remove bias from the objective function output signal. A small phase shift can be implemented to provide better line-up with the perturbation signal.

- **Parameter update:** The demodulating signal is integrated in this stage to update the parameter value corresponding to state of the integrator. A low-pass filter is used to remove high frequency noise.

Parameters of the ESC algorithm with their names are given in Table 4.1.

Table 4.1: Extremum seeking control parameters.

Name	Parameter
Estimated paramater value	$\hat{u}$
Modulated signal	u
Objective function output	y
Forcing frequency	ω
Modulation signal	$b\sin(\omega t + \varphi_2)$
Demodulation signal	$b\sin(\omega t + \varphi_1)$
Low-pass filter cut-off frequency	ω_l
Higg-pass filter cut-off frequency	ω_h

Execution of the ESC algorithm on the power-voltage (P-V) characteristics curve of a PV module is given in Figure 4.6.
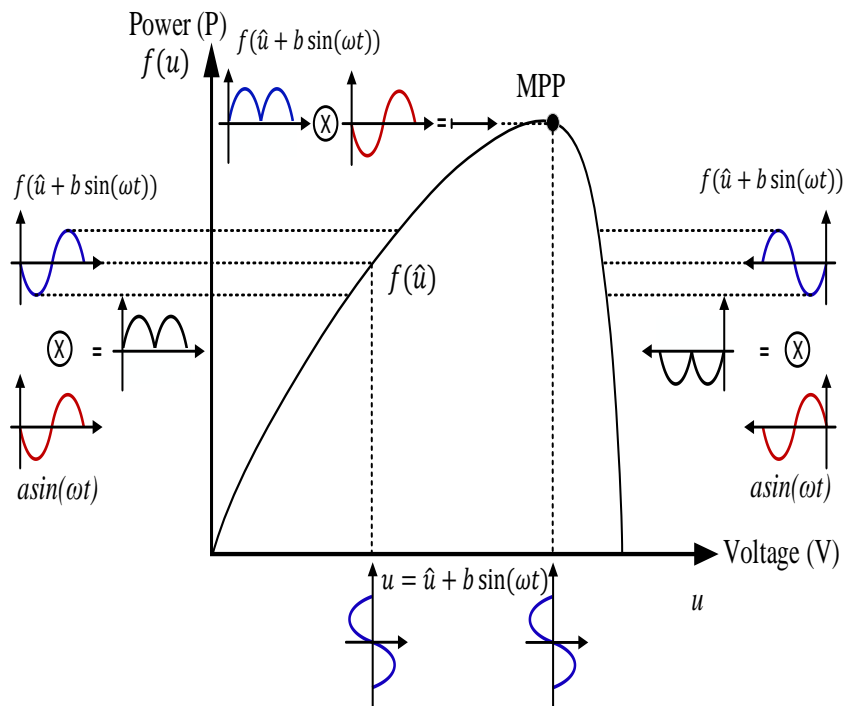
Figure 4.6: Execution of the ESC algorithm on the P-V curve.

The left side of the Figure 4.6 demonstrates extremum seeking for an increasing portion of the objective function curve (P-V curve). The modulated signal u is the sum of the current estimated voltage V and the modulation signal $b\sin(\omega t + \varphi_2)$ with the same phase as the modulation signal. Applying $f(u)$ produces a perturbed objective function which is the power P. A positive signal is produced by multiplying the

perturbed objective function by the demodulation signal $bsin(\omega t + \varphi_1)$. Integrating this signal increases the value of V, moving it closer to the objective function's peak.

The right side of the Figure 4.6 demonstrates extremum seeking for a decreasing portion of the objective function curve (P-V curve). In this case, applying $f(u)$ produces a perturbed objective function that is 180 degrees out of phase from the modulation signal $bsin(\omega t + \varphi_2)$. When multiplied by the demodulation signal $bsin(\omega t + \varphi_1)$, a negative signal is produced. Integrating this signal reduces the value of V, moving it closer to the objective function's peak.

The top of the P-V curve demonstrates extremum seeking for a flat portion of the objective function curve (P-V) curve. In this case, $f(u)$ yields a perturbed objective function close to zero. The value of V is not significantly changed when multiplied by the demodulation signal and integrated, which is near the MPP.

4.2.4 Conventional P&O Algorithm

The P&O MPPT approach one of the most basic and widely used algorithms in PV systems which does not require a system model and a quadratic objective function. It can run real time and adapt to the changing dynamics of the system over time. Operation principle of the algorithm is based on a trial-and-error approach to finding and tracking the MPP.

To compute the power, the approach requires merely measuring the PV array's current and voltage and accordingly perturbing the duty cycle based on a comparison of the initial and present values of the power and voltage until attaining the MPP. Continuous oscillations around the MPP in relation to the imposed perturbation, as well as the development of an average MPP value lower than it could be due to the huge step size, are regarded flaws in this method.

The oscillation loses a certain amount of power depending on the size of the perturbation, and improper step size selection leads to poor tracking performance. The flowchart of the algorithm and accordingly its execution on the P-V characteristics curve are given in Figures 4.7 and 4.8, respectively.
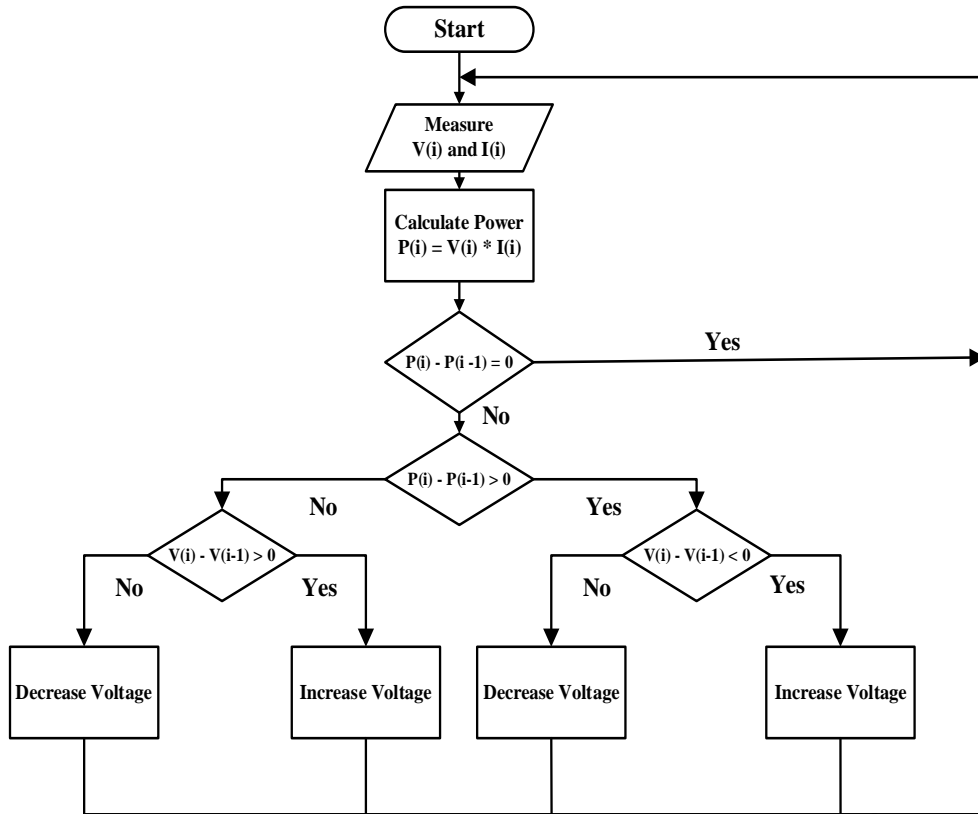
Figure 4.7: The flowchart of the P&O algorithm.
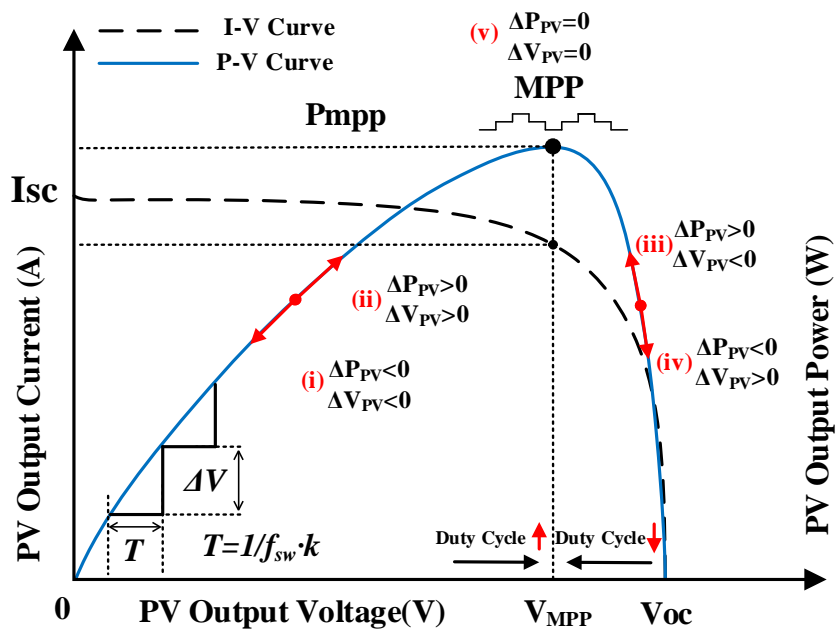
Figure 4.8: Execution of the P&O algorithm on P-V curve.

4.3 Emulated PV Panel and State-space Average Modeling of the Boost Converter.

4.3.1 Emulated PV Panel

Variations in irradiance and ambient temperature affect the current generated by the PV module, which is reflected in the output current and voltage waveforms. Since the controlling of these parameters are infeasible for repeatable testing conditions such as MPPT algorithms, inverter control for different operating conditions, testing of charge controller, performance analysis of and comparison of modelled PV panels with the emulator, PV emulating systems which mimic the characteristics of solar panels with fast transient response have become indispensable part of PV applications. Regarding the advantages of emulators which are fundamentally offering faster and more efficient solar energy generation systems testing, an emulated PV panel is constructed by connecting a SUNTECH PV panel (STP175S-24/Ac) whose parameters are given in Table 4.2. with a DC power supply (ISO-TECH-ISO1603D) that operates in current source mode in parallel. Insignificant amount of current generated by the panel due to the indoor conditions is ignored.

Table 4.2: The emulated PV module (STP175S-24/Ac) parameters.

Parameter	Value
Maximum Power (W)	174.24
Open Circuit Voltage V_{OC} (V)	44.2
Voltage at Maximum Power Point V_{MPP} (V)	35.2
Temperature Coefficient of V_{OC} (%/$deg.C$)	-0.36699
Cells per Module (Ncell)	72
Short-circuit Current I_{SC} (A)	5.2
Current at Maximum Power Point I_{MPP} (A)	4.95
Temperature Coefficient of I_{SC} (%/$deg.C$)	0.042

The DC power supply is used to inject an external current that represents the amount of the irradiance to simulate the current generated by the solar panel. Varying irradiance condition current generation is achieved by manually altering the output current (injected current) of the DC power supply. The equivalent circuit of the

emulated PV panel is shown in Figure 4.9, where I_{cs} represents the external excitation current.
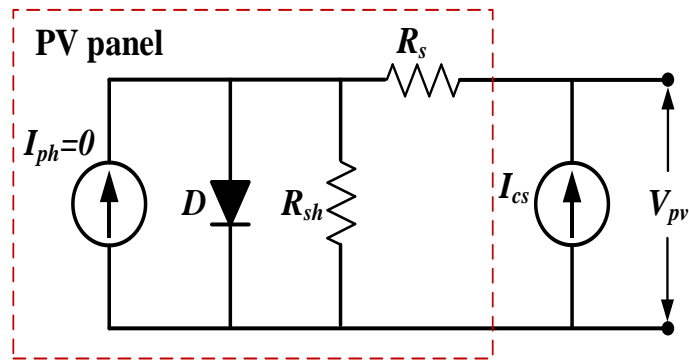
Figure 4.9: The equivalent circuit of the emulated PV panel.

The information needed to construct a solar power array so that it can function as close to its highest peak power point as possible is provided by photovoltaic current-voltage (I-V) and power-voltage (P-V) characteristics curves. The peak power point is defined as the greatest amount of power produced by a PV module when exposed to solar radiation of 1000 watts per square metre. Figure 4.10 shows the characteristics I-V and P-V curves of the emulated PV panel STP175S-24/Ac for varying irradiance values used in the simulations which are 1 kW/m^2, 0.5 kW/m^2 and 0.25 kW/m^2.
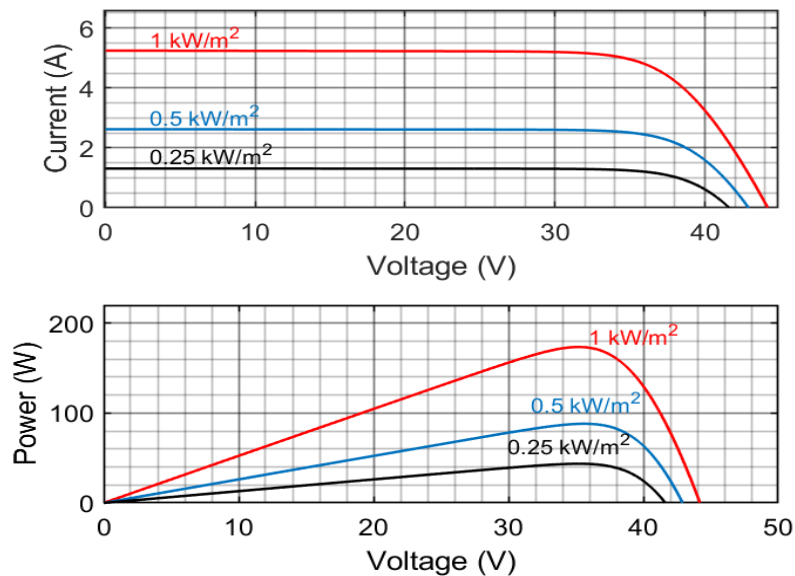
Figure 4.10: Characteristics curves of the emulated PV module (STP175S-24/Ac).

4.3.2 Transfer Function Derivation of the Designed Boost Converter

A control system manages the behaviour of plants for the regulations to meet the requirements using control loops. A plant consists of process and actuator, and it can be represented with a set of mathematical equations (mathematical model). Commonly used mathematical models in the control systems are differential equation model, transfer function model and state-space model. Main purpose of using one of these mathematical models is to simplify control system design and analysis in both time and frequency domains. The classical control theory introduces closed-loop control (feedback) to overcome limitations associates with the use of open-loop control. Primary advantages of the closed-loop controllers over open-loop controllers are disturbance rejection, better performance with parameters' uncertainties of the model, capability in the stabilization of unstable processes, sensitivity reduction to variations of model parameters and enhancement of reference tracking.

In this chapter, transfer function model of the intended boost converter is used to design and analyse the proposed PR-P controller to improve important dynamic properties of the plant such as stability, speed of response, steady-state error, oscillations which constitute the transient and the steady-state response of the system. Intended boost converter transfer function is derived by using dynamic (AC small signal) state-space averaging technique. This process includes taking the Laplace Transform (with zero initial condition) of both the state and output equations in the state-space model of the boost converter [29].

In the experimental set-up, the emulated solar panel is connected to a step-up DC-DC converter (boost converter) and supplies power to the electronic load. The boost converter consists of an inductor, power switch MOSFET, power diode and output capacitor, as shown in the Figure 4.11. The required PV terminal voltage which refers to the maximum power point voltage is achieved by regulating the duty cycle of the PWM signal with the proposed control method.
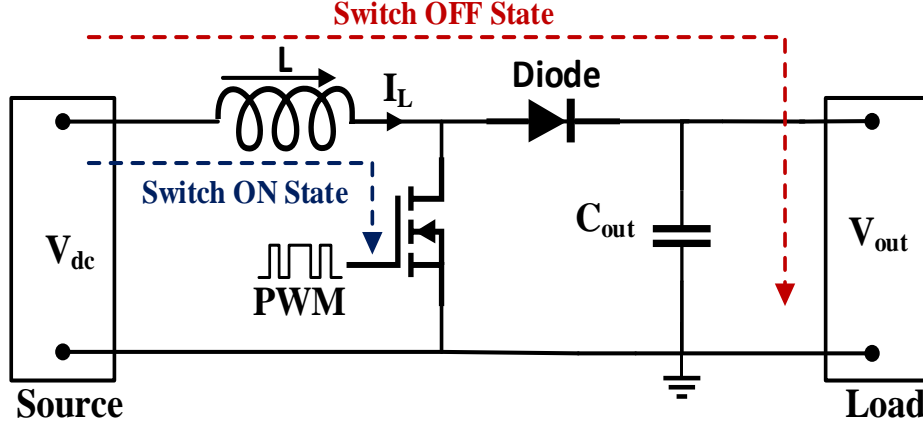
Figure 4.11: Circuit diagram of a boost converter.

Design parameters of the boost converter used for in this work given in Table 4.3.

Table 4.3: Design parameters of the boost converter.

Parameter	Value
Input voltage(V_{dc})	44.2 V
Switching frequency (f_{sw})	20 kHz
Inductance (L)	100 μH
Output capacitance (C_{out})	440 μF
Constant voltage load (V_{out})	70 V

Implementation of state-space averaging method and the design parameters for the boost converter in terms of duty ratio to output voltage yields the transfer function in the s-domain as given by:

$$G_{boost}(s) = \frac{V_{out}(s)}{d(s)} = \frac{\left[\frac{-V_{dc}}{RC_{out}(D-1)^2}\right]s + \frac{V_{dc}}{C_{out}L}}{s^2 + \left(\frac{1}{RC_{out}}\right)s + \frac{(D-1)^2}{C_{out}L}} \tag{4.6}$$

$$G_{boost}(s) = \frac{-4.42 \times 10^{-3}s + 34.53}{3.13 \times 10^{-8}s^2 + 3.91 \times 10^{-5}s + 0.31} \tag{4.7}$$

Input-output voltage relationship of steady-state operation point when the small signal perturbations are zero is given by:

$$\frac{V_{out}}{V_{dc}} = \frac{1}{1-D} \Longrightarrow \frac{70}{44.2} = 1.584, D = 0.37 \tag{4.8}$$

The transfer function of the boost converter in terms of duty ratio to input voltage can be derived by substituting (4.8) into (4.6) as:

$$G_{boost}(s) = \frac{V_{dc}(s)}{d(s)} = \frac{1}{(1-D)} \frac{\left[\frac{-V_{dc}}{RC_{out}(D-1)^2}\right]s + \frac{V_{dc}}{C_{out}L}}{s^2 + \left(\frac{1}{RC_{out}}\right)s + \frac{(D-1)^2}{C_{out}L}} \qquad (4.9)$$

$$G_{boost}(s) = \frac{-7.1 \times 10^{-3}s + 55.25}{3.13 \times 10^{-8}s^2 + 3.91 \times 10^{-5}s + 0.31} \qquad (4.10)$$

4.4 Comparative Analysis of the PR-P and PI Controllers

Control systems are often designed to improve the system characteristics such as stability, speed of response, steady-state error, or prevent oscillations after obtaining an appropriate model of the system. Mathematical model of a system is used in the analysing of the system to predict its respond in both the time and frequency domains. Time domain analysis of a system represents how the state of a dynamic system changes in time while being subjected to a particular input. In other respects, frequency domain analysis of a system comprises of magnitude and phase differences between sinusoidal input and steady-state output of the system as a function of frequency.

Performance assessment of the proposed PR-P control structure is done by using comparative analysis evaluation method which refers to the comparison of two or more control strategies. In this context, the proposed PR-P control structure is compared with PI control structure which is one of the widely used controllers in practice considering step response characteristics (rise time, settling time, settling minimum and maximum values, overshoot, undershoot, peak value and peak time) and time delays existing in two variations (signal distorting delay and non-distorting transport delay). Both controllers are designed by considering the SMPS stability criteria given in Table 4.4.

Table 4.4: Switch mode power supply stability criteria.

Parameters	Value
Crossover (cutoff frequency)	Between the range of $1/10^{th}$ to $1/8^{th}$ of switching frequency
Phase Margin	Greater than 45 degree
Gain Margin	Greater than 10 dB
The slope of the gain curve at the crossover frequency	$\approx$-20 db/decade

The closed-loop step response comparison plot of the derived transfer function of the boost converter controlled with the proposed PR-P controller and PI controller is given in Figure 4.12.
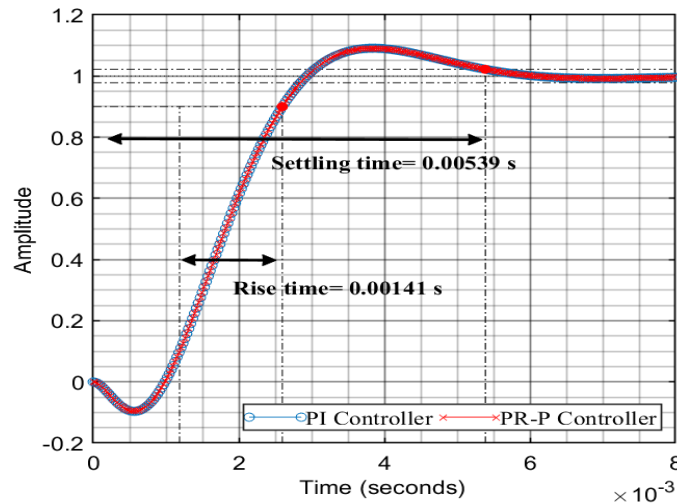
Figure 4.12: Closed-loop step response of the controllers.

Determining how the system responds to a sudden change of the input is very critical. Fast and large deviations from the long-term steady state might have drastic consequences for the specific component itself and other parts of the overall system that rely on it. When the control inputs are unit step functions, the step response of a system in a given initial state is the time evolution of its outputs. Step response provides information about a system's stability as well as its capacity to transition from one stationary state to another. Step response characteristics of the boost converter in terms of open-loop and closed-loop is given in Table 4.5. Time domain analysis of the system regarding transient and steady-state characteristics indicates that similar performance outcomes are achieved with the proposed PR-P controller for a step change.

Table 4.5: Time domain analysis of the boost converter control.

Step Reponse Characteristics	Open-loop	Closed-loop PI Control	Closed-loop PR-P Control
Rise Time (s)	6.4×10^{-4}	0.0014	0.0014
Settling Time (s)	0.0014	0.0054	0.0054
Settling Minimum	102.54	0.9084	0.9093
Settling Maximum	115.64	1.0909	1.0906
Overshoot (%)	2.20	9.0851	9.0638
Undershoot (%)	45.36	9.6256	9.6287
Peak	115.65	1.0909	1.0906
Peak Time (s)	0.002	0.0039	0.0039

Generally, the desired situation in control system applications is to have fast rising, and quickly settled step responses with a low overshoot and undershoot. The time behaviour of the boost converter outputs when its inputs quickly move from zero to one given in Table 4.5 indicates that there is a trade-off between step response characteristics. It is obvious that decreasing response times (rise, peak and settling times) led to a bigger overshoot. The best results have been obtained using the closed-loop PI and PR-P controls by changing the pole and zero locations of unity feedback transfer function.

SMPS output signals display repetitive sinusoidal-like behaviours inherently due to its nature therefore time delays must be considered during the process of building a controller for a dynamical system to analyse its performance. Time delays exist in two variations named signal distorting and non-distorting transport delays. Signal distorting delay stands for phase lag in which each frequency is delayed by a different amount of time and non-distorting delay in which the entire signal is postponed by the same amount of time. The main components cause time delays in a feedback system are sensors, actuators, controller, and the process itself.

Step-response of the feedback loop combined with a sinusoidal interference whose amplitude is 0.2 and frequency is 10 kHz in the presence of internal delay is given in Figure 4.13.
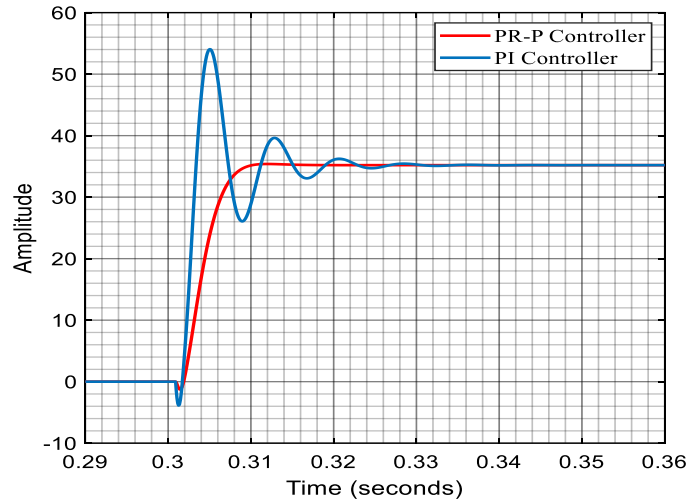
Figure 4.13: Closed-loop step response with internal time delay.

Step-response of the feedback loop combined with the same sinusoidal interference in the presence of both internal delay which is unintentional accruing due to the process itself and feedback signal transport delay is given in Figure 4.14.
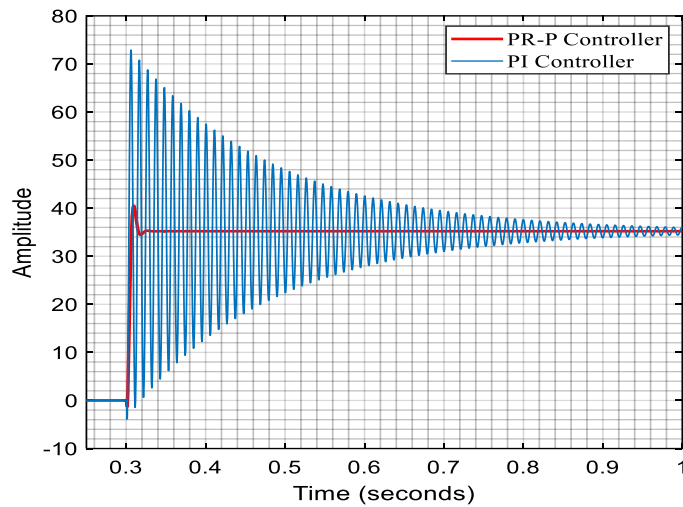
Figure 4.14: Closed-loop step response with internal and signal transport time delays.

A properly designed controller that is perfectly tuned to the model may still be under the risk of reduced performance on the real system. Straightforward approach to overcome this problem is to add margin (time delay) into the design. Regarding this issue, a consistent system must be designed in such a way to ensure that the stability is exceeded in a certain amount instead of just meeting the desired performance so any deviations on the system dynamics will not affect the requirements. In this sense, the

69

proposed PR-P controller has achieved superior enhanced performance in comparison to PI controller as shown in Figure 4.14.

The output voltage of all DC/DC converters is a function of the duty ratio. To prevent control loop instabilities and ensure proper operation of the boost converter requires considering about the duty cycle limitations in practical applications. The estimated duty ratio (D) for the boost converter can be calculated as:

$$D = 1 - \frac{V_{in}\eta}{V_{out}} \tag{4.11}$$

where V_{in}, V_{out} and η are input voltage to regulator, output voltage of the regulator and the regulator efficiency (accounts for losses), respectively. The regulator efficiency η depends on the properties of the boost converter components such as parasitic resistance in the inductor and MOSFET, the voltage drop of the diode set an upper limit on the duty ratio and therefore the output voltage. The general representation of practical boost converters' boost ratio and duty cycle relationship is given in Figure 4.15 [30], [31].
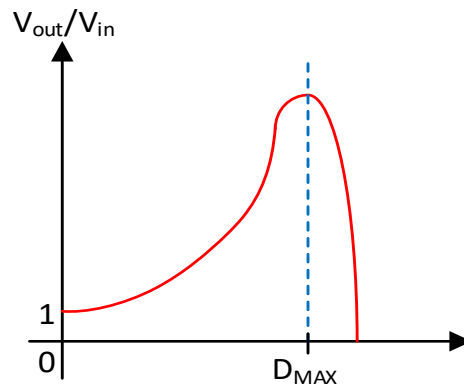
Figure 4.15: Boost ratio and duty cycle relationship

The approximate maximum duty ratio for both synchronous and non-synchronous boost converters is calculated by considering given load current I_{out}, input voltage V_{in} and component resistances as:

$$D_{MAX} \cong \frac{V_{in} - I_{out}(R_1 + R_2 + 2R_L)}{V_{in} + I_{out}(R_1 - R_2)} \tag{4.12}$$

where R_1, R_2 and R_L are resistance of MOSFET switch, resistance of synchronous MOSFET (if applicable) and resistance of inductor, respectively. In this chapter, for the purpose of simplicity the minimum (D_{min}), nominal (D_{nom}) and maximum (D_{max}) duty cycle values are calculated as:

$$D_{min} = \frac{V_{out} + V_D - V_{in(\text{max})}}{V_{out} + V_D}$$

$$D_{nom} = \frac{V_{out} + V_D - V_{in(\text{nom})}}{V_{out} + V_D} \tag{4.13}$$

$$D_{max} = \frac{V_{out} + V_D - V_{in(\text{min})}}{V_{out} + V_D}$$

where the constant output voltage (V_{out}) is 70 V, the maximum input voltage ($V_{in(\text{max})}$) is 44.2 V, which is the open circuit voltage of the emulated PV panel SUNTECH (STP175S-24/Ac), the nominal input voltage ($V_{in(\text{nom})}$) is 35.2 V, which is the maximum power point voltage of the emulated PV panel at 1000 W/m^2 and 25 ºC, the minimum input voltage ($V_{in(\text{min})}$) is 10 V, and the forward voltage (V_D) of the output diode is 0.5 V. According to these parameters calculated duty cycle corresponds with the 10-90% range in which many controllers operate properly.

In addition to the duty cycle, another primary component of the PWM control of the SMPS is the switching frequency. The PWM signal generation is a method to for creating digital pulses to control analog circuits and the simplest way to generate a PWM signal is the intersective method which requires only a sawtooth or triangular waveform. The control input or duty cycle generated from the controller is used to track the reference input. In this application, the PI and the proposed control scheme outputs are compared with a sawtooth waveform to track the desired V$_{mpp}$. The frequency of the sawtooth is 20 kHz which is the switching frequency of the boost converter. The PWM signals for both the PI and the proposed control scheme are given in Figure 4.16. While the proposed control scheme PWM generation remains constants, the conventional P&O MPPT with PI controller PWM generation presents non-constant switching frequency [32]. The advantage of fixed switching frequency in SMPS applications is that any switching noise arising can be predicted, thus facilitates the filtering process. Alternatively stated, the constant switching frequency makes the design of passive filters simpler. Furthermore, it gains more control over

physical size of components, electrical characteristics, frequency response and power losses of the boost converter.
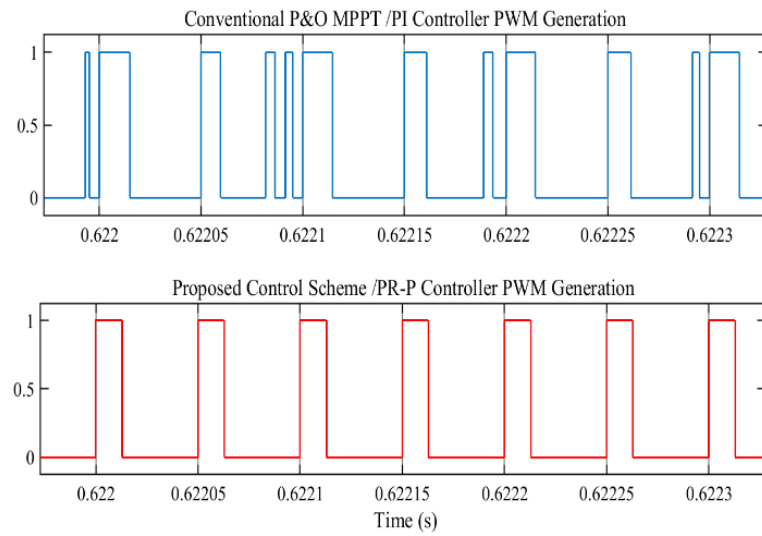
Figure 4.16: Partial section views of PWM signals for the conventional PI and the proposed PR-P control methods in steady state.

Figure 4.16 shows that conventional P&O MPPT algorithm with PI controller PWM generation signal has the period of 27.891 µs and 35.854 kHz in a steady-state partial section, although frequency of the sawtooth modulation signal is 20 kHz. However, the proposed control scheme with PR-P controller PWM generation signal has the same fixed frequency as the modulating signal.

A fixed perturbation size P&O MPPT with a PI controller and the proposed unity proportional gain resonant and gain scheduled proportional (PR-P) controller-based variable perturbation size real-time adaptive P&O MPPT simulation results are generated in MATLAB/Simulink. The fixed perturbation step size is set at ΔV=0.5 with a frequency of 200 Hz corresponding to perturbation period of ΔT=5 ms and irradiance variations are applied with sudden step changes of 1000 W/m^2, 250 W/m^2 (severe shading condition) and 500 W/m^2.

Figure 4.17 shows the voltage waveforms under determined varying irradiance. The proposed control strategy shows enhanced tracking performance 5 times faster than conventional method. Additionally, the steady-state oscillations around MPP are reduced significantly with the proposed control scheme.
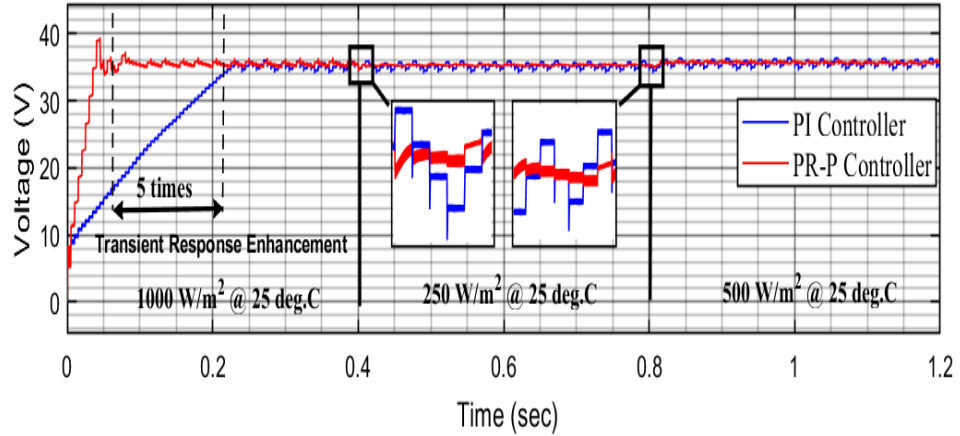
Figure 4.17: Comparison of PV maximum power point voltage tracking performance of the conventional and proposed control method.

Figure 4.18 shows the current waveforms generated under defined conditions which are sudden step changes of irradiance values of 1000 W/m², 500 W/m² and 250W/m² (refers to severe shading condition). The current outputs verified the improved MPPT performance regarding the tracking speed and reduced oscillations.
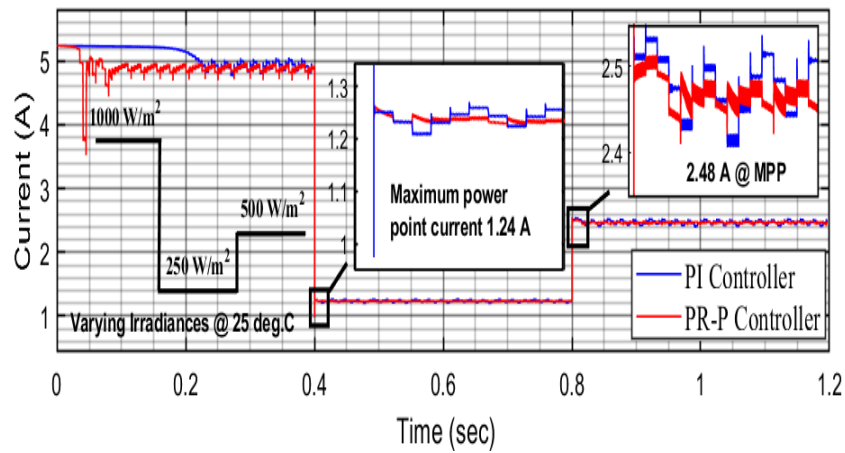
Figure 4.18: Comparison of PV current of the conventional and proposed control methods.

Figure 4.19 shows PV output powers for the PI controlled fixed perturbation P&O MPPT algorithm and the proposed control scheme with the PR-P controller. Approximately 5 times enhancement in the tracking speed and less oscillation in steady state are observed clearly with the proposed control method.

73
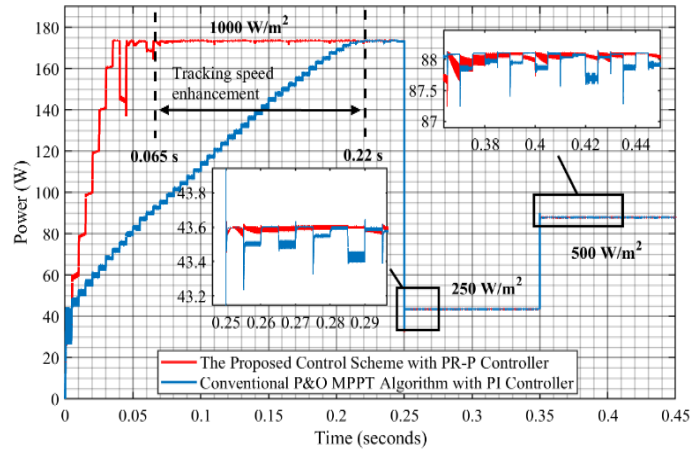
Figure 4.19: PV output powers of the conventional and proposed control methods.

The emulated PV panel SUNTECH (STP175S-24/Ac) Datasheet Values in terms of maximum power point voltages and maximum powers generated under different irradiance values of 1000 W/m², 750 W/m², 500 W/m² and 250 W/m² are given in Table 4.6.

Table 4.6: The emulated PV panel datasheet values.

| Irradiance (W/m²) | SUNTECH (STP175S-24/Ac) Datasheet Values | |
	Maximum Power Point Voltage (V_{mpp})	Maximum Power (W)
1000	35.2	174.2
750	35.55	131.5
500	35.57	88.1
250	35.43	43.59

Table 4.7 shows the efficiency and tracking performance comparison of conventional fixed perturbation size P&O MPPT with a PI controller and the proposed control scheme with PR-P controller under varying irradiance values considering the emulated PV panel SUNTECH (STP175S-24/Ac) Datasheet Values.

Table 4.7: Efficiency and tracking performance comparison of conventional P&O MPPT with a PI controller and the proposed PR-P control scheme.

| Irradiance (W/m²) | Conventional P&O MPPT with PI Controller | | | | The Proposed Control Scheme with PR-P Controller | | | |
	Measured Voltage (V)	Measured Power (W)	Efficiency (η%)	Tracking Speed (s)	Measured Voltage (V)	Measured Power (W)	Efficiency (η%)	Tracking Speed (s)
1000	35.44	169.5	97.3	0.22	35.4	170.05	97.6	0.07
750	36.07	127.2	96.73	0.25	35.79	128.3	97.56	0.05
500	35.76	86.01	97.62	0.26	35.68	87.01	98.76	0.06
250	35.35	41.5	95.2	0.27	35.39	42.5	97.49	0.075

4.5 Experimental Results and Discussions

The block diagram of the experimental setup configuration for testing the proposed MPPT algorithm is given in Figure 4.20. The overall system consists of the emulated PV panel, the DC-DC boost converter, electronic load for constant DC voltage output, dSPACE real-time Interface (RTI) hardware-in-the-loop (HIL) control panels (RTI 1007 processor board, DS2004 A/D and CP4002 Digital I/O boards).

The proposed MPPT method developed by using MATLAB/Simulink was implemented via dSPACE rapid control prototyping. The RTI block of the Modular Hardware/DS2004 High-speed A/D was used to convert the measured terminal current Ipv and terminal voltage Vpv as shown in Figure 4.20.
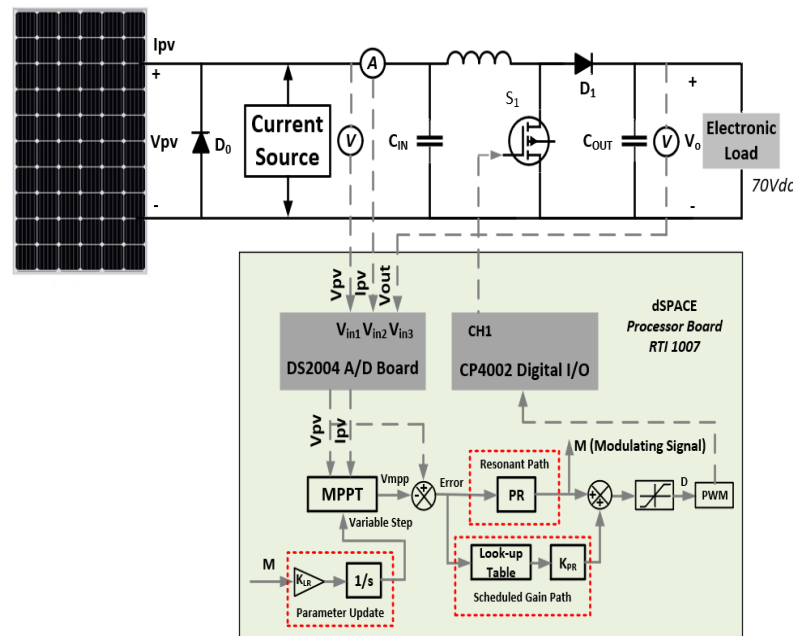
Figure 4.20: Experimental setup configuration for testing the proposed MPPT algorithm.

Test bench of the experiment is given in Figure 4.21. The emulated 175 W commercial SUNTECH PV panel (STP175S-24/Ac) connected with a 360 W DC power supply (ISO-TECH-ISO1603D) in parallel to create real environment PV characteristics was built as a power supply to the electronic load through the DC-DC boost converter. The terminal voltage of the emulated PV panel is controlled by the boost converter.
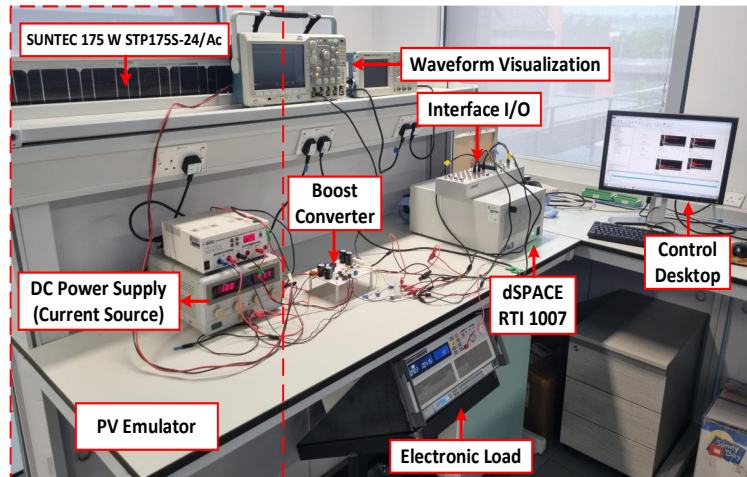
Figure 4.21: Test bench of the overall system.

The converted Ipv and Vpv were then implemented in the MPPT algorithm. Due to the limitation in the range of -10 V to +10 V of dSPACE Analogue to Digital (A/D) channel, the measured terminal outputs were scaled down. Vpv and Ipv were scaled down by a constant factor of 28 and 2.6, respectively. Regulated duty cycle in the simulink to achieve required terminal voltage was used to generate the PWM signal for running the boost converter. For this purpose, generated digital PWM signal was implemented using dSPACE MATLAB/Simulink PC-based simulation platform Modular Hardware/DS4002 Timing and Digital I/O Board.

Conventional fixed perturbation step size PI controlled P&O MPPT algorithm experimental test result is given in Figure 4.22.
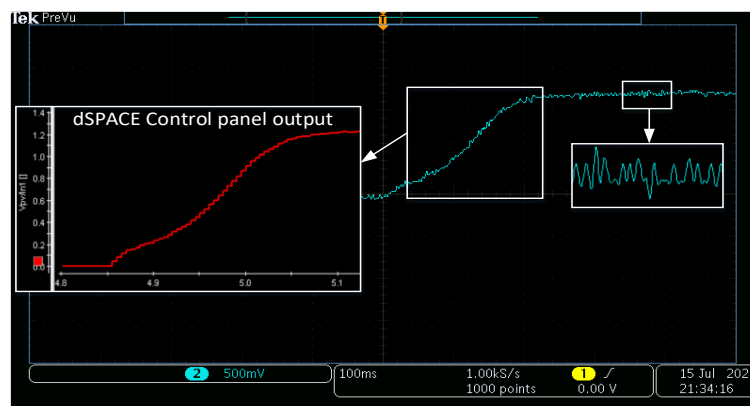
Figure 4.22: PI controlled conventional fixed perturbation step size P&O MPPT algorithm PV voltage.

The proposed unity proportional gain and gain scheduled proportional (PR-P) controller based variable perturbation size real-time adaptive P&O MPPT algorithm experimental test result is given in Figure 4.23.
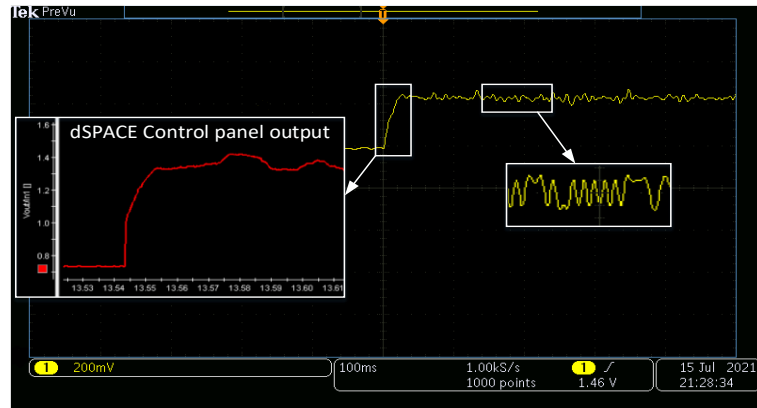
Figure 4.23: PR-P controller based variable perturbation size real-time adaptive P&O MPPT algorithm PV voltage.

The measured values in Figure 4.22 and 4.23. represent both transient and steady-state responses in terms of terminal voltage of the boost converter for constant current of 1 Amp which stands for approximately 200 w/m^2 irradiance since the maximum power point current of the emulated PV panel is 4.95 A at 1000 W/m^2 and 25 ºC.

Conventional fixed perturbation step size PI controlled P&O MPPT algorithm experimental test result for varying irradiance values is given in Figure 4.24.
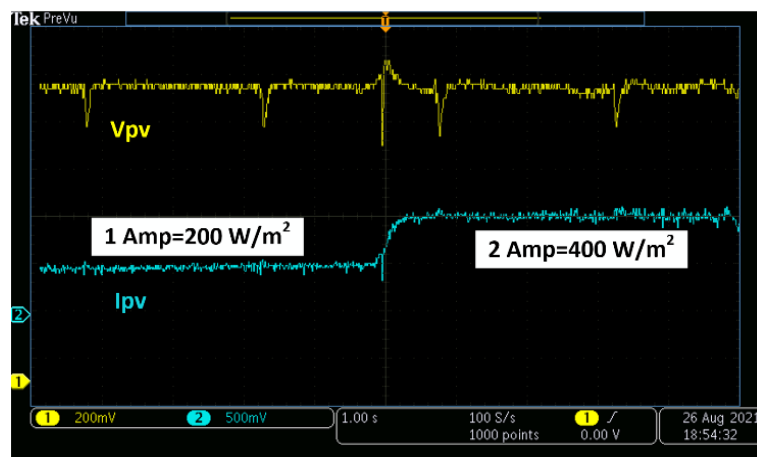
Figure 4.24: PI controlled conventional fixed perturbation step size P&O MPPT algorithm PV voltage for varying irradiance values.

The proposed unity proportional gain and gain scheduled proportional (PR-P) controller based variable perturbation size real-time adaptive P&O MPPT algorithm experimental test result for varying irradiance values is given in Figure 4.25.
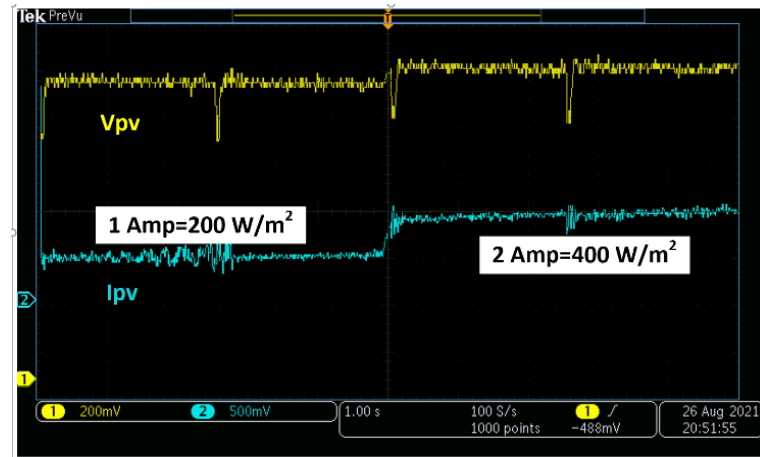
Figure 4.25: PR-P controller based variable perturbation size real-time adaptive P&O MPPT algorithm PV voltage for varying irradiance values.

Experimental results are in accordance with the simulation outcomes and both experimental results and analysis reveal that the proposed control strategy enhanced the tracking speed with reduced steady-state oscillations around maximum power point (MPP).

PV voltage and current waveform comparisons of the conventional and proposed control methods are provided in Figures 4.17 and 4.18, respectively. In both cases, the simulation results indicate that the proposed control method showed a faster tracking with a less oscillation around voltage and current steady state values.

The experimental results of P&O MPPT algorithm PV voltages are given in Figures 4.22 and 4.23. Figure 4.22 shows the PI controlled conventional fixed perturbation step size P&O MPPT algorithm PV output voltage. Figure 4.23 shows the PR-P controller based variable perturbation size P&O MPPT algorithm PV output voltage. The ideal environment provided in the simulations resulted in a greater level of rate of tracking. However, the tracking speed achieved, and the oscillation rate seen in experiments follow the trend established in the simulations. Five times faster transient response and 2% increase in the energy harvesting have been achieved with the use of the proposed control scheme.

4.6 Summary

This chapter has presented Proportional Gain Resonant and Gain Scheduled Proportional (PR-P) Controller based variable perturbation size real-time adaptive perturb and observe (P&O) maximum power point tracking (MPPT) algorithm to overcome the limitations associated with conventional fixed step size PI controlled P&O MPPT algorithm. Moreover, an alternative unprecedented design process based on changing notch filter dynamics with placement of the complementary poles around the boost converter switching frequency for the PR-P controller is implemented.

The proposed control scheme resolved the drawbacks of conventional P&O MPPT method associated with the use of constant perturbation size that leads to poor transient response and high continuous steady-state oscillations.

The prime objective of using the PR-P controller is to utilize inherited properties of the signal produced by the controller's resonant path and integrate it to update best estimated perturbation (ESC model-free adaptive control technique) to use in P&O algorithm that characterizes the overall system learning-based real time adaptive (RTA). Additionally, utilization of internal dynamics of the PR-P controller overcome the challenges namely, complexity, computational burden, implantation cost and slow tracking performance in association with commonly used soft computing intelligent systems and adaptive control strategies. Although the most common use of proportional-resonant (PR) controllers is in DC/AC applications, the results demonstrated that properties of the PR controllers can be utilized effectively in DC/DC systems.

The proposed control scheme is verified using MATLAB/Simulink by applying comparative analysis with PI controlled conventional P&O MPPT algorithm. Moreover, performance of the proposed control scheme is validated experimentally with the implementation of MATLAB/Simulink/Stateflow on dSPACE Real-time-interface (RTI) 1007 processor board, DS2004 A/D and CP4002 Digital I/O boards. The experimental results and analysis reveal that the proposed control strategy enhanced the tracking speed five times with reduced steady-state oscillations around maximum power point (MPP) and more than 99% energy extracting efficiency.

Chapter 5

Fast Converging PR-P Controller Designed by Using Symmetrical Pole Placement Method for Current Control of Interleaved Buck Converter Based PV Emulator

5.1 Introduction

Many research studies conducted on sustainable energy have shown that solar power with its almost zero detrimental effect on the environment uncontrovertibly is one of the prominent renewable energy sources [1]-[9]. In addition to its slightest impact on the environment, solar power is the most abundant and inexhaustible source of energy [10],[11]. Photovoltaic (PV) panels for solar energy generation have wide range of applications from residential districts to large-scale solar power plants [12]. Another primary advantage of PV system is that extensive maintenance is not required after installation process [13],[14].

PV systems basically consist of PV arrays and power electronic converters [15]. These converters constitute the most essential components of the PV systems due to their use of capturing the maximum power generation from PV arrays and subsequently feeding the generated power into the grid [16]. In this regard, development of high-efficiency power electronic converters, high-performance maximum power point tracking (MPPT) algorithms is imperative [17],[18]. Implemented MPPT algorithms and power electronics converters have to ensure the maximum possible power generation despite the variation of temperature, irradiance and non-linear behaviours of solar cells since

a solar cell is basically a p-n junction diode which forms a photoelectric behaviour, whose electrical characteristics vary when exposed to light [19],[20].

Testing the performance of the MPPT algorithms and the power electronic converters with real installed solar panels is a considerable challenge because of the constraints such as need for wide surrounding space, high installation cost and the lack of control over the environmental conditions [4],[21]. Under such constraints, the use of Photovoltaic Emulators (PVEs) is the most cost-effective solution to test MPPT algorithms and power electronics converters [8],[16]. The use of cost-effective emulators provides a clear incentive for global enterprise and scientific development [22]. For the ideal PVE, there are specific requirements which include a proper emulation of non-linear I-V and P-V characteristics of a PV panel, which function under varying atmospheric conditions (temperature and irradiance) [17]. The emulator must be able to integrate Power Electronics Converter interfaces for testing [21]. It must also be able to function appropriately under frequent load changes [19]. Contemporary scientific enquiry has found that emulated I-V and P-V curves produce similar results to real PV panel outcomes (in terms of the datasheet) [23]. However, advantages and disadvantages have been identified in terms of performance criteria, such as implementation costs; efficiency; accuracy; the level of complexity; sensitivity to variable environmental conditions and frequent load changes [4],[15],[24].

In this chapter, interleaved buck converter based PVE current control is presented. Compared to single-phase buck regulator based PVE, interleaved buck converter based PVE offer several advantages such as reduction in both input and output capacitance, improvement in thermal performance and efficiency, enhancement in overshoot and undershoot during load transients [25],[26]. While interleaved buck converter based PVE provide many benefits, implementing of additional phases pose challenges, for instance, phase management, complexity, increase in the cost of components and printed-circuit board (PCB) area [27]. The phase management is the most significant major challenge in multi-phase converter applications [28]. Achieving the highest potential performance is required to balance current evenly between active phases to avoid thermal stress in each phase and ensure optimal ripple cancellation [29],[30]. Moreover, addition and removing of each phase quickly during transients matters a great deal for minimizing excursions on the output voltage. Considering all these reasons, yielding optimum efficiency from the multi-phase buck converter based PVE

leads to the necessity to develop more sophisticated control strategies. The comparative analysis of the most common developed control techniques for multi-phase converter applications in terms of their features, advantages, and limitations is given in Table 5.1.

Table 5.1: Characteristics of commonly used control techniques for multi-phase converter applications.

Control Technique	Features	Advantages	Limitations	References
Proportional-Integral (PI)	•Suitable for linear control •Low-complexity	•Simple implementation •Fast transient response •Easy integration with various control techniques	•Incapable of responding to external distubance (e.g., load variations) •High settling time, steady-state error, overshoots	[33],[34], [35],[36], [37]
Sliding Mode Control (SMC)	•Robust and suitable for non-linear control •Converge towards sliding surface	•Simple Implementation •Capable of responding to external disturbance •Fast dynamics (e.g., settling time) •Robust	•Chattering issues due to discontinuous control law •Excessive overshoots	[34],[37], [38],[39], [40],[41]
Model Predictive Control (MPC)	•Easy for online iteration •Robust and suitable for non-linear control •Enable to predict furure states	•Enhanced transient performance with external constraints •Fast response •Efficient tracking with estimation-based techniques	•Sensitive to circuit parameters •High computational burden •Required for detailed knowledge of the model	[33],[37], [42],[43], [44]
State-space Modeling (SSM)	•Robust and suitable for non-linear control •Suitable for multiple-input and multiple-output systems •Enable to estimate plant states continuously	•Improved transient response •Less overshoot during load varying conditions	•Longer period of time required for initial implementation •Detailed knowledge of the model required	[37],[45], [46],[47], [48]
Fuzzy Logic Control (FLC)	•Robust and suitable for non-linear control •Providing stability in the presence of large variations •Suitable for the systems with imprecise boundary conditons	•Less overshoots •Efficient tracking response •Do not require the mathematical model of the plant	•High computational burden •Required for properly defined rules for operation •Longer settling time	[37],[49], [50],[51], [52]

The chapter proposes a novel and unprecedented Proportional-Resonant-Proportional (PR-P) controller designed by symmetrical poles placement method together with use of robust control theory for the current control of interleaved buck converter-based PVE.

The proposed controller shows superior performance in terms of fast-converging transient response, zero steady-state error, significant reduction in current ripple and properly functioning with parameters uncertainty (highly robust) that constitutes primary concern in multi-phase converters' load sharing. For the purpose of verification and validation of the designed controller, a comparative analysis with a PI

controller is also presented to illustrate the efficiency of the proposed control scheme. In addition to improved dynamics of the control process, unconventional design process of the controller reduces the computational complexity, provides cost-effectiveness and simple implementation. Moreover, implementing of auxiliary Resistor-Capacitor (RC) circuits parallel with the inductors to sense the current in each phase removes the need for current measurement sensors that contribute to overall cost of the system.

5.2 The Proposed PR-P Controller Design

The proposed PR-P controller consists of two parts, one part is Proportional-Resonant (PR) which constitutes resonant path of the controller with a constant proportional unity gain, the other part is proportional gain (P) which is used to determine the compatibility of the controller with parameters of the plant in question to accomplish optimum efficiency [31]. Figure 5.1 shows circuit diagram of PR-P current control of interleaved buck converter (two buck converters connected in parallel) based PVE. Control scheme of the overall system consists of two PR-P controllers for current control in each phase and one PI controller to ensure the current balance (equal load sharing) between phases, mathematical model of the emulated PV panel for the generation of the reference current under varying temperature and irradiance values. Determining the phase currents is done by utilizing the parasitic DC resistances of the inductors by integration of auxiliary Resistor-Capacitor (RC) circuits parallel to the inductors in each phase.

The PR component of the controller is designed by considering the changing dynamics of a notch filter with addition of mutually complementary poles to the notch transfer function whose resonant frequency is PWM switching frequency of the buck converter.

An unrealizable transfer function $G(s)$ that is lightly damped ($\xi = 0.0001$) pair of zeros centred at the PWM switching frequency of the buck converter ($\omega_n = 10\ kHz$) that corresponds to the resonant frequency of the PR and the parameter k (k=2) have been implemented for the application. The selection of the small damping parameter is related to the unprecedented design of the proposed PR-P controller. The smaller

the value, the bigger the gain achieved at the PWM switching frequency. The value of the parameter k establishes enough width for the notch and, consequently, provides a sufficient gain in the case of variation around resonant frequency (the PWM switching frequency of the buck converter).
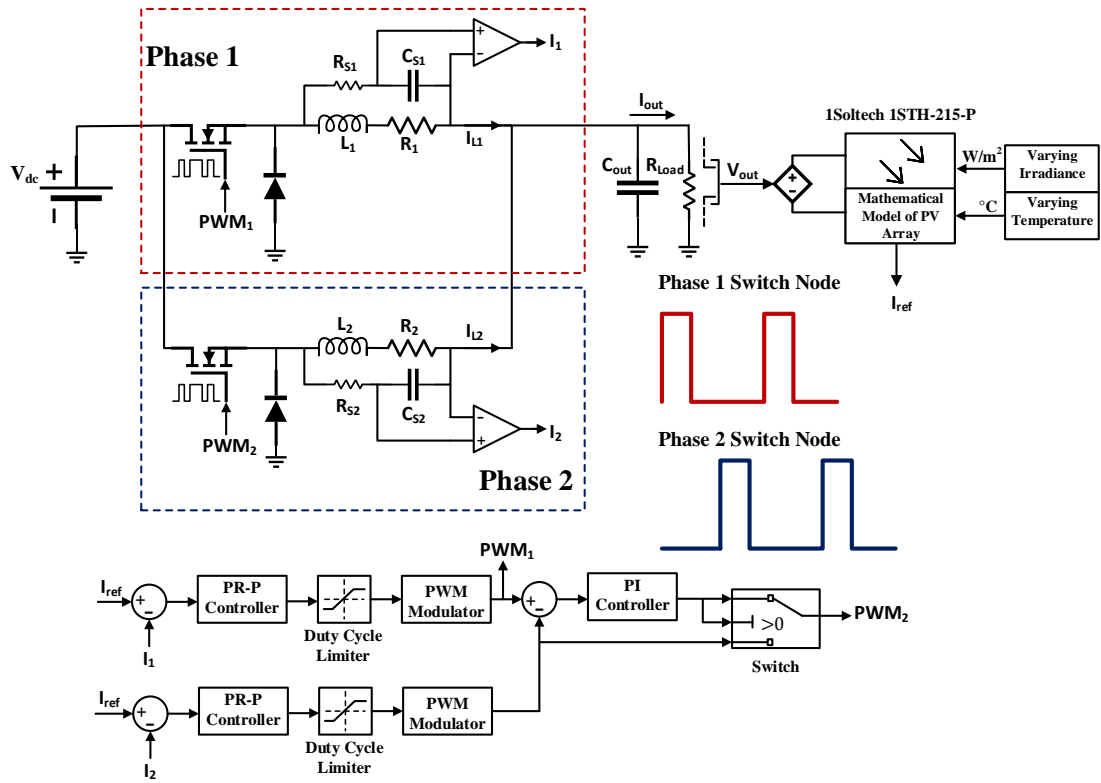
Figure 5.1: PR-P current control of interleaved buck converter.

Figure 5.2(a) shows the frequency response of the physically unrealizable transfer function $G(s)$. There is a gain rising at 40 dB/decade since there are two unanswered zeros, thus the high frequency signals are to pass through altered. Figure 5.2(b) shows that addition of a pole with a cut-off frequency that is k times larger than the natural frequency dragged the high frequency magnitude down by 20 dB/decade. Figure 5.2(c) shows that addition of a complementary pole with a cut-off frequency that is k times smaller than the natural frequency bended down the high frequency magnitude by 20 dB/decade to the zero dB.
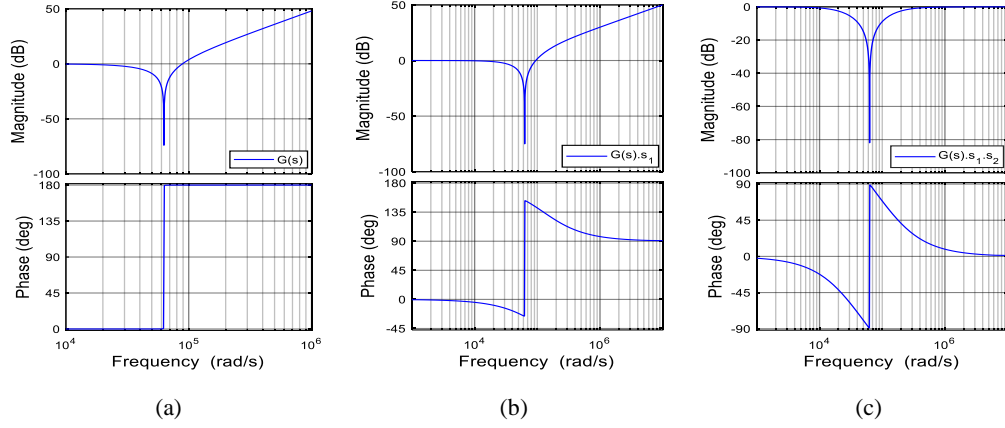
Figure 5.2: The notch filter dynamics-based PR controller: (a) Lightly damped unrealizable transfer function. (b) Addition of the first pole. (c) Addition of the second complementary pole.

The transfer function of PR path of the proposed PR-P controller $G_{PR}(s)$ is the reciprocal of the notch filter transfer function $G_{notch}(s)$ is presented as:

$$G_{PR}(s) = \frac{1}{G_{notch}(s)} = \frac{1}{G(s).s_1.s_2}$$

$$G_{PR}(s) = \frac{\omega_n{}^2}{s^2 + 2\xi\omega_n s + \omega_n{}^2} \cdot \frac{s + k\omega_n}{k\omega_n} \cdot \frac{s + \dfrac{\omega_n}{k}}{\dfrac{\omega_n}{k}}$$

(5.1)

$$G_{PR}(s) = \frac{3.948 \times 10^9 s^2 + 6.201 \times 10^{14} s + 1.559 \times 10^{19}}{3.948 \times 10^9 s^2 + 4.961 \times 10^{10} s + 1.559 \times 10^{19}}$$

(5.2)

Addition of the proportional gain K_{P2} with the value of 100 to the PR path puts the proposed controller into final form as:

$$G_{PRP}(s) = K_{P2} + G_{PR}(s)$$

$$G_{PRP}(s) = \frac{3.987 \times 10^{11} s^2 + 6.251 \times 10^{14} s + 1.574 \times 10^{21}}{3.948 \times 10^9 s^2 + 4.961 \times 10^{10} s + 1.559 \times 10^{19}}$$

(5.3)

The magnitude and phase responses of the designed PR-P controller is given in Figure 5.3. The highest gain of the designed PR-P controller is 82 dB, and it occurs at the PWM switching frequency of the buck converter ($\omega_n = 10\ kHz$). The phase response shows that the phase shift is zero for low and high frequencies.

85
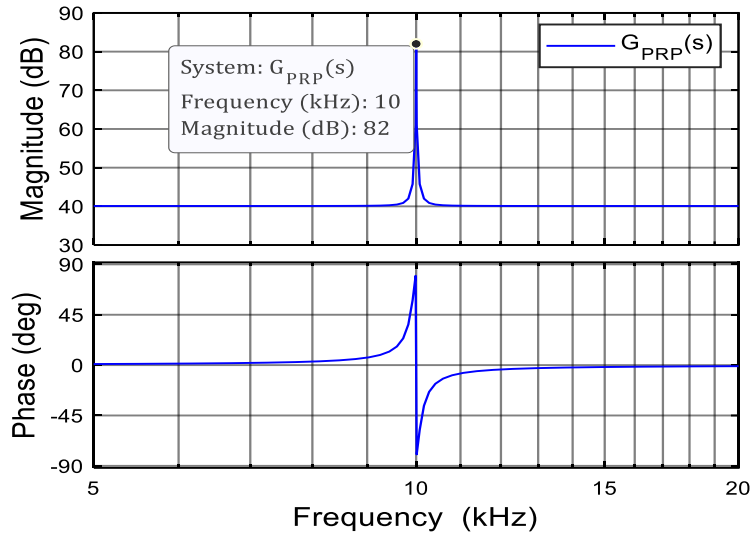
Figure 5.3: Magnitude and phase response of the proposed PR-P controller.

Figure 5.4 shows the unity feedback control structure of the interleaved buck converter PVE with the proposed PR-P controller in s-domain from feedback error (e) to control input (u) to the plant [20],[31].
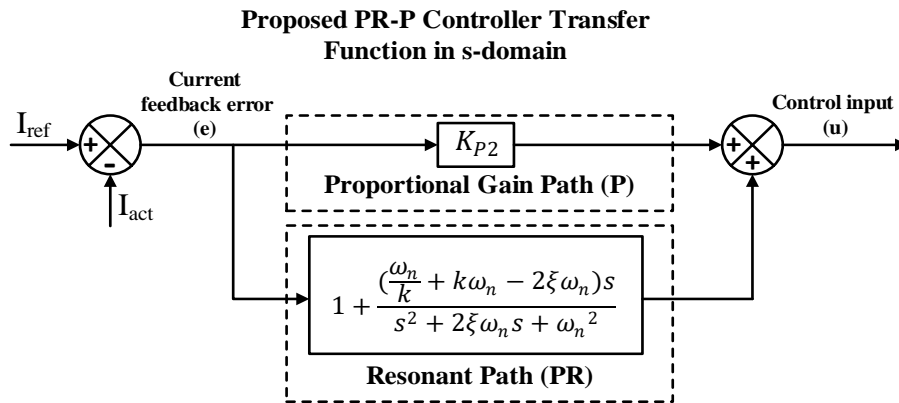
Figure 5.4: Unity feedback of the proposed PR-P controller in s-domain.

The adjustment of a control loop's parameters to the optimum values for the desired control response is known as tuning which requires comprehensive information about the effects of each parameter. Continuous transfer function mode of a controller represents the function of each parameter used in the design of the controller. Figure 5.5 shows the unity feedback control structure of the proposed PR-P controller in continuous transfer function mode from feedback error (e) to control input (u) to the plant [20],[31].
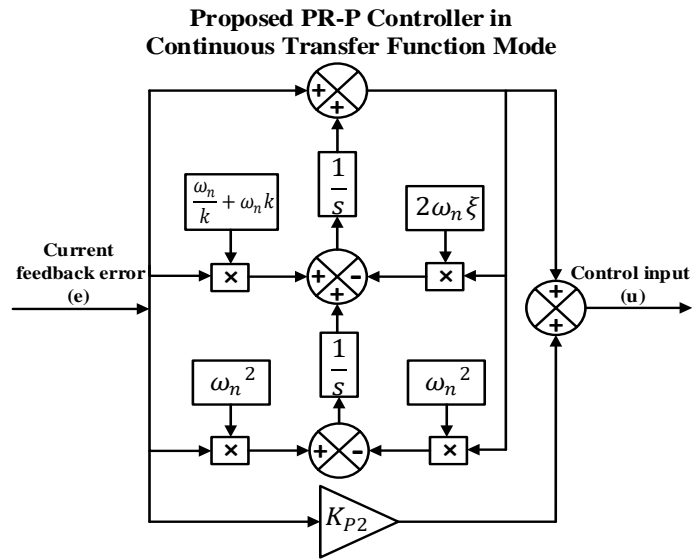
Figure 5.5: Unity feedback of the proposed PR-P controller in continuous transfer function mode.

5.2.1 Current Sensing with Auxiliary RC Circuit

One of the problems in multi-phase converter topologies is the possibility of imbalance between phase currents [25]. If the currents are not in balance, there will not be good cancellation in ripple currents and the amount of power loss in each phase will be different from each other [32]. To assure load balancing, current sensing and feedback is required. An auxiliary RC circuit connected parallel to the inductors in each phase is used for measuring the currents. Accordingly, Figure 5.6 shows the current sensing part of the phase-1 circuit.
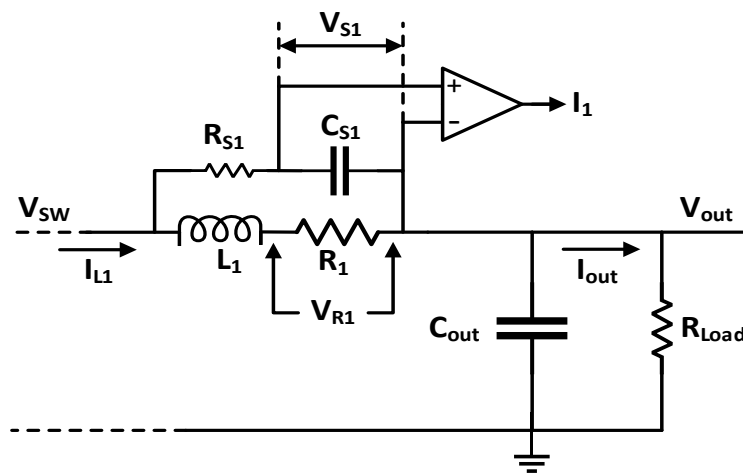
Figure 5.6: Lossless current sensing by using an auxiliary RC circuit in parallel with the inductor.

The idea behind this method is utilizing the parasitic resistance of wires of the inductor. There is a voltage drop on the inner parasitic resistance R_1 of the inductor and current I_{L1} flowing through the inductor is measured based on this voltage drop. There is no access to R_1 so the measurement is carried out outside with the implementation of RC auxiliary circuit. The voltage V_{S1} across the capacitor C_{S1} is proportional to the R_1 and therefore it is also proportional to the I_{L1}. Considering the DC situation, voltage drop of the inductor due to its inductance is zero. DC voltage on the parasitic resistance is the DC current times the resistance and accordingly V_{S1} can be written as:

$$V_{S1(DC)} = I_{L1(DC)}R_1 \tag{5.4}$$

where $V_{S1(DC)}$, $I_{L1(DC)}$ are DC voltage and DC current, respectively. Considering the AC situation (high frequency components-ripple) with the assumption that most of the current flow through the inductor since impedance of the inductor is much lower than the auxiliary RC circuit (very large resistance), voltage drop on the parasitic resistance is proportional to the inductor current. Therefore, V_{S1} can be written as:

$$V_{S1(AC)} = I_{L1(AC)}(R_1 + sL_1)\frac{\frac{1}{sC_{S1}}}{R_{S1} + \frac{1}{sC_{S1}}} \tag{5.5}$$

where $V_{S1(AC)}$, $I_{L1(AC)}$, $(R_1 + sL_1)$ and $(1/sC_{S1})/(R_{S1} + 1/sC_{S1})$ are AC voltage, AC current, Laplace presentation of impedance of the inductor branch and RC circuit as a voltage divider, respectively. Working (5.5) out yields:

$$V_{S1(AC)} = I_{L1(AC)}R_1\left(\frac{1 + \frac{sL_1}{R_1}}{1 + sC_{S1}R_{S1}}\right) \tag{5.6}$$

If the time constant of the inductor (L_1/R_1) and the RC circuit time constant $(C_{S1}R_{S1})$ are made equal, the voltage across the capacitor is AC current times the parasitic resistance and it can be written as:

$$V_{S1(AC)} = I_{L1(AC)}R_1 \tag{5.7}$$

The Equations (5.4) and (5.7) shows that the voltage across the capacitor is representing the current flowing through the inductor in both DC and AC situations.

Given the inductance value $L_1 = 7.8108 \times 10^{-4}\ H$, winding resistance value $R_1 = 0.5\ \Omega$ and arbitrarily selecting a value for $C_{S1} = 1.0414 \times 10^{-5}\ F$, calculation the value of R_{S1} is carried out by setting the time constants of inductor (L_1/R_1) and capacitor $(C_{S1}R_{S1})$ branches equal to each other as follows:

$$R_{S1} = \frac{L_1}{R_1} \times \frac{1}{C_{S1}} = 150\ \Omega \tag{5.8}$$

The waveforms of actual current and sensed current with amplifier gain of 2 for single-phase buck converter is given in Figure 5.7.
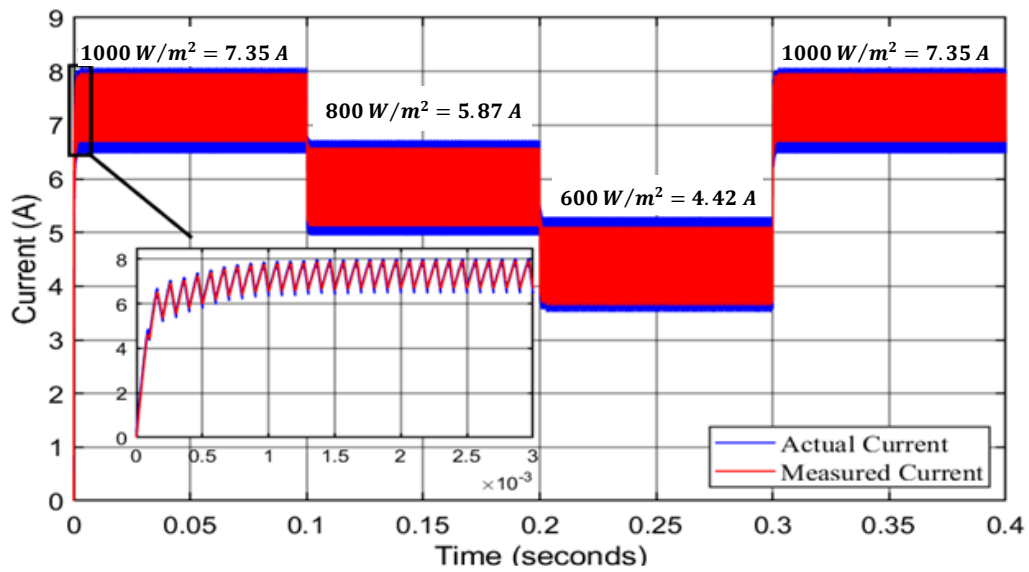
Figure 5.7: RC circuit measured current and actual current

5.3 Emulated PV Panel Parameters and Specifications

Electric characteristics of a PV module are represented graphically by using I-V and P-V characteristics curves. These curves summarize the current-voltage and power-voltage relationships at present conditions of irradiance and temperature of a PV panel. Formation of the curves pertains to PV module's parameters. The emulated PV module is 1Soltech 1STH-215-P with parameter given in Table 5.2.

Table 5.2: The emulated PV module (1Soltech 1STH-215-P) parameters.

Parameter	Value
Maximum Power (W)	231.15
Open Circuit Voltage V_{OC} (V)	36.3
Voltage at Maximum Power Point V_{MPP} (V)	29
Temperature Coefficient of V_{OC} (%/deg.C)	-0.36099
Cells per Module (Ncell)	60
Short-circuit Current I_{SC} (A)	7.84
Current at Maximum Power Point I_{MPP} (A)	7.35
Temperature Coefficient of I_{SC} (%/deg.C)	0.102

Figure 5.8 shows I-V and P-V curves of the emulated PV panel at 25 ºC and specified iradiances of 1000 W/m², 800 W/m² and 600 W/m².
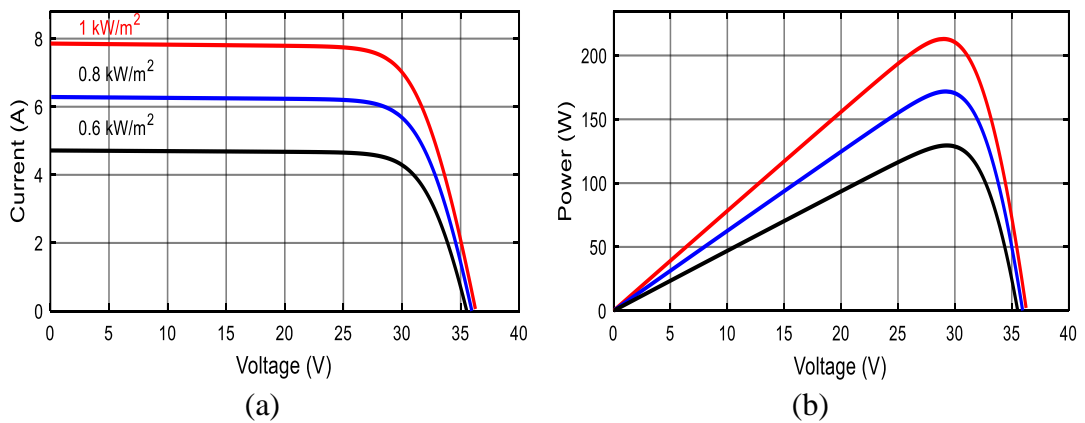
Figure 5.8: Emulated PV panel characteristics curves; (a) I-V curve (b) P-V curve.

The proposed interleaved buck converter based PVE and its control structure block digaram is given in Figure 5.1. It takes an input voltage (V_{dc}) of 48 volts and converts it into an output voltage of 29 volts. The switching frequency is 10 kHz. The minimum load resistance R_{min} is 3.9465 ohm (corresponds to the maximum load condition). In the continuous conduction mode (CCM) operation of the PVE, the maximum ripple allowed in the inductor is 20% of the average inductor current and the maximum load. The maximum ripple in the capacitor is plus and minus 2% of the average output voltage.

5.3.1 Calculation the Values of Buck Converter-based PV Emulator Components

Buck converter is a switch topology that takes a DC input voltage V_{in} and transforms it to the DC output voltage V_{out}. The output voltage is always smaller than the imput voltage ($V_{out} < V_{in}$). In an asynchronous buck converter, the lower switch is implemented by using a diode which will automatically turn on when the upper switch implemented by using a MOSFET or IGBT is turned off. Usually an asynchronous buck converter is designed to operate in CCM in which the operation range is selected in a way that all times the inductor current is positive which ensures that the diode is in forward bias. If this conditon is not met the equations that describe the behavior of the converter changes. The switched topology in CCM has two different states shown in Figure 5.9. When the control signal is high the controllable switch (S) turns on and connects the input voltage to the LC circuit driving the inductor current. This is maintained during a certain amount of time called the on-time t_{on} after which the control signal is changed to a low state which causese the controllable switch to turn off and the current is driven throuhg the diode. This is maintained during a certain amount of time called off-time t_{off}.

(a) The on-state (time interval: 0<t<dT$_s$)

(b) The off-state (time interval: dT$_s$<t<T$_s$)
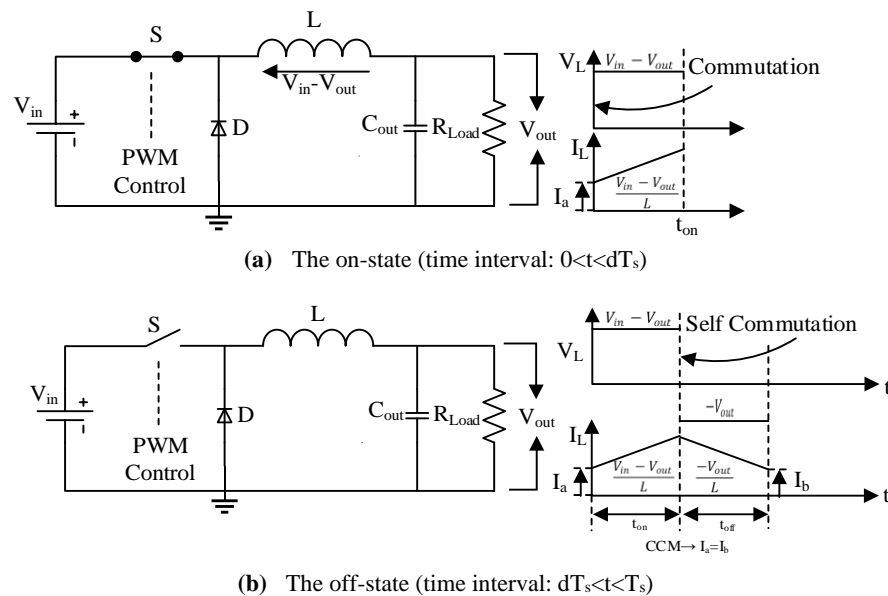
Figure 5.9: Switch topologies and inductor current-voltage waveforms.

The steady state duty cycle of the plant is given by:

$$D = \frac{V_{out}}{V_{in}} \tag{5.9}$$

The maximum average inductor current is given by:

$$I_{L,avg,max} = \frac{V_{out}}{R_{min}} \tag{5.10}$$

The maximum average inductor ripple current is the 20% of the average current that is given by:

$$\Delta I_L = 0.2 I_{L,avg,max} \tag{5.11}$$

Inductance value L of the inductor is given by:

$$L = \frac{V_{in}(1 - D)D}{f_{sw}\Delta I_L} \tag{5.12}$$

Capacitor ΔV_C or output voltage ripple ΔV_{out} is the $\pm 2\%$ of the average output voltage is represented by:

$$\Delta V_C = \Delta V_{out} = 0.04 V_{out} \tag{5.13}$$

Capacitance value C of the capacitor is represented by:

$$C = \frac{V_{in}(1 - D)D}{8L f_{sw}^{2}\Delta V_C} \tag{5.14}$$

The calcuted values of the PVE parameters and components are given in Table 5.3.

Table 5.3: Calculated values of the PVE parameters and components.

Parameters and Components	Value
Steady-state Duty Cycle	0.6042
Maximum Average Inductor Current (A)	7.3483
Maximum Average Inductor Current Ripple (A)	1.4697
Inductor Value (mH)	0.781
Output Voltage Ripple (V)	1.16
Capacitor Value (μF)	15.837

5.3.2 Deriving Transfer Function of the Buck Converter-based PV Emulator

Step-by-step transfer function derivation process of the buck converter with its components which are input voltage V_{in}, inductance L, output capacitance C_{out}, load resistance R_{Load}, inductor current i_L, capacitor current i_C, inductor voltage V_L, capacitor voltage V_C, steady-state duty cycle D and small signal duty cycle d is presented with the following equations based on comprehensive and systematic analysis of the averaging-perturbation-linearization process of the switch mode power supplies (SMPS) explained in Chapter 2. Accordingly, taking Laplace transform of state and output equations with zero initial condition yields:

$$sX(s) = AX(s) + BU(s)$$
$$Y(s) = CX(s) + DU(s)$$

(5.15)

Rewriting the state equation as:

$$sX(s) - AX(s) = BU(s)$$
$$(sI - A)X(s) = BU(s)$$

(5.16)

By premultiplying $(sI - A)^{-1}$ to both sides of (5.16) yields:

$$X(s) = (sI - A)^{-1}BU(s)$$

(5.17)

By substituting (5.17) into the output equation of the plant is resulted as:

$$Y(s) = [C(sI - A)^{-1}B + D]U(s)$$

(5.18)

Transfer function of the system is given by:

$$G(s) = \frac{Y(s)}{U(s)} = C(sI - A)^{-1}B + D$$

(5.19)

AC small signal analysis of the converters consists of obtaining averaged state-space equation of the converters and superimposing ac variation (perturbation) around the steady-state point. To find the steady state operating point of the system, time

derivative is set to zero in the state equation. Dynamic AC small signal model is given by:

$$\hat{x}(s) = (sI - A)^{-1}[(A_1 - A_2)X + (B_1 - B_2)V_{in}]\hat{d}(s)$$

$$\frac{\hat{x}(s)}{\hat{d}(s)} = (sI - A)^{-1}[(A_1 - A_2)X + (B_1 - B_2)V_{in}]$$

(5.20)

The state variables of the system are inductor current (i_L) and capacitor voltage (V_C) since the inductor and capacitor are the only energy storage elements of the buck converter. Accordingly, the state vector x of the buck converter is given by:

$$x = \begin{bmatrix} i_L \\ V_C \end{bmatrix}$$

(5.21)

Analysis of the buck converter in continuous current mode (CCM) and deriving its averaged state-space equation is given in Table 5.4.

Table 5.4: Derivation of average state-space equation of buck converter in CCM.

	On-state (time interval: 0<t<dT$_s$)	Off-state (time interval: dT$_s$<t<T$_s$)	State-space Averaging	
Derivation of state equations	$V_L = L\dfrac{di_L}{dt} = V_{in} - V_{out}$ $\dfrac{di_L}{dt} = \dfrac{V_{in} - V_{out}}{L}$ $i_L = i_{out} + i_C$ $i_L = \dfrac{V_{out}}{R_{Load}} + C_{out}\dfrac{dV_C}{dt}$ $\dfrac{dV_C}{dt} = \dfrac{i_L}{C_{out}} - \dfrac{V_{out}}{R_{Load}C_{out}}$	$V_L = L\dfrac{di_L}{dt} = -V_{out}$ $\dfrac{di_L}{dt} = \dfrac{-V_{out}}{L}$ $i_L = i_{out} + i_C$ $i_L = \dfrac{V_{out}}{R_{Load}} + C_{out}\dfrac{dV_C}{dt}$ $\dfrac{dV_C}{dt} = \dfrac{i_L}{C_{out}} - \dfrac{V_{out}}{R_{Load}C_{out}}$	**The averaged system matrix**	$A = \begin{bmatrix} 0 & \dfrac{-1}{L} \\ \dfrac{1}{C_{out}} & \dfrac{-1}{RC_{out}} \end{bmatrix}$
System matrices	$A_1 = \begin{bmatrix} 0 & \dfrac{-1}{L} \\ \dfrac{1}{C_{out}} & \dfrac{-1}{RC_{out}} \end{bmatrix}$	$A_2 = \begin{bmatrix} 0 & \dfrac{-1}{L} \\ \dfrac{1}{C_{out}} & \dfrac{-1}{RC_{out}} \end{bmatrix}$	**The averaged input matrix**	$B = \begin{bmatrix} \dfrac{D}{L} \\ 0 \end{bmatrix}$
Input matrices	$B_1 = \begin{bmatrix} \dfrac{1}{L} \\ 0 \end{bmatrix}$	$B_2 = \begin{bmatrix} 0 \\ 0 \end{bmatrix}$	**Averaged state-space equation** $\dot{x} = Ax + BV_{dc}$	$\begin{bmatrix} \dfrac{di_L}{dt} \\ \dfrac{dV_C}{dt} \end{bmatrix} = \begin{bmatrix} 0 & \dfrac{-1}{L} \\ \dfrac{1}{C_{out}} & \dfrac{-1}{RC_{out}} \end{bmatrix}\begin{bmatrix} i_L \\ V_C \end{bmatrix}$ $+ \begin{bmatrix} \dfrac{D}{L} \\ 0 \end{bmatrix}[V_{in}]$

The state variable vector X at steady-state operation point from can be rewritten by considering that all parasitic resistances are zero as the following:

$$X = -A^{-1}BV_{in} = -\frac{adj\begin{bmatrix} 0 & \dfrac{-1}{L} \\ \dfrac{1}{C_{out}} & \dfrac{-1}{R_{Load}C_{out}} \end{bmatrix}}{det\begin{bmatrix} 0 & \dfrac{-1}{L} \\ \dfrac{1}{C_{out}} & \dfrac{-1}{R_{Load}C_{out}} \end{bmatrix}}\begin{bmatrix} \dfrac{D}{L} \\ 0 \end{bmatrix}V_{in} \qquad (5.22)$$

$$X = \begin{bmatrix} \dfrac{C_{out}{}^2 DV_{in}}{R_{Load}} \\ DV_{in} \end{bmatrix}$$

Substituting (5.22) and the averaged system and input matrices derived in Table 5.4 into (5.20) results in:

$$\frac{\hat{x}(s)}{\hat{d}(s)} = \frac{\begin{bmatrix} \hat{\imath}_L \\ \hat{V}_C \end{bmatrix}}{\hat{d}(s)} = \begin{bmatrix} \dfrac{V_{in}(C_{out}R_{Load}s + 1)}{C_{out}LR_{Load}s^2 + Ls + R_{Load}} \\ \dfrac{V_{in}R_{Load}}{C_{out}LR_{Load}s^2 + Ls + R_{Load}} \end{bmatrix} \qquad (5.23)$$

Duty ratio to the inductor current transfer function is obtained from (5.23) by substitution of the calculated components values for one phase of the intended buck converter as:

$$\frac{i_L(s)}{d(s)} = \frac{V_{in}}{L}.\frac{s + \dfrac{1}{R_{Load}C_{out}}}{s^2 + \dfrac{s}{R_{Load}C_{out}} + \dfrac{1}{LC_{out}}} \qquad (5.24)$$

$$\frac{i_L(s)}{d(s)} = (6.1455 \times 10^4).\frac{s + 1.6 \times 10^4}{s^2 + 1600s + 8.0841 \times 10^7}$$

5.4 Proportional-Integral (PI) PWM Error Compensator Design

The Proportional-Integral (PI) feedback compensator structure is used in wide range of applications in control systems. The main properties make extensive use of PI controller are its simplicity in imlemetation, easy comprehension of its impacts on systems and high efficiency. A PI contoller is designed as a PWM error compensator to provide current balance between phases of the interleaved buck converter. Morever, robustness of the system that is adversly affected with parameter uncertainity is

increased with the use of PI controller. The unity feedback structure of the single phase proposed PVE system is given in Figure 5.10.
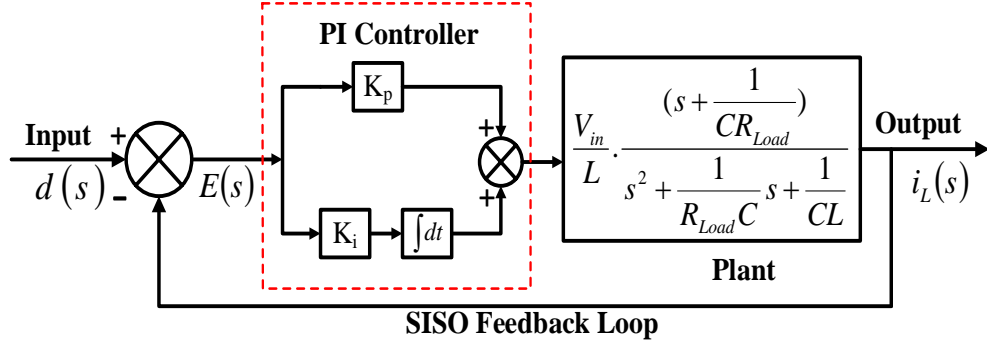
Figure 5.10: Unity feedback control structure of the PVE.

The closed-loop transfer function of inductor current to the duty ratio for the unity-feedback system with PI control is given by:

$$G_{CL}(s) = \frac{V_{in}K_p}{L} \frac{s^2 + s\left(\frac{1}{CR_{Load}} + \frac{K_i}{K_p}\right) + \frac{K_i}{K_pCR_{Load}}}{s^3 + s^2\left(\frac{1}{CR_{Load}} + \frac{K_pV_{in}}{L}\right) + s\left(\frac{1}{CL} + \frac{K_pV_{in}}{CLR_{Load}} + \frac{K_iV_{in}}{L}\right) + K_iV_{in}} \qquad (5.25)$$

K_p and K_i values are calculated as 0.21 and 709, respectively according to stability criteria of the buck converter is given in Table 5.5.

Table 5.5: Buck converter stability criteria in terms of frequency domain.

Parameters	Value
Crossover (cutoff frequency)	Between the range of $1/10^{th}$ to $1/8^{th}$ of switching frequency
Phase Margin	Greater than 45 degree
Gain Margin	Greater than 10 dB
The slope of the gain curve at the crossover frequency	$\approx$-20 db/decade

5.5 Comparative Analysis of the Proposed PR-P Controller

Common goals of control sytems are obtaining fast rise time, minimal overshoot and zero steady-state error. In addition to these objectives, maintaining load sharing in balance, increase the robustness of the system despite parameter unceratinties,

reduction in current and voltage ripples are aimed. Performance assessment of the proposed PR-P control structure is done by using comparative analysis evelution method with widely used PI control structure. Current feedback control structure of the overall system is given in Figure 5.11.
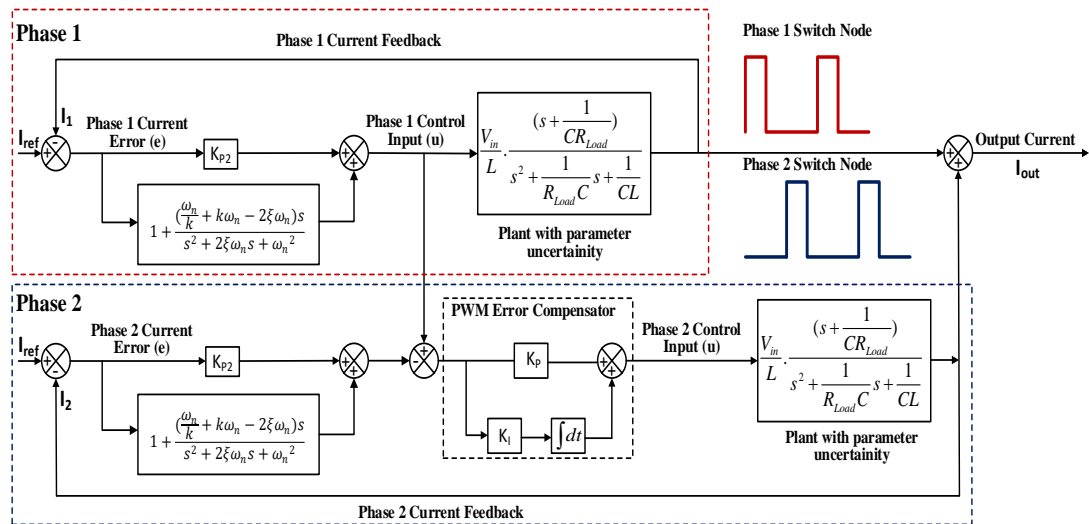
Figure 5.11: Overall system current feedback control structure.

When designing a controller for a system, open-loop response is considered on a preferential basis to determine what needs to be improved for a desired response. Figure 5.12 depicts the open-loop and uncontrolled closed-loop step responses of derived transfer function of the PVE.

(a) (b)
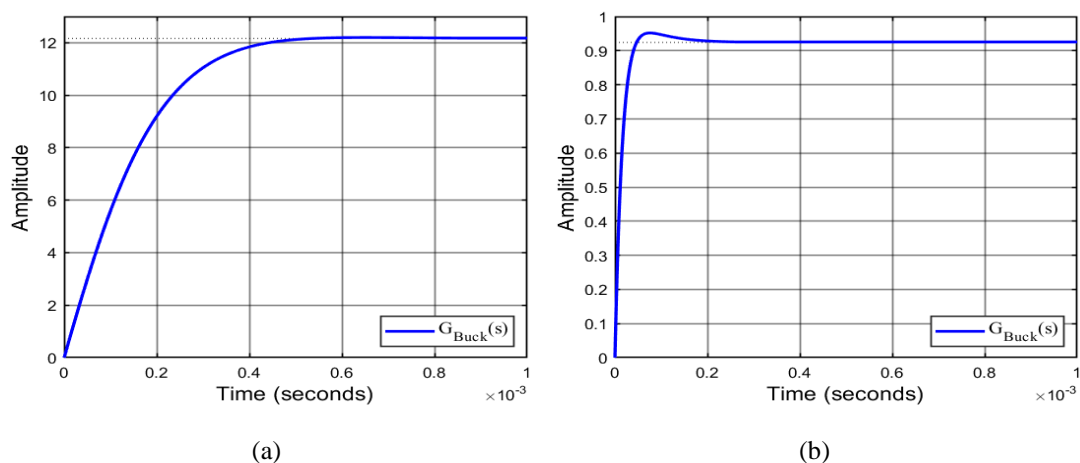
Figure 5.12: PVE step response; (a) Open-loop step response (b) Uncontrolled closed-loop step response.

Figure 5.13 illustrates the closed-loop step response comparison plot of the derived transfer function of the PVE controlled with the proposed PR-P and PI controllers.
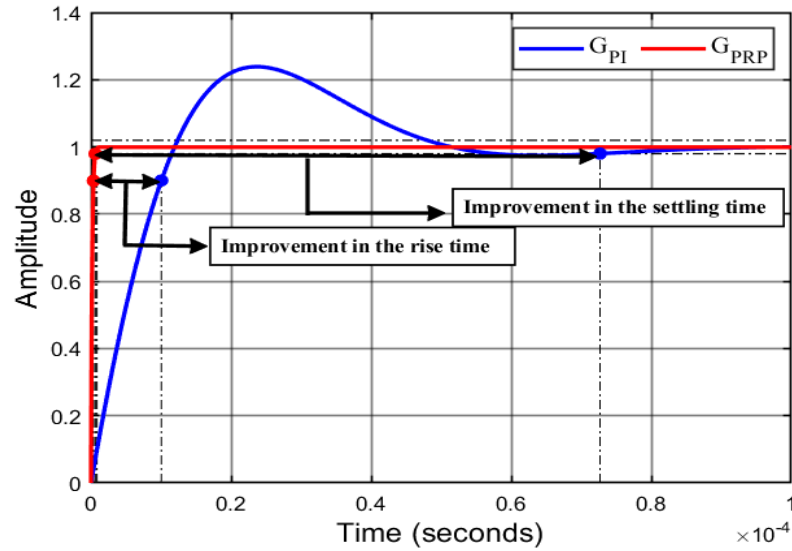
Figure 5.13: The proposed PR-P and PI controlled closed-loop
step response of the PVE.

Step response characteristics of the PVE in terms of open-loop and closed-loop is given in Table 5.6. Time domain analysis of the system regarding transient and steady-state characteristics indicates that enhanced performance outcomes are achieved with the proposed PR-P controller.

Table 5.6: Time domain analysis of the overall system.

Step Reponse Characteristics	Open-loop	Closed-loop Without Controller	Closed-loop PI Control	Closed-loop PR-P Control
Rise Time (s)	2.7203×10^{-4}	2.8250×10^{-4}	9.1876×10^{-6}	3.5257×10^{-7}
Settling Time (s)	4.1803×10^{-4}	1.1501×10^{-4}	$7.2690 \times 10^{-}$	6.2230×10^{-7}
Settling Minimum	10.9681	0.8414	0.9030	0.9002
Settling Maximum	12.2004	0.9518	1.2385	0.9992
Overshoot (%)	0.31	3.0028	23.8460	5.8370×10^{-4}
Undershoot (%)	0	0	0	0
Peak	12.2004	0.9518	1.2385	0.9992
Peak Time (s)	6.5048×10^{-4}	7.5723×10^{-5}	2.3304×10^{-5}	1.1058×10^{-6}

The response of the overall system to the unit step input with all initial conditions equal to zero is given in Table 5.6 by considering open-loop and closed-loop unity feedback structures. The comparison of the obtained results shows the superior performance of

the closed-loop characteristics of the system with the use of the proposed PR-P controller. Although the closed-loop PI control of the system gives better results regarding the response times, it leads to a poor transient performance in terms of overshoot. The underlying cause of a higher overshoot is the inertial term in the transfer function of the buck converter arising from the use of inductor. In mathematical sense, the term containing a damping ratio and a natural frequency in the second order characteristic equation of the buck converter is not changed by the PI controller proportional and integral gains.

A properly designed controller that is perfectly tuned to the model may still be under the risk of reduced performance on the real system. Straightforward approach to overcome this problem is to add margin into the design. Regarding this issue, a consistent system must be designed in such a way to ensure that the stability is exceeded in a certain amount instead of just meeting the desired performance so any deviations on the system dynamics will not affect the requirements. Classical gain and phase margins analysis of a system at some critical frequency or frequencies is made for the purpose of designing a robust control. The amount of margin chosen for a system depends on uncerainty between the model and the real system. Classical gain and phase margin analysis of a system is one of the assessment methods of its robustness but does not give a complete view about the system robustness since the effects of the gain and phase are assessed individually. Therefore, combination of gain and phase uncertainty known as a disk margin analysis needs to be considered. In respect to this, the disk margin analysis has to be performed in addition to individual assessment of the margins with classical approach.

The PVE feedback loop with the proposed PR-P controller and uncertain multiplicative factor F that has the nominal value of 1 is given in Figure 5.14. The system has infite gain margin, 89.98 degree phase margin at the gain crossover frequency of 6.2068×10^6 rad/s, 25µs delay margin. Bandwidth of the system is 7.86×10^3 rad/s.
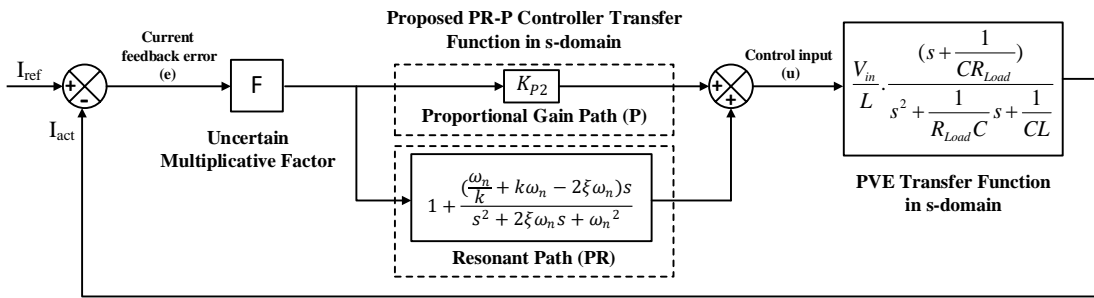
Figure 5.14: The PVE feedback-loop with the proposed PR-P controller and the multiplicative factor F.

Due to the plant uncertainties and other sources of variations, the loop gain and phase are exposed to fluctuations. The general aproaches to determine the amount of uncertainty are either quantifying through experiments or approximation based on gained insight about the system after wide range of simulations. The gain and phase unceratinty analysis in feedback loop will be performed based on to the stability criteria given in Table 5. It is supposed that the open-loop gain variation is 50% (increase or decrease), and the phase variation is ±45°. The set of values F that captures the unceratin gain/phase with relative gain change in [0.0765,1.5] and phase change of ± 45° is given in Figure 5.15.
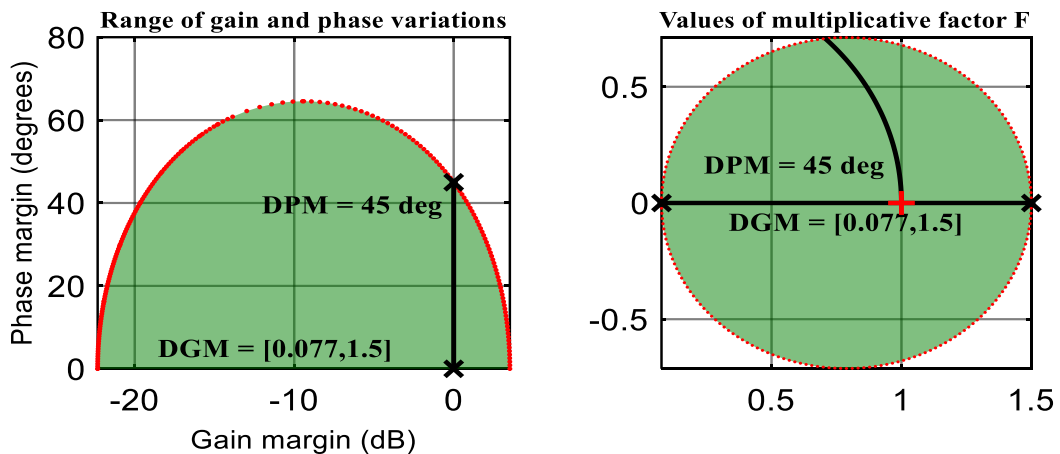
Figure 5.15: Specified range of gain & phase variations and the multiplicative factor F.

Figure 5.15 shows that the gain can vary between 7% and 150% of its nominal value without of phase variation and the phase can vary by ± 45° without gain variation. In the case of variation for both gain and phase, their deviation remains inside the shaded

region in the left. The step response of incorporating of this uncertainty into the closed-loop model is given in Figure 5.16.

(a)   (b)
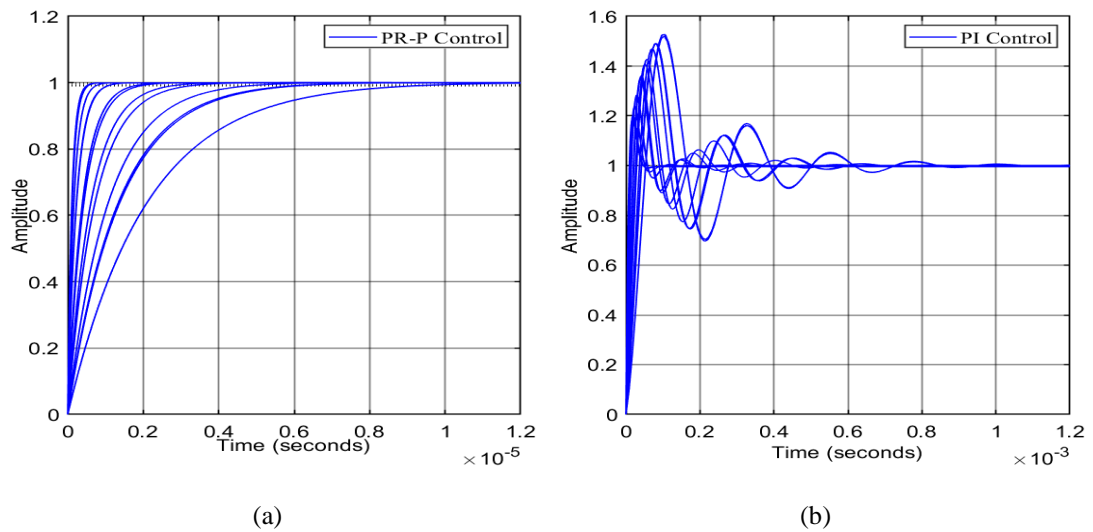
Figure 5.16: Closed-loop step response of the PVE for the set of values of F
(a) with PR-P control (b) with PI control.

The robust stability margin of the system that is full range of simultaneous gain and phase variations tolerable by the closed-loop system is given in Figure 5.17.

(a)

(b)
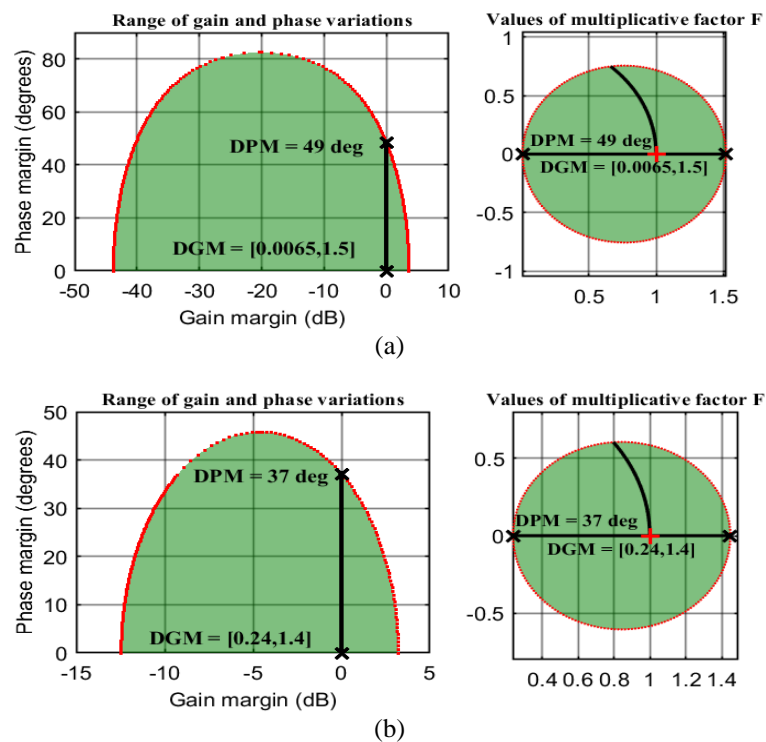
Figure 5.17: The gain & phase variations tolerable (robust stability margin)
by the closed-loop system; (a) PR-P control (b) PI control.

101

The closed-loop step response indicates that the system performs well and yields good robustness to specified gain and phase variations. The robust stability margin of the PR-P controlled system is 100% that means feedback loop can withstand 100% of the specified uncertainty generated by F. Figure 5.17(a) shows that 100% uncertainty specified in F therefore in the openloop system amounts the gain variation between 0.6% and 150% of the nominal value, and phase variation of $\pm 49°$. The robus stability margin of the PI controlled system is 87%, meaning that feedback loop can withstand only 87% of the specified unceratinty. Figure 5.17(b) indicates that 87% uncertainty specified in F therefore in the openloop system amounts the gain variation between 24% and 140% of the nominal value, and phase variation of $\pm 37°$. The proposed PR-P and PI current wafevorm control of single phase PVE for varying irradiance of 1000 W/m^2, 800 W/m^2 and 600 W/m^2 that correspond to 7.3483 A, 5.8656 A and 4.4153 A, respectively and voltage outputs for both control configurations are given in Figure 5.18. The proposed PR-P controller structure for the PVE reveals better performance than PI control in terms of transient response and reduction in the current and voltage ripples. While the system reaches steady state in less than 1 millisecond for PI control, 10 times faster convergence to steady-state is attained with the proposed PR-P controller.
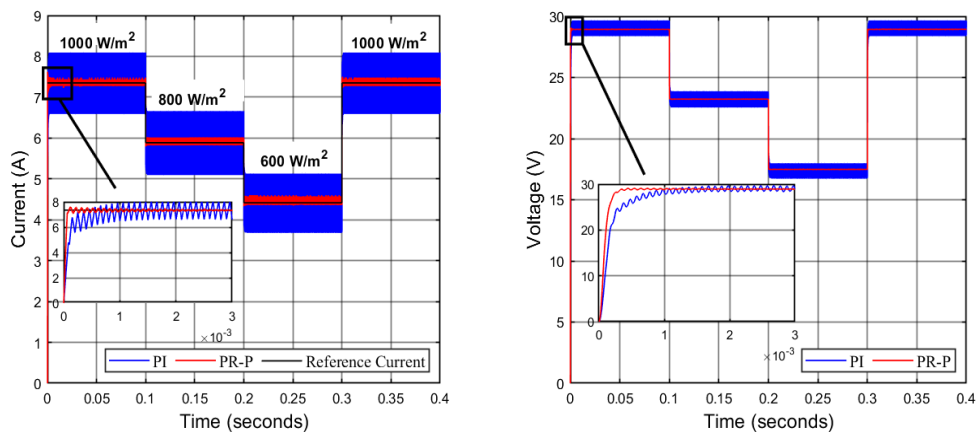
Figure 5.18: Output current and voltage waveforms of the PR-P and PI controlled single phase PVE.

Figure 5.19 shows that phase currents are accurately balanced for varying irradiance conditions for interleaved buck converter based PVE. Furthermore, the output current ripples are reduced compared to single phase buck converter based PVE given in Figure 5.18.
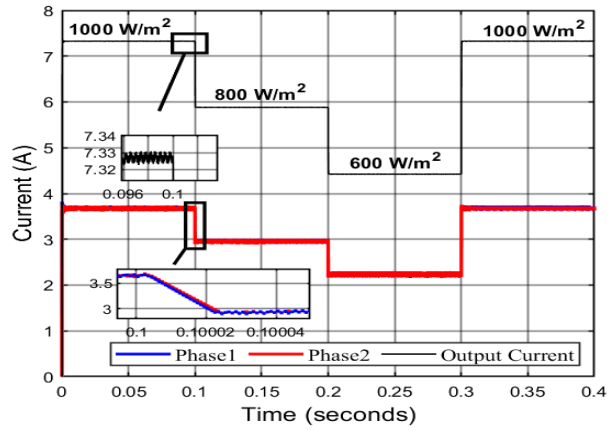
Figure 5.19: Output current waveform of the PR-P controlled interleaved buck converter based PVE.

Figure 5.20 displays the performance of the PVE to variations in the values of the inductance in each phase at different irradiance values. In Figure 5.20(a), the inductance of each phase is halved and additionally 20% inductance difference is applied between phases. In Figure 5.20(b), additional dissimilarity is implemented in terms of DC parasitic resistance of the inductor. The value of parasitic resistance is set to 2 Ω and 2.4 Ω (20% variance) for phases. Parameter uncertainties and variations in component values are inevitable in dynamics systems. The objective PVE system reveals good performance with the proposed PR-P controller under parameter variations.
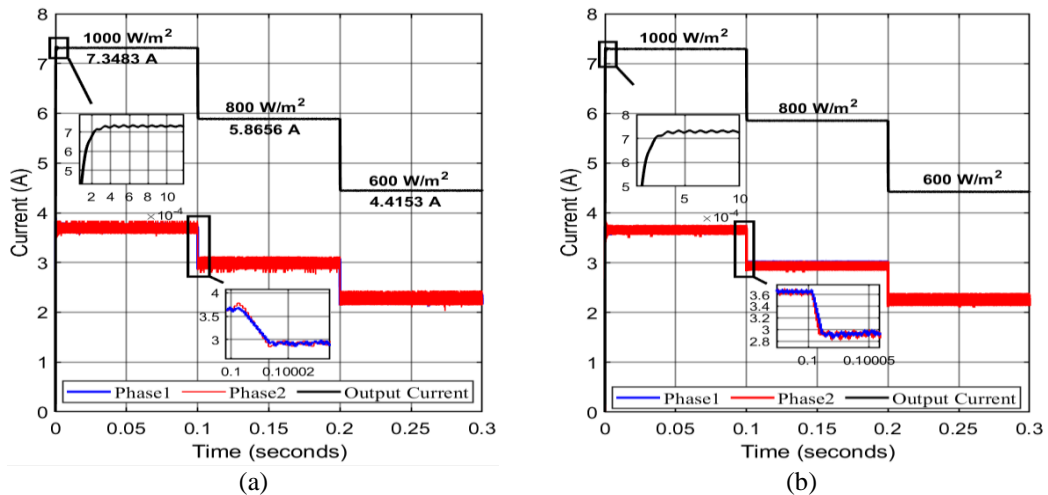
Figure 5.20: Output current waveforms under varitons of inductance and DC parasitic resistance (a) $L_1=(7.8108 \times 10^{-4})\times 50\%$ H, $L_2=(7.8108 \times 10^{-4})\times 40\%$ H; (b) $L_1=(7.8108 \times 10^{-4})\times 50\%$ H, $L_{R1}=2$ Ω, $L_2=(7.8108 \times 10^{-4})\times 40\%$ H, $L_{R2}=2.4$ Ω

Figure 5.21 displays the PVE and the emulated PV module I-V characteristic curves at different irradiance values. The proposed PR-P controller interleaved buck converter based PVE system I-V curves correspond to the parameters of the emulated PV module (1Soltech 1STH-215-P) given in Table 5.2 and I-V curves given in Figure 5.8.
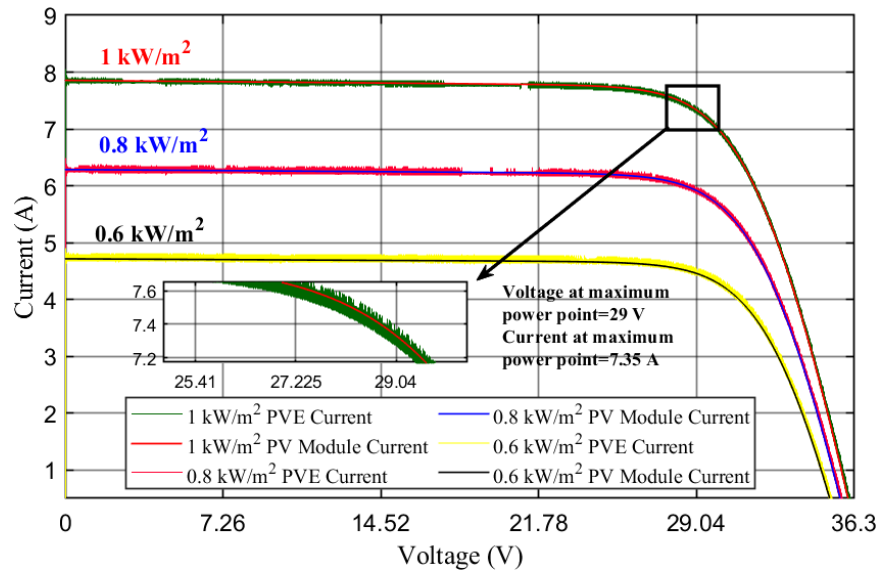
Figure 5.21: I-V characteristics curves at different irradiance values for the proposed PVE and PV module

5.6 Summary

This chapter has presented interleaved buck converter based photovoltaic emulator current control with proportional-resonant-proportional (PR-P) controller. By considering the most commonly used controller mappings for SMPS with their features, advantages and limitations, verification and validation of the designed PR-P controller compared with the PI controller has been presented to illustrate the proposed controller scheme efficiency by using robust control theory. Unlike the classical gain and phase margin analysis of the system through which effects of the gain and phase are worked individually for the assessment of its robustness, combination of gain and phase uncertainty has been considered. In respect to this, disk margin analysis has been performed in addition to straightforward classical approach (individual gain and phase margins assessment) to overcome the main issues in control systems designing such as complex dynamics, uncertainty, intentional simplicity, stochastic events, and process variations. The stability of a closed-loop system against gain or phase

fluctuations in the open-loop response has been measured by disc margins. The implementation has been carried out by adding multiplicative uncertainty factor F with the nominal value of 1 to the buck converter based PVE feedback loop. Since the disc margin is a metric that indicates how much uncertainty the loop can withstand before becoming unstable, 50% (increase or decrease) open-loop gain and ±45° phase variation has been added into the system by setting the values of F. The results have revealed that 13% improvement in the robust stability margin and 12° bigger phase toleration with the PR-P controller have been achieved. Additionally, the proposed controller has shown superior performance in terms of 10 times faster-converging transient response, zero steady-state error, significant reduction in current ripple and properly functioning with parameters uncertainty (highly robust) that constitutes primary concern in multi-phase converters' load sharing. Moreover, unconventional design process of the controller reduces the computational complexity, provides cost-effectiveness and simple implementation. Output voltage and current waveforms produced by the PVE at different irradiance values reflects the I-V characteristics curves of the emulated PV panel accurately.

Chapter 6

Symmetrical Pole Placement Method-based Unity Proportional Gain Resonant and Gain Scheduled Proportional (PR-P) Controller with Harmonic Eliminator for Single Phase Grid-connected PV Inverters

6.1 Introduction

Photovoltaic (PV) energy is a clean, renewable source of direct current (DC) energy generated from the sunlight, which attracts considerable attention due to remarkable advantages such as reliability and long-life, advanced manufacturing process, static and noise-free operations, increasing efficiency, decreasing prices, flexibility of construction and availability of government support and incentives [1]-[4]. The increasing demand of PV energy systems has leaded to comprehensive studies in this field, common ground of these studies aims at achieving the increase in the efficiency, reliability and useful life-span of the PV systems and on the contrary the reduction in cost and space from generation to delivering of the energy [5], [6]. Single-phase PV inverter systems have been widely applied in photovoltaic power generation. Inverter current control with the object of injecting smooth current with less harmonics to the grid is the key aspect of the PV power sourced grid connected inverter (GCI) systems [7]. The main reasons of harmonic generation in single phase PV inverter systems are basically due to distortion in the grid voltage, switching harmonics (high frequency) and DC-link voltage variations arising from the MPPT [8], [9]. The basic model of closed loop Pulse Width Modulation (PWM) current controlled single- phase inverter

with harmonic information is given in Figure 6. 1, where G_{PR}, G_{PWM}, G_{inv} and G_f are PR controller, PWM, inverter and filter transfer functions, respectively.
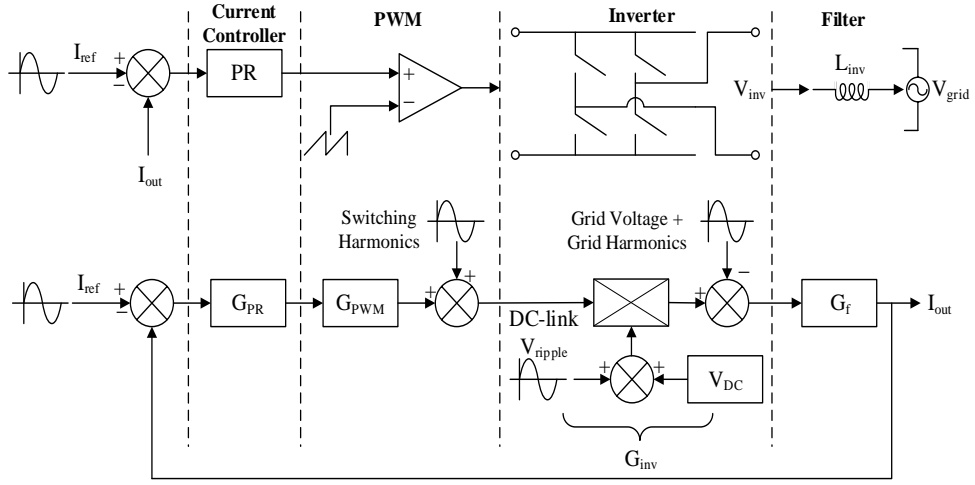
Figure 6.1: The current controlled PWM inverter with harmonic information.

It is crucial to state that distortions in the current for the single-phase GCI systems are particularly caused by the PWM control of the inverter and variations in the DC-link voltage [9]. Considering that the fundamental grid voltage $v_g^1 = \sqrt{2}V_g^1 \cos(\omega_0 t + \varphi)$, the fundamental grid current $i_g^1 = \sqrt{2}I_g^1 \cos(\omega_0 t)$, the inverter output voltage $v_{inv}^1 = \sqrt{2}V_{inv}^1 \cos(\omega_0 t + \varphi - \varphi_1)$, the DC side instantaneous power P_{dc} (i.e., PV array output power) and the instantaneous inverter output power P_{inv} for the single-phase inverter PV system can be obtained as:

$$P_{dc} = v_{pv}i_{pv} - v_{pv}C_{dc}\frac{dv_{pv}}{dt} = v_{pv}i_{pv} - V_{pv}C_{dc}\frac{d\tilde{v}_{pv}}{dt} - \tilde{v}_{pv}C_{dc}\frac{d\tilde{v}_{pv}}{dt} \qquad (6.1)$$

$$\begin{aligned} P_{inv} &= v_{inv}^1 i_g^1 = \sqrt{2}V_{inv}^1 \cos(\omega_0 t + \varphi - \varphi_1)\sqrt{2}I_g^1 \cos(\omega_0 t) \\ &= V_{inv}^1 I_g^1 \cos(\varphi - \varphi_1) + V_{inv}^1 I_g^1 \cos(2\omega_0 t + \varphi - \varphi_1) \\ &\quad + \left(i_g^1 \sum_{h=2}^{n} v_{inv}^h + v_{inv}^1 \sum_{h=2}^{n} i_g^h \right) \end{aligned} \qquad (6.2)$$

where V_g^1, I_g^1, V_{inv}^1, ω_0, φ, φ_1, v_{pv}, i_{pv}, C_{dc}, V_{pv}, $\tilde{v}_{pv}$, i_g^h, v_{inv}^h represents amplitude of the fundamental grid voltage, amplitude of the fundamental grid current, amplitude of the fundamental inverter output voltage, fundamental angular frequency, power angle, inverter voltage leading angle, PV voltage, PV current, DC-link capacitance, DC

component of the PV voltage, AC component of the PV voltage, grid current harmonics and inverter voltage harmonics, respectively.

For a single-phase PV system, neglecting the inverter and DC-link capacitor losses gives $P_{dc} = P_{inv}$. Ignoring the high order term $\tilde{v}_{pv}\, d\tilde{v}_{pv}/dt$ in the DC side instantaneous power and considering the relationships of $|V_{pv}| \gg |\tilde{v}_{pv}|$, $|I_g^1| \gg |i_g^h|$, and $|V_{inv}^1| \gg |v_{inv}^h|$, equivalence of the powers obtained in (6.1) and (6.2) yields:

$$\tilde{v}_{pv} \approx -\int \left[\frac{V_{inv}^1 I_g^1}{C_{dc} V_{pv}} cos(2\omega_0 t + \varphi - \varphi_1)\right] dt \qquad (6.3)$$

which confirms that the PV source output (the DC-link voltage) pulsate at twice the grid frequency and amplitude of its variation is proportional to fundamental amplitude of the inverter output voltage V_{inv}^1 and fundamental amplitude of the grid current I_g^1.

The inverter output voltage harmonics induction is strictly dominated for the injected current in the grid, since DC-to-AC inversion is executed by the application of the PWM scheme using non-linear semiconductor devices. In general terms, the PWM current controlled single-phase inverter output voltage v_{inv} can be expressed as:

$$\begin{aligned} v_{inv} = d_{pwm} v_{pv} &= \left(d_{pwm}^1 + \sum_{h=2}^{n} d_{pwm}^h\right)\left(V_{pv} + \tilde{v}_{pv}\right) \\ &= d_{pwm}^1 V_{pv} + d_{pwm}^1 \tilde{v}_{pv} + V_{pv} \sum_{h=2}^{n} d_{pwm}^h \\ &+ \tilde{v}_{pv} \sum_{h=2}^{n} d_{pwm}^h = v_{inv}^1 + \sum_{h=2}^{n} v_{inv}^h \end{aligned} \qquad (6.4)$$

where d_{pwm}, d_{pwm}^1, and d_{pwm}^h are the PWM signal, fundamental component of the PWM and harmonics of the PWM, respectively. In theory, formation of the PWM harmonics $\sum_{h=2}^{n} d_{pwm}^h$ occurs around the switching frequency and its multiples that corresponds to generation of the high order harmonics [10]. However, practical applications show that the PWM harmonics contributes to low order harmonic distortions due to dead-time and non-linear ON-OFF switching [10], [11]. Equation (6.4) indicates that variation $\tilde{v}_{pv}$ will introduce harmonics in the inverter output voltage and it mainly contains even harmonics at the double of the grid frequency $2\omega_0$ shown in

(6.3). The term $d_{pwm}^1 \tilde{v}_{pv}$ in (6.4) implies that odd current harmonics injection is inevitable in single-phase PV inverter systems with the frequency of $(2k + 1)\omega_0, k = 1,2,3, ...$ [9]. The second order harmonic on the DC side will be converted as a third-order harmonic on the grid side that is the primary problem for the single-phase PV inverter systems. The main purpose of this study is to eliminate the 3rd order harmonics in grid side that stems from 2nd order harmonic component in PV side caused by the Dc-link voltage variations due to MPPT.

According to the IEEE Std 519-1992, total harmonic distortion (THD) shall be less than 5% of the current at the fundamental frequency at rated power output of the inverter and the distortion limits of the individual harmonics shall be less than 4%, 2%, 1.5%,0.6% and 0.3% for 3rd to 9th , 11th to 15th ,17th to 21st, 23rd to 33rd and the odd harmonics above 33rd, respectively [12]. Achieving of this objective presents some considerable challenges in practice. Evaluating the performance of the single-phase GCI controller systems that is supplied with PV array DC under varying environmental conditions with the use of real PV panels in series or parallel according to the needs is practically impossible due to the lack of control over the irradiance and temperature and the requirement of large area, hence the use of PVEs has become compulsory [13], [14], [15]. A wide range of research papers have discussed the various controllers thoroughly by using conventional or advanced design techniques for the single-phase GCI systems [16], [17], [18], [19], [20], [21], [22].

The number of algorithms developed to extract the disturbing current and inject solely the smooth current to the grid has been proposed in literature. Among these the synchronous reference frame (SRF) and the instantaneous reactive power (IRP) theories are the most addressed applications in literature [23], [24]. The issue with applying these theories to single phase PV systems is that there is only one phase variable, which requires the creation of an additional virtual orthogonal variable that operates with a 90-degree phase shift at the fundamental frequency [25]. In addition to those common theories, another proposed technique for the current control and the compensation of the selected harmonics is the adaptive control which contains several algorithms within itself such as the Least Mean Square (LMS) [26], the Decorrelation Normalized Least Mean Square (DNLMS) [27] and the Fractional Normalized Least Mean Square (FNLMS) [28]. Even though the adaptive control method has higher

efficiency, its concept remains a challenge in terms of complexity and requirement of large number of calculations.

Alternatively, the Hysteresis Controller that is simple to implement and has fast response time with a drawback of generating variable switching frequency [29], [30], the Predictive Controller that tracks a reference signal with zero steady-state error with the drawbacks of its dependency on the accuracy of the system model to generate the reference current prediction precisely [31], [32], the Proportional-Integral (PI) Controller that is very simple and has the ease of implementation with drawbacks of inadequacy in tracking a sinusoidal reference signal with a zero steady-state error and having a poor disturbance rejection capability [30]. The Proportional-Resonant (PR) Controller proposes a solution to current control and harmonic mitigation problems associated with the aforementioned control techniques for the single-phase GCI systems [17], [19].

In this chapter a novel PR controller is designed by using notch filter dynamics based symmetrical pole placement method. The proposed PR controller design technique offers an alternative with its unprecedented approach. It delivers an outstanding performance in current control and harmonic mitigation for the single-phase PV inverter systems. It consists of a resonant path and an external proportional gain. The external proportional gain stands for a regulator for varying system parameters such as inverter input voltage (V_{dc}) and filtering inductor (L_{inv}) shown in Figure 6.1 and can be altered easily for different applications. The resonant path has unity proportional gain and adjustable integral gain. These parameters are independent of V_{dc} and L_{inv} that means the proposed PR controller establishes more robustness and reduction in the computational complexity and consequently the proposed PR controller provides cost-effectiveness and simple implementation.

6.2 The Proposed PR-P Controller and Harmonic Compensator Design

The PR controller has gained its popularity and become widely used current regulator for grid-connected single-phase systems [22], [33], [34].The PR controller offers several advantages, such as resolving the computational burden and complexity due to removal of Park transformations, providing great convenience and simplicity to implement [35].

Figure 6.2 shows a circuit diagram of a single-phase PVE supported grid connected inverter. A buck DC-DC converter-based PV emulator is employed as the PV source. The PV source is connected to the grid using a full bridge DC-AC converter. The MPPT algorithm is employed to maintain the voltage at the maximum power point of the PV source, which is then input to the PV inverter so that the PV inverter can control the DC link voltage following the maximum power point voltage. The inverter also controls the inverter output current injection to the grid.
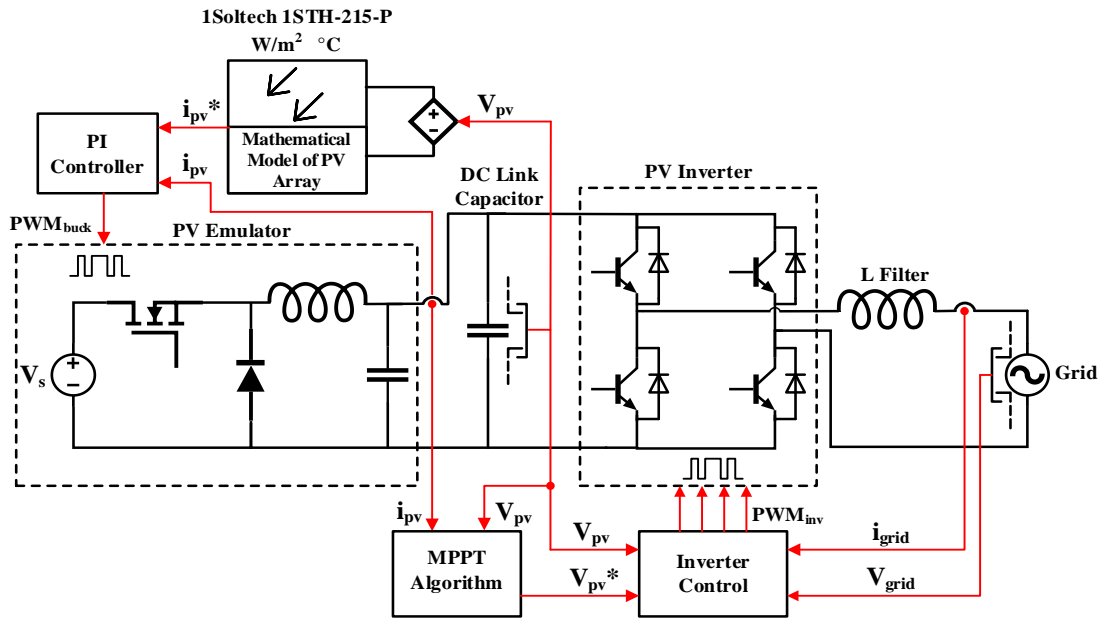
Figure 6.2: PVE based single phase grid-connected inverter system.

The ideal PR controller transfer function with its parameters proportional gain (K_P), integral gain (K_I) and the resonant frequency (ω_r) is represented by:

$$G_{PR}(s) = K_P + K_I \frac{s}{s^2 + {\omega_r}^2} \tag{6.5}$$

The ideal PR controller transfer function frequency response attains a phase shift and an infinite gain only at the resonant frequency (ω_r) that sets the steady-state error to zero and consequently enables to track sinusoidal reference signal efficiently at any specified resonant frequency. However, the ideal PR controller causes stability issues due to the infinite gain in applications [25]. Prevention of this problem is achieved with implementation of a non-ideal PR controller generated by introducing damping to the

ideal transfer function [18],[19]. The non-ideal PR controller transfer function with addition of the bandwidth (ω_c) around the ac resonant frequency (ω_r) is represented by:

$$G_{PR}(s) = K_P + K_I \frac{2\omega_c s}{s^2 + 2\omega_c s + \omega_r{}^2}$$

(6.6)

The non-ideal PR controller produces a finite gain at the resonant frequency ω_r but it is still large enough to provide a very small steady-state error that is almost zero [19]. The single-phase inverter control process is comprised of three parts basically which are DC-link voltage controller, grid synchronization and current controller. Block diagram of the inverter control including all parts is given in Figure 6.3.
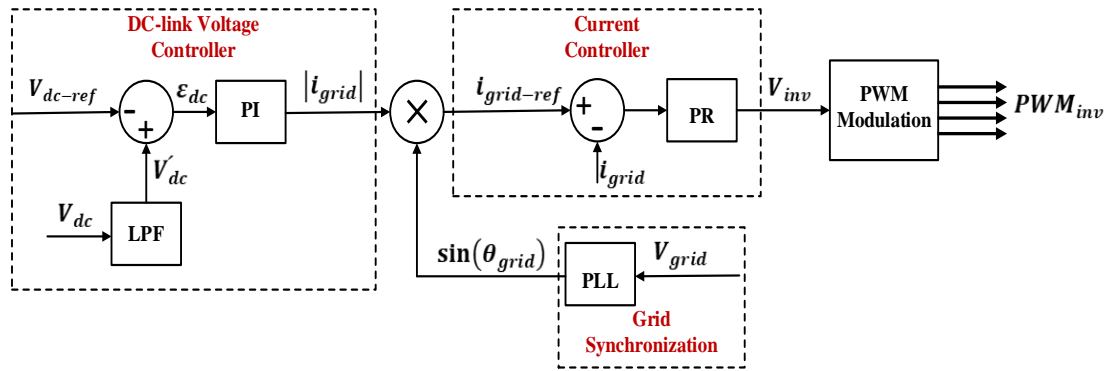
Figure 6.3: Block diagram of the inverter control.

The parameter k is set to adjust the width of the notch, the damping ratio (ξ) is set to adjust the depth of the notch and the natural frequency (ω_n) is set to adjust the location of the notch that refers to resonant frequency for the PR controller. In [36], the value of ξ is recommended as 0.001 and the value of k is chosen in the range of 1 to 5 considering the location of dominant poles for providing sufficient damping and preventing high frequency issues [16]. Frequency response of the notch according to varying ξ and k is given in Figure 6.4.

(a) Frequency response with varying ξ.

(b) Frequency response with varying k.
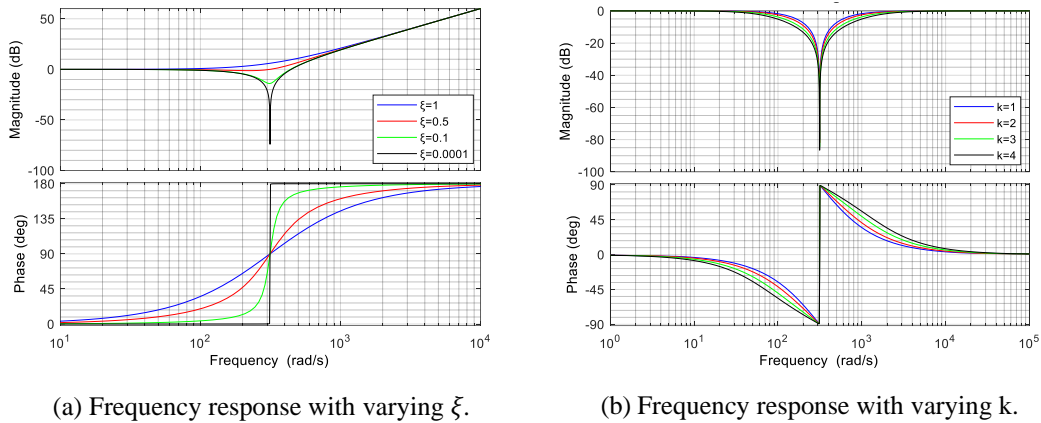
Figure 6.4: Phase and magnitude response of the proposed notch filter.

First, the variable (k) will be defined as the ratio of each pole is away from the natural frequency. The larger value of k corresponds with a wider notch and can be adjusted according to the requirement. An unrealizable transfer function $G(s)$ that is lightly damped ($\xi = 0.0001$) pair of zeros centred at the natural frequency ($\omega_n = 50\ Hz$) that corresponds to the resonant frequency of the PR and the parameter k (k=2) for the application have been chosen.

Figure 6.5 shows the frequency response of the unrealizable transfer function that is constituted with a greater order of numerator than denominator. There is a gain rising at 40 dB/decade since there are two unanswered zeros, thus the high frequency signals are to pass through altered.
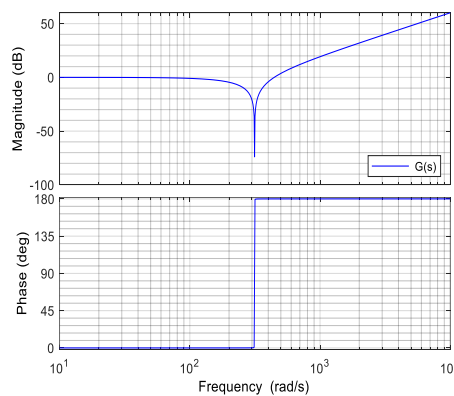
Figure 6.5: Lightly damped unrealizable transfer function.

Figure 6.6 shows that addition of a pole with a cut-off frequency that is k times larger than the natural frequency dragged the high frequency magnitude down by 20 dB/decade.

113
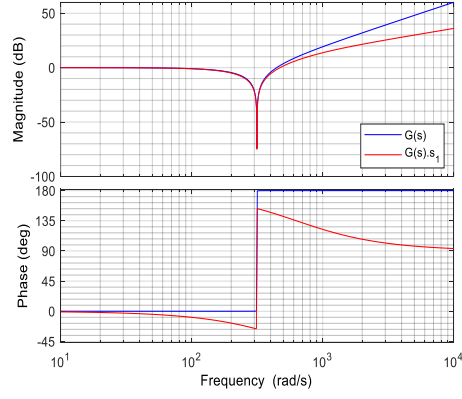
Figure 6.6: Addition of the first pole to the unrealizable transfer function.

Figure 6.7 shows that addition of a complementary pole with a cut-off frequency that is k times smaller than the natural frequency bended down the high frequency magnitude by 20 dB/decade to the zero dB.
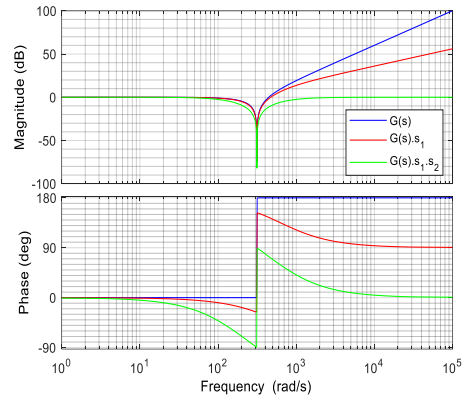
Figure 6.7: Addition of the second complementary pole to the unrealizable transfer function.

The transfer function of the proposed PR controller $G_{PR}(s)$ is the reciprocal of the notch filter transfer function $G_{notch}(s)$ is given as:

$$G_{PR}(s) = \frac{9.87 \times 10^4 s^2 + 7.752 \times 10^7 s + 9.741 \times 10^9}{9.87 \times 10^4 s^2 + 6201s + 9.741 \times 10^9} \qquad (6.7)$$

The magnitude and phase responses of the designed PR controller is given in Figure 6.8. The highest gain of the designed PR controller is 81.7 dB, and it occurs at the resonant frequency ($\omega_n = 50\ Hz$). The phase response shows that the phase shift is zero for low and high frequencies.

114
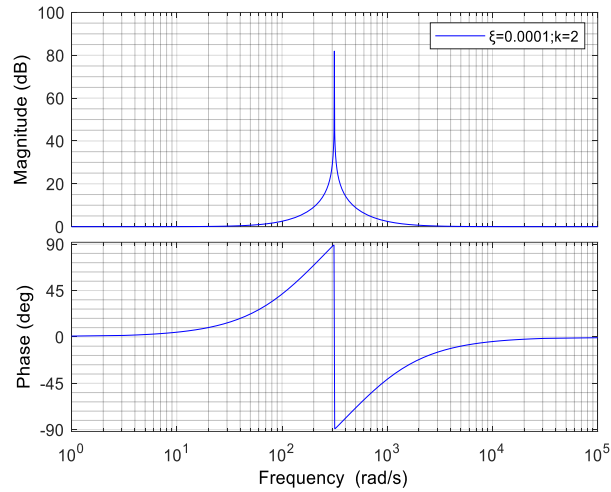
Figure 6.8: Magnitude and phase responses of the proposed PR controller.

Figure 6.8 indicates that for any arbitrary frequency ω_0, the gain of the PR controller transfer function $G_{PR}(j\omega_0)$ is at sufficient level without a phase shift for other frequencies, hence it can track sinusoidal reference signal without error.

6.2.1 The PR Controller with Harmonic Compensator

Grid connected inverter systems (GCI) mainly operate as transferring energy from the primary DC source such as PV arrays to the grid and hence inject harmonic currents to act as an active filter. In this regard, the reference signal is constituted of the sum of the fundamental component and some harmonic components (e.g., 3rd, 5th, 7th order harmonics). The PR controller assures zero steady-state error for any harmonic components at issue by implementing additional resonant paths to the controller. The block diagram of the general system with a PR controller that consists of n-resonant paths is given in Figure 6.9.
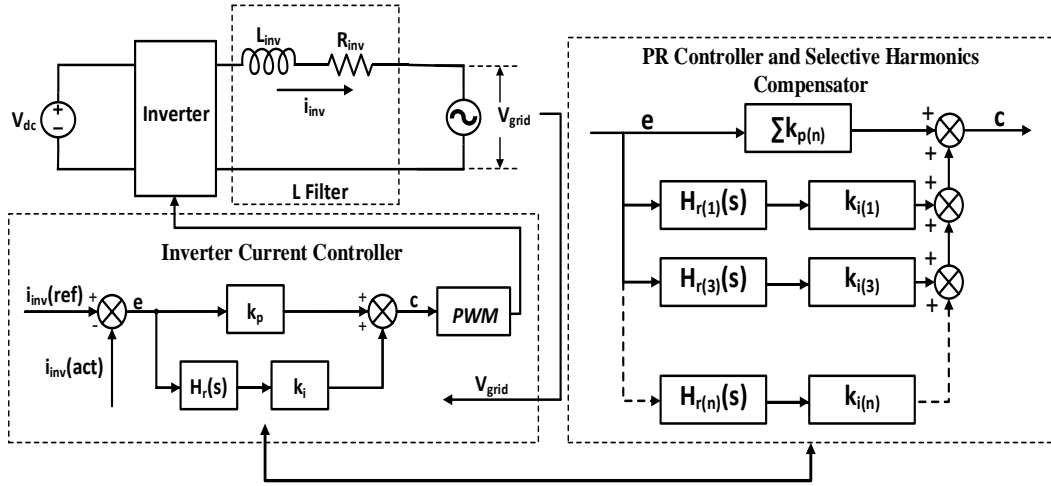
Figure 6.9: The proposed PR controller with n-resonant paths.

General form of the selective harmonic compensator transfer function $G_H(s)$ is represented by:

$$G_H(s) = \sum_{h=3,5,7,\dots} \frac{(h\omega_n)^2}{s^2 + 2\xi h\omega_n s + (h\omega_n)^2} \times \frac{s + kh\omega_n}{kh\omega_n} \times \frac{s + \frac{h\omega_n}{k}}{\frac{h\omega_n}{k}} \qquad (6.8)$$

In the design of objective resonant paths, the same pole placement notch filter dynamics-based technique that is previously stated will be implemented. The only changing parameters is the resonant frequencies. The resonant frequency for the fundamental component is 50 Hz (ω_n), for the 3rd order harmonic component 150 Hz ($3\omega_n$) and for the 5th order harmonic component 250 Hz ($5\omega_n$). The magnitude and phase responses of the designed PR controller with the 3rd and the 5th harmonics compensator is given in Figure 6.10.
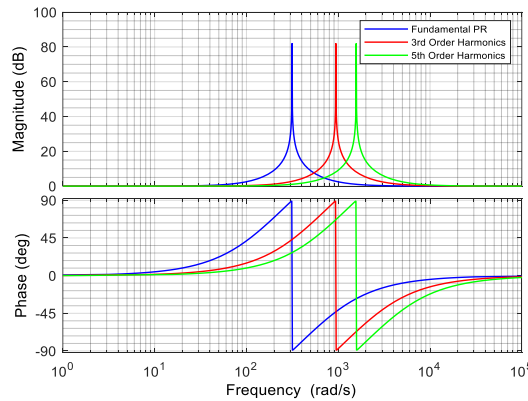
Figure 6.10: Magnitude and phase response of the designed PR controller with the 3rd and the 5th harmonic components compensator.

6.2.2 Comparative Analysis of the Proposed PR-P Controller

The PR controller consists of the main frame (the resonant path $H_R(s)$) and fundamental parameters (the proportional gain (K_P) and the integral gain (K_I)) for the single-phase grid connected full-bridge inverter. Components of the PR controller are formulized as [37]:

$$H_R(s) = \frac{k_r B_r s}{s^2 + 2B_r s + \omega_r^2} \tag{6.9}$$

$$K_P = \frac{(2\xi + 1)\sqrt{(2\xi + 1)}\omega_r L_{inv}}{V_{dc}} \tag{6.10}$$

$$K_I = \frac{\omega_r^2 L_{inv}[(2\xi + 1)^2 - 1]}{2V_{dc}} \tag{6.11}$$

Equation (6.9), (6.10) and (6.11) consist of various parameters that are resonant gain (k_r), resonant angular bandwidth (B_r), resonant angular frequency (ω_r), damping ratio (ξ), inverter output filter inductance (L_{inv}), inverter input voltage (V_{dc}) and constitute commonly used non-ideal PR controller transfer function design given in (6.6). In [38], it is presented that the most frequently used conventional PR controller poses problems in the presence of non-linear load and weak grid condition. In [39] and [40], studies were performed by utilizing this formula and it provides consistent results in terms of transient response and selective harmonics mitigation but the number of parameters used in the design process increases the complexity of the controller. Moreover, dependency on the variables such as (L_{inv}) and (V_{dc}) in the calculations of the K_P and K_I decreases the robustness of the controller as these variables are likely to change over time or to vary during operations. On the contrary, the PR path of the proposed PR-P controller design process is independent of these variables. Rearranging the PR path of the controller transfer function gives:

$$G_{PR}(s) = 1 + \frac{\left(\frac{\omega_n}{k} + k\omega_n - 2\xi\omega_n\right)s}{s^2 + 2\xi\omega_n s + \omega_n^2} \tag{6.12}$$

The proposed controller resonant path has a constant unity proportional gain K_P and addition of each harmonic reduction component increases it 1. K_I depends only on three

parameters that are k, ω_n and ξ. The assessment of the PR path of the proposed controller indicated that using $G_{PR}(s)$ obtained in (6.12) meets the IEEE Std 519-1992 standards with a sufficiently good transient response. Addition of scheduled proportional gain ($K_{P(ex)}$) determined by loop shaping method to the resonant path PR considering system uncertainties, weak grid condition, non-linear loads and grid fault has resolved the problems associated with the use of conventional PR controller. In this regard, the proposed PR-P controller can be considered as a system consisting of unity proportional gain resonant path $G_{PR}(s)$ and controllable variable $K_{P(ex)}$ given in Figure 6.11(a). The overall current control and selective harmonic mitigation scheme for GCI systems is given in Figure 6.11(b).
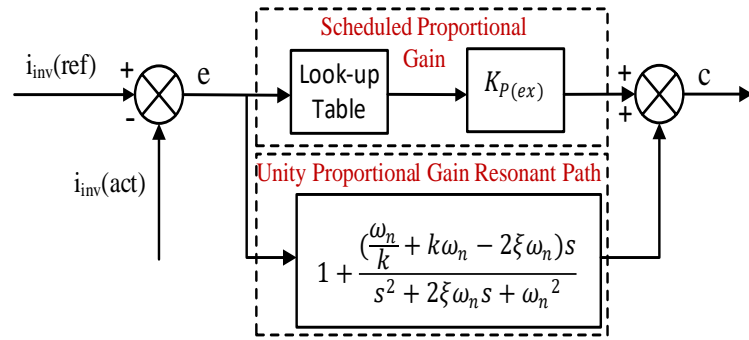
(a) The proposed PR-P controller
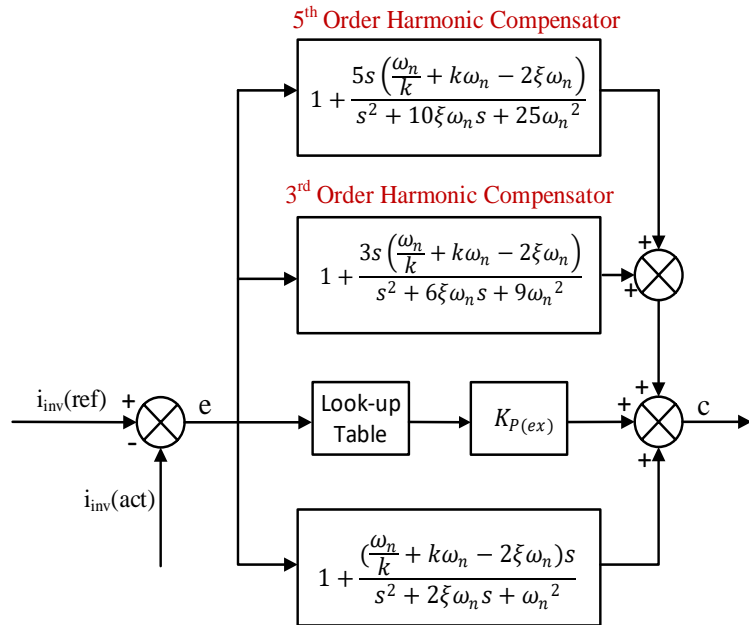
(b) The proposed PR-P controller and harmonic compensator

Figure 6.11: The proposed PR-P controller with 3rd and 5th order harmonic components compensator.

6.2.3 Tuning the Scheduled Gain of the Proposed Controller

Large signal average model of the full-bridge inverter given as:

$$L\frac{d\langle \hat{i}_{inv}\rangle}{dt} = (2d-1)V_{dc} - v_{ac} \qquad (6.13)$$

where L, $\langle \hat{i}_{inv}\rangle$, d, V_{dc} and v_{ac} are the inductance of the inverter filter, duty cycle of the inverter PWM signal, input voltage of the inverter and grid voltage, respectively. Assuming that there is no small signal variation in v_{ac} as the control input is the duty cycle, linearization of (6.13) gives:

$$L\frac{d\hat{i}_{inv}}{dt} = 2V_{dc}\hat{d} \qquad (6.14)$$

Laplace transform of (6.14) gives small-signal transfer function of the inverter as:

$$sL\hat{i}_{inv} = 2V_{dc}\hat{d}$$
$$G_{inv}(s) = \frac{\hat{i}_{inv}}{\hat{d}} = \frac{2V_{dc}}{Ls} \qquad (6.15)$$

The power inverter input voltage is 400 V, and it is connected to the grid via L filter whose inductance is 1 mH. Accordingly, substituting these values in (6.15) yields:

$$G_{inv}(s) = \frac{\hat{i}_{inv}}{\hat{d}} = \frac{800}{0.001s} \qquad (6.16)$$

Magnitude and phase response of the loop transfer function that is $G_{PRP}(s)$ times $G_{inv}(s)$ with varying $K_{P(ex)}$ is given in Figure 6.12.
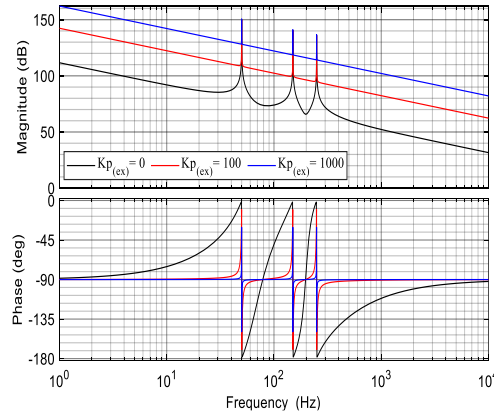
Figure 6.12: Magnitude and phase responses of the loop transfer function with varying $K_{P(ex)}$.

The look-up table breakout points correspond to closed-loop current feedback error and the outputs are retrieved from a given set of breakout points (input values) as scheduling variables for the constant $K_{P(ex)}$ whose value is determined as 100 according to the loop transfer function magnitude and phase response given in Figure 6.13.
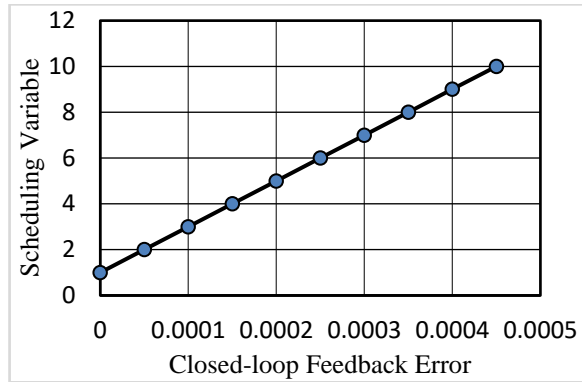
Figure 6.13: Dynamics of the look-up table.

The look-up table method is based on linear interpolation between two consecutive elements of the table if the error signal does not match a breakout point and extrapolation if the error is not falling within the range of breakout values. Average current mode control loop of the inverter assumed that pulse width modulator (PWM) gains 4 V, sensing resistor R_F 1 Ω with all harmonics injecting is given in Figure 6.14.
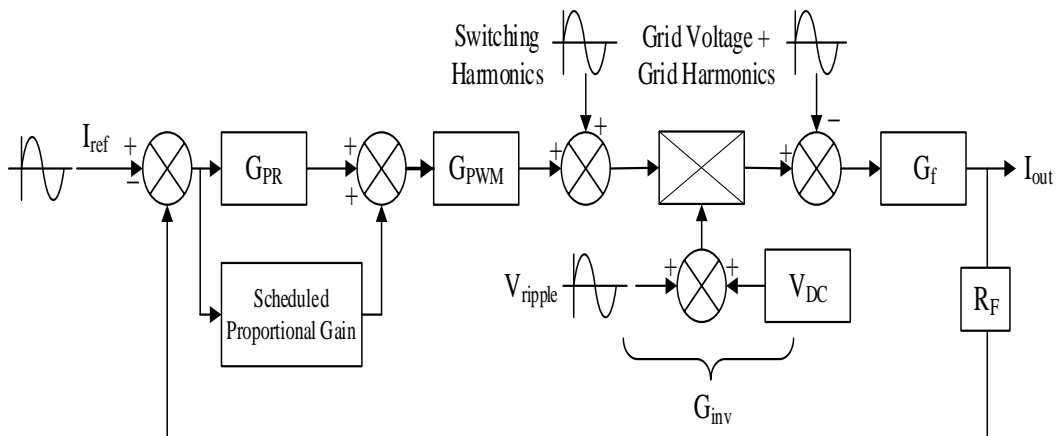
Figure 6.14: Inverter average current mode compensator design loop.

Inverter average current control feedback system outputs for implementation of different controllers are given in Figure 6.15. While most frequently used PI and

conventional PR control techniques perform poorly in the presence of harmonics, the proposed PR-P controller follows its reference with negligible steady-state error.
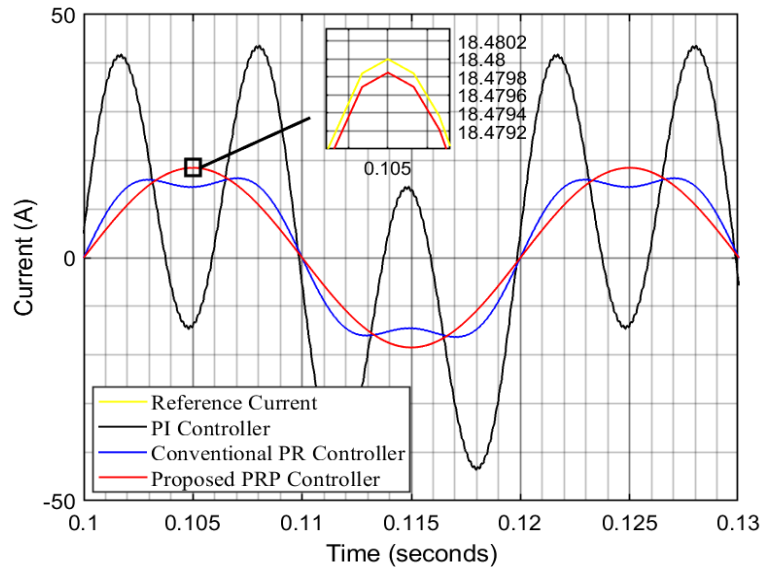
Figure 6.15: Reference tracking performance of the various controllers in the presence of harmonics.

6.3 PVE and MPPT Algorithm

The current-voltage (I-V) and the power-voltage (P-V) characteristics curves of the PV cells are heavily dependent on changing environmental conditions such as irradiance and temperature [41]. In accordance with the efficiency-based aforesaid objectives in the introduction, maintaining the characteristic curves at a specific point that is known as the maximum power point (MPP) is required [42]. In this regard, maximum power point tracking (MPPT) concepts are employed at PV array in practice to harvest the maximum power from the PV module or array under various irradiance and temperature conditions [43].

Tracking performance of the MPPT algorithms has great importance, hence it has been the main subject of many studies and different methods are developed in consequence [44], [45], [46] . Development and improvement of MPPT techniques with the real PV panels posed some challenges such as being inability to control the environmental factors, requirement of wide space and cost [13], [47]. At this point, photovoltaic emulators (PVE) have become the essential part of the PV applications in terms of

development of the MPPT algorithms [48]. The working principle of the PVE is based on generating the explicit dynamics of the I-V and P-V characteristics curves of the real PV panel at issue [14], [49].

It is worth noting that whilst the objective PVE delivers a good performance by itself, it may exhibit undesirable behaviours as a result of interfacing with some switch mode power supplies that constitute the indispensable of the PV power generation and delivering systems or it may not reflect the same PV characteristics through the variance of the irradiance and the temperature [50], [51], [52]. Referring to the previous works taking part in literature, many different PVE modelling and simulations have been conducted and these PVEs have designed with pure resistive load and their I-V and P-V curves compared with the real PV panel or they are integrated with a Boost Converter for the MPPT applications [13], [15], [50], [51], [53].

6.3.1 Design Procedure of the PVE

This chapter proposed scrutinization of buck converter based PVE single phase grid-connected H-bridge inverter system with a maximum power point tracking (MPPT), a proportional-resonant-proportional controller (PR-P) for the purpose of the current control as well as 3rd and 5th order harmonics mitigation with the aid of multiple domains of MATLAB and Simulink. The emulated PV module is 1Soltech 1STH-215-P with parameter given in Table 6.1.

Table 6.1: The emulated PV module (1Soltech 1STH-215-P) Parameters.

Parameter	Value
Maximum Power (W)	231.15
Open Circuit Voltage V_{OC} (V)	36.3
Voltage at Maximum Power Point V_{MPP} (V)	29
Temperature Coefficient of V_{OC} (%/$deg.C$)	-0.36099
Cells per Module (Ncell)	60
Short-circuit Current I_{SC} (A)	7.84
Current at Maximum Power Point I_{MPP} (A)	7.35
Temperature Coefficient of I_{SC} (%/$deg.C$)	0.102

The proposed buck converter based PVE, and its control structure block diagram is given in Figure 6.16.
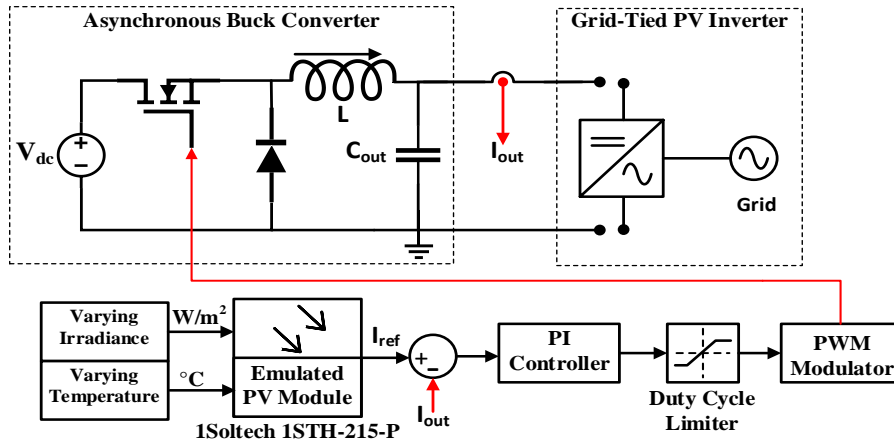
Figure 6.16: The proposed buck converter based PVE and control structure.

The module takes an input voltage (V_{dc}) of 48 volts and converts it into an output voltage of 36.3 volts. The switching frequency is 10 kHz. The minimum load resistance R_{min} is 4.6301 ohm (corresponds to the maximum load condition). In the continuous conduction mode (CCM) operation of the PVE, the maximum ripple allowed in the inductor is 20% of the average inductor current and the maximum load. The maximum ripple in the capacitor is plus and minus 2% of the average output voltage.

The output voltage (V_{out}) of the PVE corresponding to the inverter input voltage is determined as 400 V in this application, thus the PVE is considered as the series connection of 14 PV modules that results in approximately 3 kW power generation.

6.3.2 Calculations of the Values of PV Emulator Components

The steady state duty cycle of the plant is represented by:

$$D = \frac{V_{out}}{V_{in}} \tag{6.17}$$

The maximum average inductor current is represented by:

$$I_{L,avg,max} = \frac{V_{out}}{R_{min}} \tag{6.18}$$

123

The maximum average inductor ripple current is the 20% of the average current that is represented by:

$$\Delta I_L = 0.2 I_{L,avg,max} \tag{6.19}$$

Inductance value L of the inductor is represented by:

$$L = \frac{V_{in}(1-D)D}{f_{sw}\Delta I_L} \tag{6.20}$$

Capacitor ΔV_C or output voltage ripple ΔV_{out} is the $\pm 2\%$ of the average output voltage is represented by:

$$\Delta V_C = \Delta V_{out} = 0.04 V_{out} \tag{6.21}$$

Capacitance value C of the capacitor is represented by:

$$C = \frac{V_{in}(1-D)D}{8Lf_{sw}{}^2\Delta V_C} \tag{6.22}$$

The calculated values of the PV emulator parameters and components are given in Table 6.2.

Table 6.2: Proposed PVE parameters and components calculated values.

Parameters and Components	Value
Steady-state Duty Cycle	0.7563
Maximum Average Inductor Current (A)	7.84
Maximum Average Inductor Current Ripple (A)	1.568
Inductor Value (mH)	0.5642
Output Voltage Ripple (V)	1.452
Capacitor Value (µF)	13.4989

6.3.3 Proportional-Integral (PI) Controller Design for the PVE

Analysis of the plant for predicting its response and observing its behaviours in both the time and frequency domains requires obtaining its mathematical model properly. In this regard, control systems are designed and implemented to improve important dynamic

properties of the plant such as stability, response time, steady-state error, oscillations that constitute the transient and the steady-state responses of the system.

Transfer function of the intended buck converter based PVE in terms of duty ratio (d(s)) to inductor current (i_L(s))is derived by using a dynamic (AC small signal) state-space averaging technique is given by:

$$G_{PVE}(s) = \frac{i_L(s)}{d(s)} = \frac{V_{in}}{L} \cdot \frac{s + \frac{1}{R_{Load}C}}{s^2 + \frac{s}{R_{Load}C} + \frac{1}{LC}} \qquad (6.23)$$

$$G_{PVE}(s) = (8.5063 \times 10^4) \cdot \frac{s + 1.6 \times 10^4}{s^2 + 1600s + 1.3128 \times 10^8} \qquad (6.24)$$

The Proportional-Integral (PI) feedback compensator structure is a controller that is widely used due to the properties of being simple to implement, easily comprehensible, very understandable and its effectiveness. The unity feedback structure of the proposed PVE system is given in Figure 6.17:
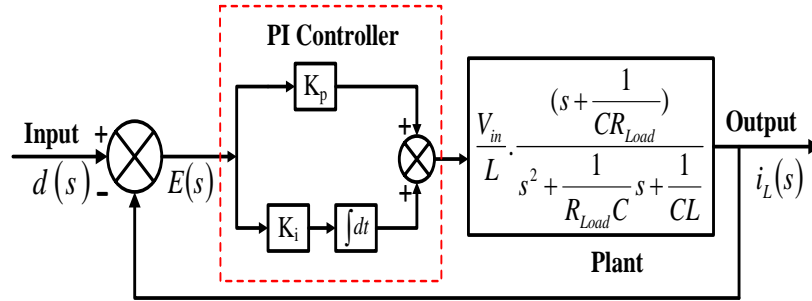
Figure 6.17: The unity feedback control structure of the proposed PVE.

The closed-loop transfer function of inductor current to the duty ratio for the unity-feedback system with a proportional-integral control is the following:

$$G_{CL}(s) = \frac{V_{in}K_p}{L}[s^2 + s\left(\frac{1}{CR_{Load}} + \frac{K_i}{K_p}\right) + \frac{K_i}{K_pCR_{Load}}]$$

$$\div [s^3 + s^2\left(\frac{1}{CR_{Load}} + \frac{K_pV_{in}}{L}\right) \qquad (6.25)$$

$$+s\left(\frac{1}{CL} + \frac{K_pV_{in}}{CLR_{Load}} + \frac{K_iV_{in}}{L}\right) + K_iV_{in}]$$

Considering the stability criteria of a switch mode power supply (SMPS) which are the crossover (cut-off or break) frequency between the range of 1/10th to 1/8th of the switching frequency, the phase margin larger than 45 degrees, the gain margin larger than 10 dB and the slope of the gain curve at the crossover frequency is about -20 dB/decade, K_p and K_i values are calculated as 0.21 and 709, respectively. Emulated PV module (1Soltech 1STH-215-P) and the proposed PV emulator controlled by the designed PI controller current waveforms for varying irradiance of 1000 W/m², 800 W/m², 600 W/m² and 250 W/m² (severe shading pattern) that correspond to 7.84 A, 6.272 A, 4.704 A and 1.844 A, respectively are given in Figure 6.18.
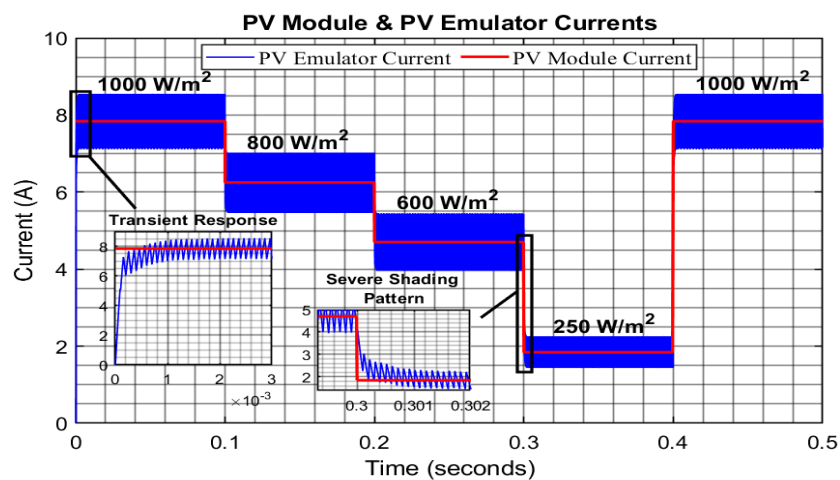
Figure 6.18: The emulated PV module and designed PVE currents.

6.3.4 Perturb and Observe (P&O) MPPT Algorithm

The P&O MPPT technique is one of the most basic and commonly used algorithms in PV systems. Implementation of the algorithm depends on the trial-and-error method in pursuit of maximum power point (MPP) and tracking it [41]. The method is required to measure only the PV array's current and voltage to calculate the power and perturbing the duty cycle based on the comparison of the initial and present values of the power and voltage until reaching the MPP occurring at MPP voltage (VMPP) [54]. The use of current and voltage sensors only causes relatively big reduction in the operational cost. Moreover, its convenience and compatibility with the grid-tied converter systems due to effective regulation of the output voltage and dynamic performance in terms of fast response time is considered as the notable feature of the algorithm [46], [50]. The

flowchart of the algorithm and accordingly its execution on the power-voltage (P-V) characteristics curve of the PV module is explained in Chapter 4.

The parameters of the developed algorithm are 400 V initial value of the voltage reference that corresponds VMPP and the input voltage of the inverter, 410 V upper limit and 390 V lower limit. Increment value used to increase or to decrease the voltage is 0.003 V.

6.4 Simulation Results and Discussions

This chapter proposed a novel approach to design a PR-P controller that is based on changing notch filter dynamics by implementing of two symmetrical poles to both sides of the resonant frequency at which the control is aimed and taking the reciprocal of the derived transfer function. In addition to this, the performance of the PR-P controller is validated under real-like developed switch mode power supply (SMPS) PVE sourced single-phase GCI system.

The simulation of the PVE supported single phase grid connected inverter with the proposed PR-P controller was performed in MATLAB/Simulink by assuming inverter switching frequency is 6 kHz, peak value of the grid voltage is 340 V, and the frequency is 50 Hz. Figure 6.19 shows the current output of the PVE under varying irradiance. The PI controller for the PVE reveals good performance in terms of transient response and tracking the emulated PV module current given in Table 6.1. The system reaches steady state in less than 1 millisecond in line with the reference current.
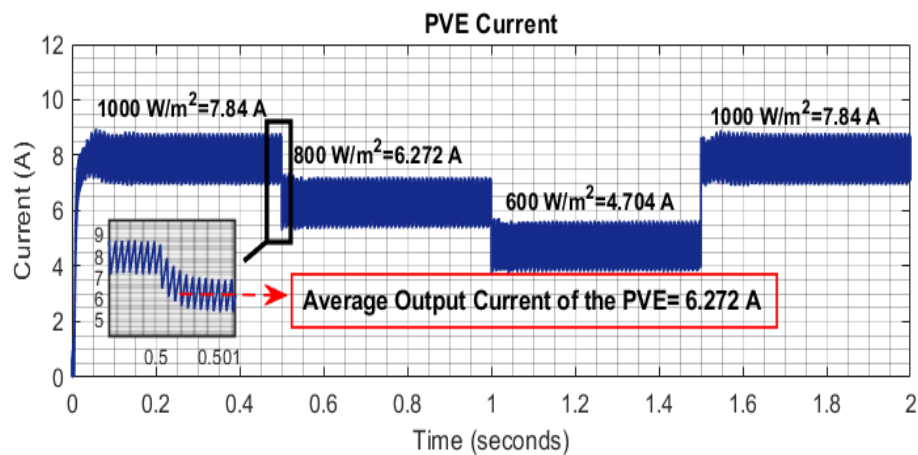
Figure 6.19: The PVE current for varying irradiance.

Figure 6.20 shows the voltage output of the PVE under varying irradiance. The designed P&O MPPT algorithm performs well and tracks the reference voltage of 400 V effectually if there is not big variation in the irradiance. The reason for the poor transient response for the abrupt and significant shift in the irradiance occurred at the very beginning when the irradiance changed from 0 to 1000 W/m^2 and from 600 W/m^2 to 1000 W/m^2 at 1.2nd second is due to the fixed step size of $\Delta V = 0.003$ V.
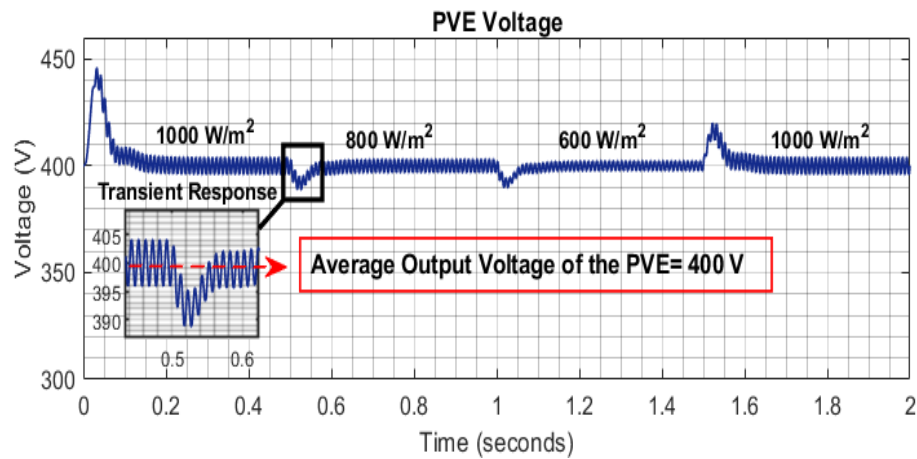
Figure 6.20: The PVE voltage for varying irradiance.

Figure 6.21 presents the inverter output current and reference current behaviours in both stages of stepping from a null current to a sinusoidal waveform and transient response after the sinusoidal waveform.
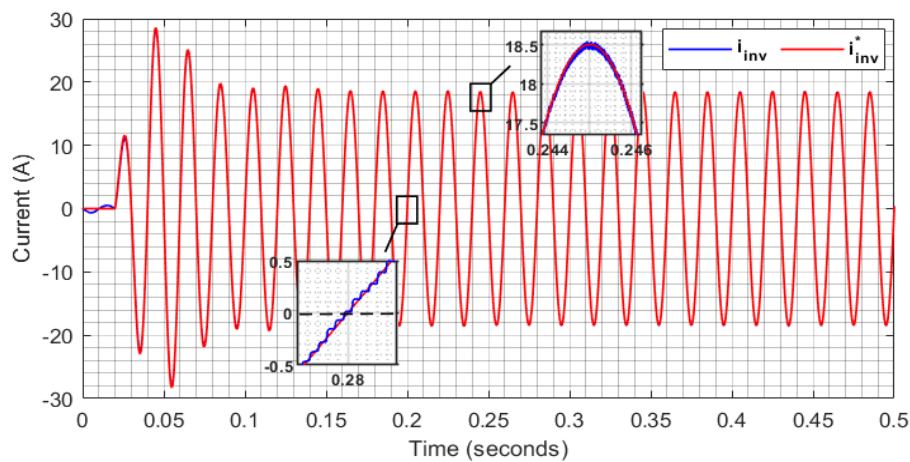
Figure 6.21: Reference and inverter output currents.

The proposed PR-P controller functions properly and makes the inverter current follows the reference current with negligible steady-state error and consequently maintains the

grid voltage and current in phase as shown in Figure 6.22. The transient period takes approximately 0.06 second with insignificant oscillation in the inverter current that denotes the rapid response of the controller.
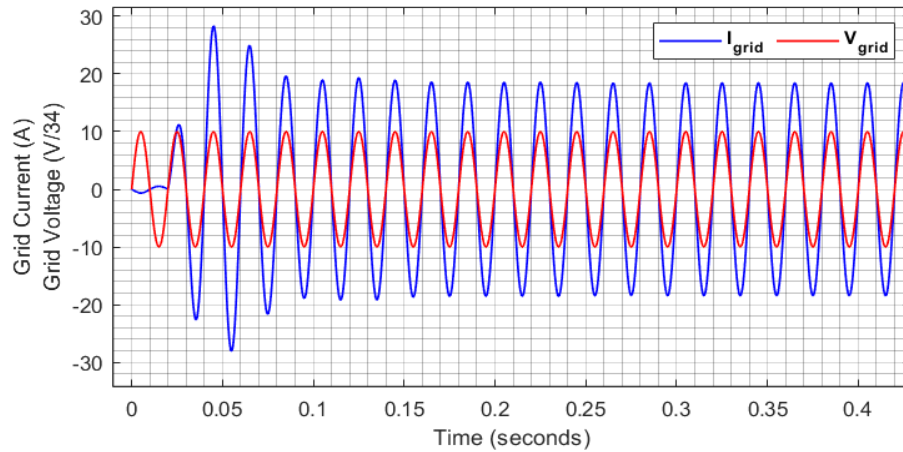
Figure 6.22: Grid current and scaled grid voltage.

Power generation for varying irradiance and its deliver through an inverter in terms of active and reactive powers are giving in Figure 6.23. The power generation, conditioning and its deliver to the grid process is accomplished efficiently with zero reactive power. The transient regime stems from the output voltage waveform of the PVE as indicated in Figure 6.20.
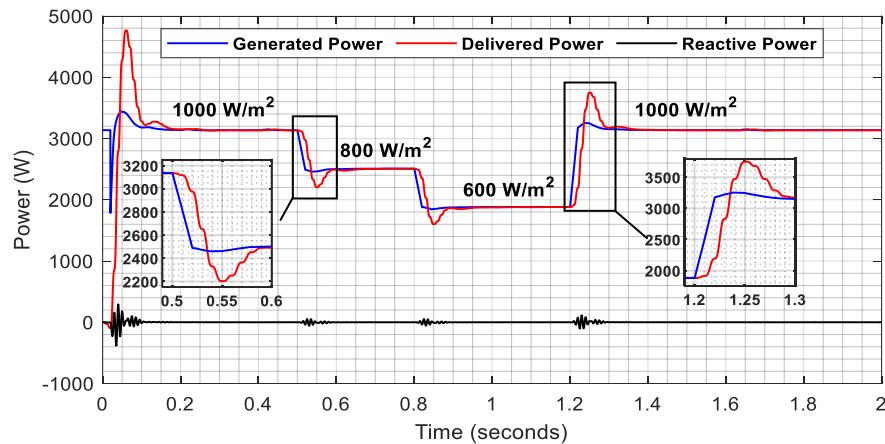
Figure 6.23: Generated power with delivered and reactive powers.

Table 6.3 presents total harmonic distortion (THD) of the grid current for varying frequencies for the cases of implementing unscheduled PR-P controller itself, PR-P controller with 3rd order harmonic compensator and PR-P controller with both 3rd and 5th order harmonic compensator assuming that $K_{P(ex)}$ is zero.

Table 6.3: Implementing of the unscheduled PR-P controller with harmonic compensator.

Magnitude of Harmonic Distortion (% of Fundamental)	PR-P controller without scheduled proportional gain $K_{p(ex)}$		
	Without harmonic compensator	Implementing 3rd order harmonic compensator	Implementing 3rd and 5th order harmonic compensators
THD	4.68	4.65	4.64
3rd order harmonic component	0.4149	0.0008684	0.001779
5th order harmonic component	0.1519	0.06788	0.0005461
7th order harmonic component	0.02581	0.03124	0.04333
9th order harmonic component	0.137	0.07815	0.04409
11th order harmonic compoennt	0.02715	0.08445	0.03253

In Table 6.4, the PR-P controller and 3rd and 5th order harmonics compensators are implemented with $K_{P(ex)}$ value of 20 by considering variation in the inverter output inductor values.

Table 6.4: Constant proportional gain ($K_{P(ex)} = 20$) PR-P controller with 3rd and 5th order harmonics compensator with varying inverter output inductor values.

Magnitude of Harmonic Distortion (% of Fundamental)	PR-P controller with constant proportional gain $K_{p(ex)}$=20 with 3rd and 5th order harmonic compensators		
	L_{inv}= 1 mH	L_{inv}= 3 mH	L_{inv}= 5 mH
THD	1.90	1.79	1.64
3rd order harmonic component	0.001909	0.00176	0.002072
5th order harmonic component	0.001138	0.001344	0.001361
7th order harmonic component	0.2354	0.268	0.1677
9th order harmonic component	0.2003	0.1931	0.1202
11th order harmonic compoennt	0.1488	0.1232	0.07186

The same application is carried out with a constant inductance and varying $K_{P(ex)}$ values in Table 6.5. The results shows that the performance of the proposed control scheme is satisfactory and in compliance with the IEEE Std 519-1992.

Table 6.5: Constant inverter output filtering inductance (L=3 mH) with varying $K_{P(ex)}$ values PR-P controller with 3rd and 5th order harmonics compensator.

Magnitude of Harmonic Distortion (% of Fundamental)	PR-P controller with scheduled proportional gain K$_{p(ex)}$ + 3rd and 5th order harmonic compansators Constant Inverter Filtering Inductance L$_{inv}$= 3 mH		
	K$_{p(ex)}$= 0	K$_{p(ex)}$= 10	K$_{p(ex)}$= 20
THD	4.64	0.49	0.49
3rd order harmonic component	0.00389	0.04725	0.04776
5th order harmonic component	0.001712	0.03015	0.03001
7th order harmonic component	0.04379	0.02842	0.02831
9th order harmonic component	0.04727	0.008881	0.008885
11th order harmonic compoennt	0.03033	0.0004584	0.00172

The main drawbacks of the PI controller in single phase GCI systems are insufficiency in removing the steady-state error in stationary reference frame shown in Figure 6.24 and being incapable of selective harmonics mitigation.
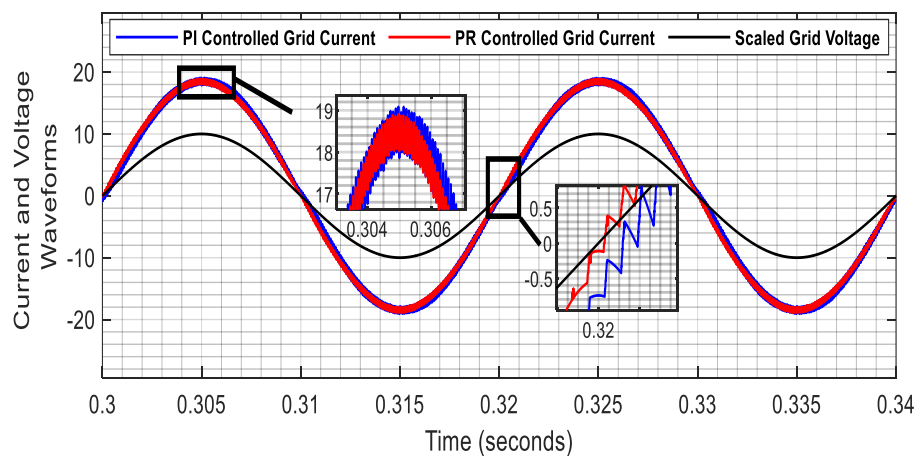
Figure 6.24: The PR-P and PI controlled grid currents with scaled grid voltage.

Closed loop errors of PR and PI controllers are presented in Figure 6.25, The 3rd order harmonic component is eliminated within a quarter second with the proposed PR controller. However, the use of PI controller results in a constant error regarding the 3rd order harmonic component in the grid current. The PR controller is more efficient in terms of harmonic compensation and removing the steady-state error.
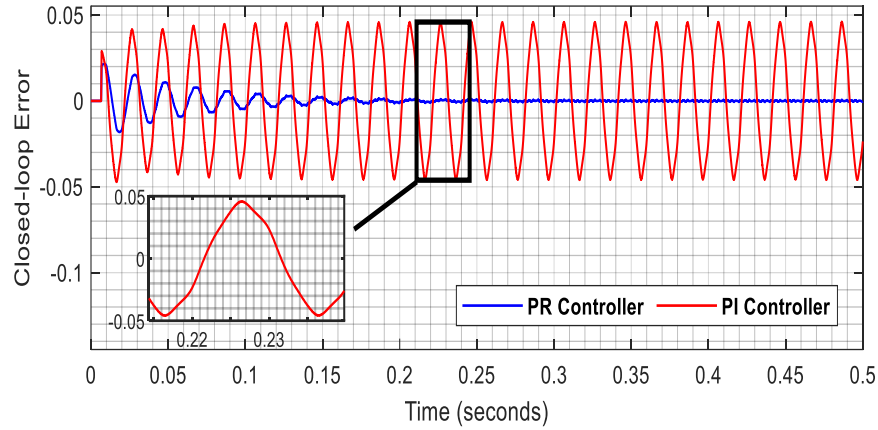
Figure 6.25: Closed-loop error in terms of 3rd order harmonics.

Performance validation of the proposed PR-P controller involves checking its efficiency compared with PI controller in the presence of severe shading pattern, non-linear load and weak grid that constitute the main concerns in grid connected applications. The general structure of the overall system given in Figure 6.26.
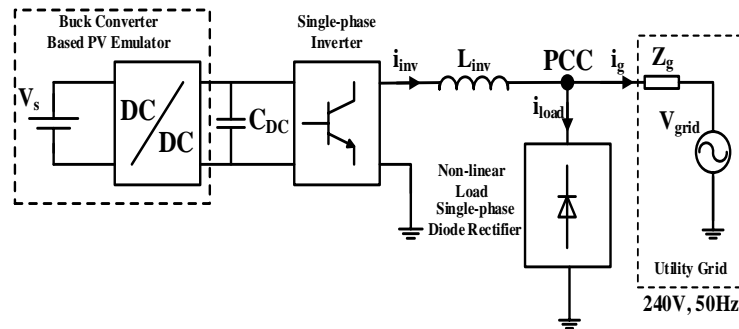
Figure 6.26: Single-phase PVE sourced grid-connected inverter system in the presence of non-linear load and weak grid.

Parameters of the buck converter based PVE sourced single phase grid connected inverter system is given in Table 6.6.

Table 6.6: The simulated system parameters.

Parameter	Value
Grid phase voltage (rms)	V_{grid}=240V
Grid frequency	f=50Hz
Inverter filtering inductance	L_{inv}=3mH
Average DC-bus voltage	V_{dc}=400V
DC-bus capacitor	C_{DC}=3000µF
Inverter switching frequency	f_{sw}=6kHz

Single phase transmission line with lumped parameters is given in Table 6.7.

Table 6.7: Transmission line parameters.

Transmission Line Parameters	Value
Resistance per unit length	0.2568 Ohms/km
Inductance per unit length	2 mH/km
Capacitance per unit length	8.6 nF/km
Line lenght	10 km

Figure 6.27 shows that PI current control of the PVE sourced single phase grid-tied inverter resulted in deterioration and distortion of the current while proposed PR-P controller gives better results in the presence of non-linear load and weak grid.
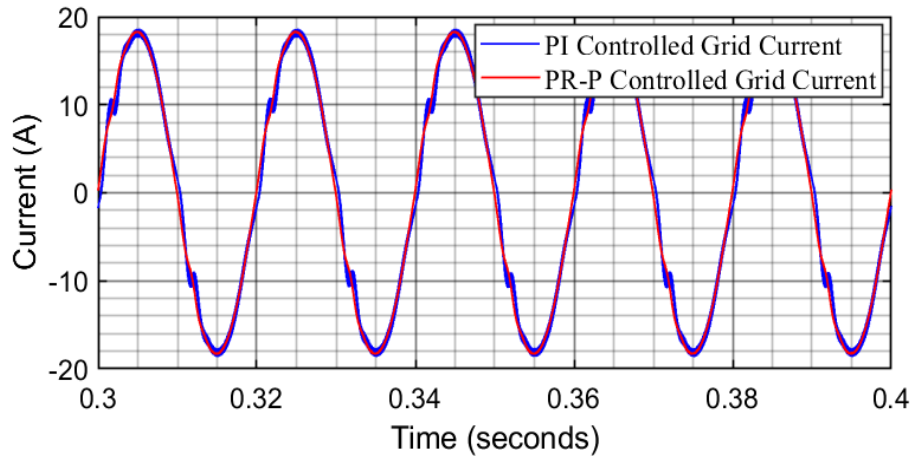
Figure 6.27: The PR-P and PI controlled grid currents.

Figure 6.28 indicates that closed-loop error in terms of the 3rd order harmonic component is mitigated by the proposed PR-P controller effectively while PI controller is inefficient of selective harmonic compensation. Additionally, the proposed PR-P controller responds swiftly to sudden large irradiance change with less oscillation compared to PI controller.
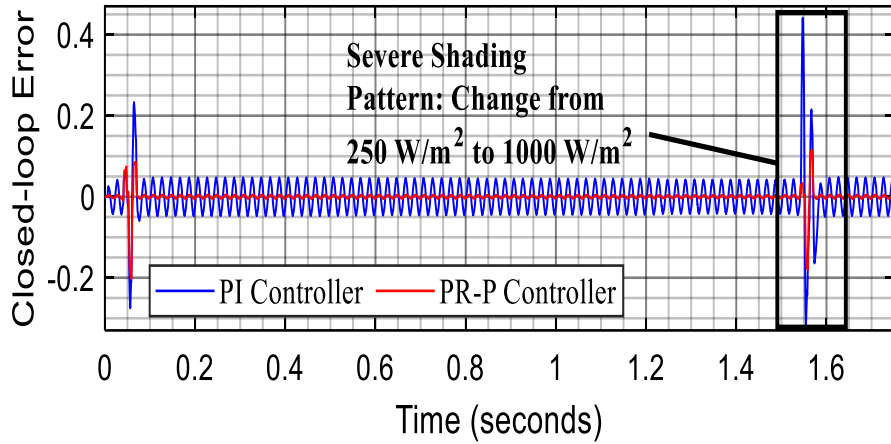
Figure 6.28: 3rd order harmonic component closed-loop error.

Table 6.8 shows low order harmonic distortions of grid current and voltage waveforms for PI and proposed PR-P controller in the presence of non-linear load and weak grid. The THD value of grid current is 6.59 % with PI controller; however, the THD value of the grid current 1.88 % with the proposed PR-P controller. The THD value of the grid current is reduced 79.81% with the use of proposed PR-P controller. The results verify the effectiveness of the proposed PR-P control method in attenuation of the disturbing current in the presence of non-linear load and weak grid condition.

Table 6.8: Comparison of harmonic distortions for the PR-P and PI controllers in the presence of non-linear load and weak grid.

| Magnitude of Harmonic Distortion (% of Fundamental) | Harmonic Distortion in the Presence of Non-linear Load and Weak Grid | | | |
| | PI Controller | | PR-P Controller | |
	Grid Voltage (V)	Grid Current (A)	Grid Voltage (V)	Grid Current (A)
THD	9.22	6.59	3.52	1.88
3rd order harmonic component	0.6419	1.054	0.2416	0.2843
5th order harmonic component	1.442	1.655	0.4919	0.5301
7th order harmonic component	3.023	3.227	0.7997	0.7814
9th order harmonic component	3.211	3.331	1.046	1.015
11th order harmonic compoennt	2.444	2.519	0.9266	0.9263

6.4.1 Sensitivity Analysis and Robustness of the Proposed System

Sensitivity analysis is indispensable part of modern control system theory and design applications. It is crucial to choose controller parameters in such a manner that the closed-loop system assures design requirements even though variations in process dynamics occur during operation. A full-bridge inverter is fed by a buck converter-based PV emulator whose output voltage is kept constant at 400 V with P&O MPPT method that is the nominal average DC-bus voltage V_{dc} for the inverter and the inverter filtering inductance L_{inv} is determined as 1 mH. Variations in these parameters are bound to happen due to environmental and process-based factors. Closed-loop transfer function of the proposed PR-P controller inverter system in the s-domain using unity negative feedback can be rewritten replacing the $2V_{dc}$ and L_{inv} in the small-signal transfer function of the inverter obtained in (6.15) with α and β, respectively, as:

$$T(s) = \frac{N(s)}{D(s)} = \frac{(G_{PR}(s)+K_{P(ex)})G_{inv}(s)}{1 + (G_{PR}(s) + K_{P(ex)})G_{inv}(s)}$$

$$= \frac{(1 + \dfrac{\left(\dfrac{\omega_n}{k} + k\omega_n - 2\xi\omega_n\right)s}{s^2 + 2\xi\omega_n s + \omega_n^2} + K_{P(ex)})\dfrac{\alpha}{\beta s}}{1 + (1 + \dfrac{\left(\dfrac{\omega_n}{k} + k\omega_n - 2\xi\omega_n\right)s}{s^2 + 2\xi\omega_n s + \omega_n^2} + K_{P(ex)})\dfrac{\alpha}{\beta s}} \qquad (6.15)$$

Sensitivity of the closed-loop transfer function due to α ($2V_{dc}$) which is the numerator of the inverter transfer function $G_{inv}(s)$ is derived as:

$$S_\alpha^T(s) = \frac{\alpha}{T(s)}\frac{\partial T(s)}{\partial \alpha}\bigg|_{\alpha=800} \qquad (6.16)$$

Substituting (6.15) into (6.16) yields:

$$S_\alpha^T(s) = \frac{\alpha}{N(s)}\frac{\partial N(s)}{\partial \alpha} - \frac{\alpha}{D(s)}\frac{\partial D(s)}{\partial \alpha}\bigg|_{\substack{\alpha=800 \\ \beta=0.001}} \qquad (6.17)$$

Sensitivity of the closed-loop transfer function due to β (L_{inv}) that is the denominator of the inverter transfer function $G_{inv}(s)$ is derived as:

135

$$S_\beta^T(s) = \frac{\beta}{T(s)} \frac{\partial T(s)}{\partial \beta}\bigg|_{\beta=0.001} \tag{6.18}$$

Again, substituting (6.15) into (6.18) yields:

$$S_\beta^T(s) = \frac{\beta}{N(s)} \frac{\partial N(s)}{\partial \beta} - \frac{\beta}{D(s)} \frac{\partial D(s)}{\partial \beta}\bigg|_{\substack{\beta=0.001 \\ \alpha=800}} \tag{6.19}$$

The system sensitivity to variations in α and β in terms of magnitude in dB obtained from (6.17) and (6.19) for varying irradiance is plotted in Figure 6.29. The system is more sensitive to the variations in inverter filtering inductance compared to inverter input voltage, but both meet the requirement that is having small nominal sensitivity peak for low frequencies for better reference tracking and disturbance rejection.
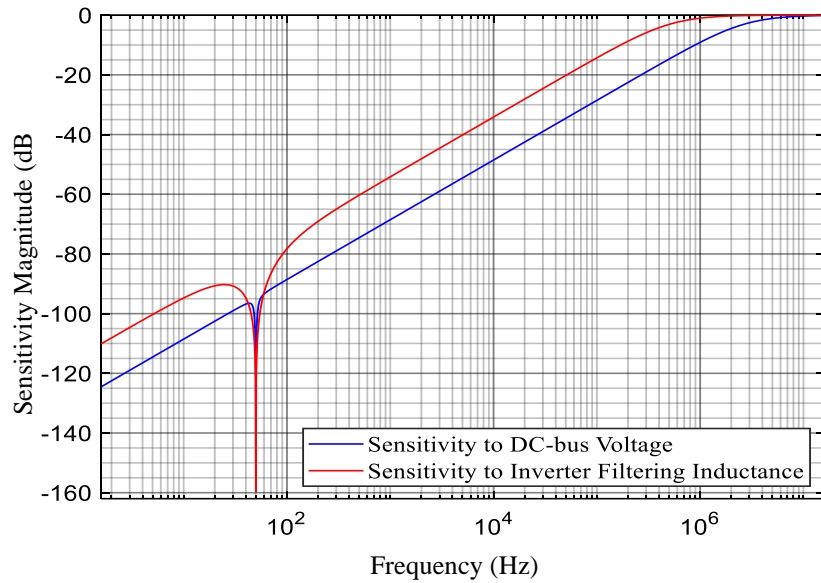
Figure 6.29: System sensitivity to DC-bus voltage and inverter filtering inductance.

A robust system must be capable of meeting requirements that are ensuring the stability of a system and performance measures even in the presence of uncertainties, disturbance, and noise. Sensitivity and complementary sensitivity analysis for overall system are one of the most important useful concepts for a robust control. Nominal sensitivity peak of a system is given as:

$$M_s = \max_{0 \le \omega \le \infty} |S(j\omega)| = \max_{0 \le \omega \le \infty} \left| \frac{1}{1 + G(j\omega)C(j\omega)} \right| \tag{6.20}$$

136

where $G(s)$ and $C(s)$ denote the plant and controller's transfer functions in s-domain for a unity negative feedback control system. Sensitivity and complementary sensitivity functions always and at all frequencies equals 1 for single-input and single-output systems. Accordingly, nominal complementary sensitivity peak of a system is given as:

$$M_{cs} = \max_{0 \leq \omega \leq \infty} |S(j\omega)| = \max_{0 \leq \omega \leq \infty} \left| \frac{G(j\omega)C(j\omega)}{1 + G(j\omega)C(j\omega)} \right| \qquad (6.21)$$

The M_s is closely associated with the robustness of a system as it represents the inverse of the shortest distance from the Nyquist Curve of the loop-transfer function to the critical point -1. The further the loop-transfer function from the critical point in the complex plane the more robust the system is and the more it can handle unmodeled dynamics in the plant. Figure 6.30 indicates the M_s and M_{cs} values of the proposed PR-P current controlled inverter in dB.
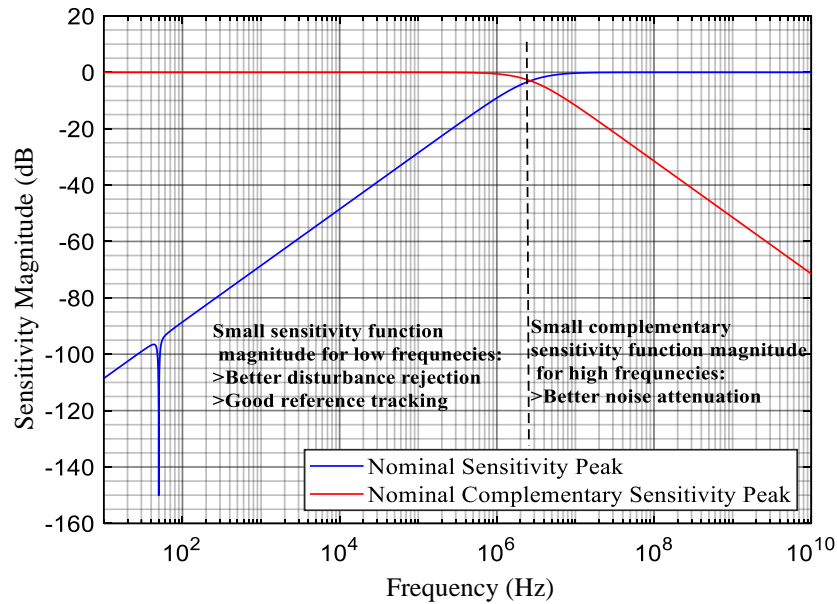
Figure 6.30: Robustness analysis of the system in terms of sensitivity and complementary sensitivity functions.

In addition to have small M_s in low frequencies and small M_{cs} for high frequencies, the peaks at the crossover point of these quantities are not desirable. For satisfactory control systems, the peak value of M_s must be in the range of 1.2-2 and the peak value

of M_{cs} must be in the range of 1-1.5. Regarding this, the proposed system demonstrates very smooth roll-off at the crossover point of the curves.

6.5 Summary

This chapter has presented an alternative unprecedented design process for a Proportional-Resonant (PR) controller with a selective harmonic components (3rd and 5th order) compensator for Photovoltaic Emulator (PVE) supported single phase Grid Connected Inverter (GCI) systems. The design procedure of the proposed controller unity proportional resonant (PR) path is conducted based on notch filter dynamics regulated by symmetrical pole placement methods. Addition of scheduled proportional gain designed by loop shaping method to the resonant path increased the performance of the controller in terms of robustness, achieving better results in the presence of non-linear load and weak grid. The performance of the proposed controller and harmonic compensator is validated employing a PVE consisting of a DC-DC Buck converter, a Maximum Power Point Tracking (MPPT) algorithm and a full-bridge GCI designed using MATLAB/Simulink platforms. Frequency and time domain analysis of the system elements showed satisfactory behaviours of transient and steady-state responses with a high bandwidth which enables them to function with a mutual adaptation to each other. A comparative analysis with different PR controller design techniques used in various papers is performed and resulted in confirming that the proposed technique is robust and simple to implement. The performance of the Proposed PR-P controller with the harmonic compensator is compared with a PI in stationary reference frame and conventional PR current controllers in terms of steady-state error and harmonics mitigation. The simulation results demonstrated that the proposed PR-P controller with harmonic compensator is superior at tracking sinusoidal reference current with zero steady-state error and lower total harmonic distortion with eliminated 3rd and 5th order harmonics.

Chapter 7

Conclusion and Future Work

7.1 Conclusion

In this research design and implementation of control techniques of power electronic interfaces for photovoltaic power systems were reviewed and discussed. Cascade PI controller-based model reference adaptive control, notch filter dynamics-based PR-P controller designed by symmetrical pole placement method, extremum seeking adaptive control and perturb & observe (P&O) methods for various applications have been presented.

A DC-DC boost converter is controlled with Cascade PI Controller-Based Robust Model Reference Adaptive Control (MRAC). The recommended control technique efficiently overcame complexity and challenges by merging parts of a cascade PI control loop with MRAC characteristics. The primary goal of combining MRAC with the cascade PI-controlled boost converter was to maintain consistent performance in the face of uncertainty, changes in plant parameters, and nonlinear dynamics.

The proposed control method boosted tracking speed by two times while simultaneously offering better disturbance rejection, according to the experimental and analytical results.

A variable perturbation size real-time adaptive perturb and observe (P&O) maximum power point tracking (MPPT) algorithm based on the Proportional Gain Resonant and Gain Scheduled Proportional (PR-P) Controller is presented to overcome the limitations of the conventional fixed step size PI controlled P&O MPPT algorithm. Furthermore, for the PR-P controller, an alternate design technique based on shifting notch filter dynamics with placement of complementary poles around the boost converter switching frequency is implemented. The suggested control strategy

overcomes the shortcomings of the traditional P&O MPPT method, such as poor transient responsiveness and large continuous steady-state oscillations, caused using a constant perturbation size. The primary goal of the PR-P controller is to integrate inherited properties of the signal produced by the controller's resonant path to update the best estimated perturbation (ESC model-free adaptive control technique) for use in the P&O algorithm that characterises the overall system learning-based real-time adaptive control (RTA). Furthermore, when compared to commonly used soft computing intelligent systems and adaptive control schemes, the usage of the PR-P controller's internal dynamics overcomes difficulties such as complexity, computational burden, implantation cost, and slow tracking performance. Although proportional-resonant (PR) controllers are most commonly used in DC/AC applications, the results showed that their properties can also be used efficiently in DC/DC systems.

The proposed control technique increased tracking speed by five times, with reduced steady-state oscillations at the maximum power point (MPP) and more than 99 percent energy extraction efficiency, according to the experimental results and analyses.

The current control of an interleaved buck converter-based photovoltaic emulator with a proportional-resonant-proportional (PR-P) controller has been studied. Verification and validation of the designed PR-P controller compared to the PI controller has been presented to illustrate the proposed controller scheme efficiency using robust control theory by considering the most commonly used controller mappings for SMPS with their features, advantages, and limitations. Unlike the traditional gain and phase margin analysis of the system, in which the impacts of gain and phase are analysed separately for the assessment of its robustness, the study considers the combination of gain and phase uncertainty. In order to overcome the main issues in control system design, such as complex dynamics, uncertainty, intentional simplicity, stochastic events, and process variations, disc margin analysis has been performed in addition to the straightforward classical approach (individual gain and phase margins assessment).

Disc margins are used to test the stability of a closed-loop system against gain or phase changes in the open-loop response. The implementation was carried out by adding a multiplicative uncertainty factor F to the buck converter-based PVE feedback loop with a nominal value of 1. Because the disc margin is a parameter that indicates how

much uncertainty the loop can endure before becoming unstable, the system has been enhanced with 50% (increase or decrease) open-loop gain and ±45º phase variation by changing the values of F. The PR-P controller obtained a 13% gain in robust stability margin and a 12º increase in phase toleration, according to the data. Furthermore, the proposed controller has demonstrated superior performance in terms of 10 times faster-converging transient response, zero steady-state error, significant reduction in current ripple, and proper functioning with parameter uncertainty (highly robust), which is a major concern in the load sharing of multi-phase converters. Furthermore, the controller's novel design process decreases computing complexity, improves cost-effectiveness, and simplifies implementation. The PVE's output voltage and current waveforms at various irradiance values accurately follow the I-V characteristics of the emulated PV panel.

An alternative unprecedented design process for a Proportional-Resonant (PR) controller with a selective harmonic components (3rd and 5th order) compensator for Photovoltaic Emulator (PVE) supported single phase Grid Connected Inverter (GCI) systems is presented. The suggested controller's unity proportional resonant (PR) path is designed using notch filter dynamics controlled by symmetrical pole placement methods. The addition of a planned proportional gain developed using the loop shaping method to the resonant path improved the controller's robustness, allowing it to achieve better outcomes in the presence of a nonlinear load and a weak grid.

The system constituents' behaviors were satisfactory when analyzed in the frequency and time domains. A comparison of alternative PR controller design strategies utilized in other studies is conducted, with the proposed technique proving to be both robust and straightforward to apply. In terms of steady-state error and harmonics mitigation, the proposed PR-P controller with the harmonic compensator is compared to a PI in stationary reference frame and standard PR current controllers. The simulation results demonstrated that the proposed PR-P controller with harmonic compensator is better at monitoring sinusoidal reference current with zero steady-state error and lower total harmonic distortion since 3rd and 5th order harmonics are eliminated.

7.2 Future work

- Design and implementation of advanced control techniques comprising a wide variety of methods of power electronic interfaces for photovoltaic power systems will be studied with a detailed comparative analysis of the proposed control schemes presented in this research to illustrate the advantages and drawbacks. According to the results, better control systems will be developed and implemented.

- The performance of developed control techniques will be evaluated by using in a wide range of switch mode power supplies applications in PV systems considering other types of converter such as Buck, Boost, Buck-Boost, Split-pi (Boost-Buck), Ćuk, Sepic, and Charge pump/Switch capacitor.

Chapter 1. References

[1]   R. Ayop and C. W. Tan, "A comprehensive review on photovoltaic emulator," *Renew. Sustain. Energy Rev.*, vol. 80, May, pp. 430–452, 2017, doi: 10.1016/j.rser.2017.05.217.

[2]   S. Seyam, I. Dincer, and M. Agelin-chaab, "Development of a clean power plant integrated with a solar farm for a sustainable community," *Energy Convers. Manag.*, vol. 225, no. June, p. 113434, 2020, doi: 10.1016/j.enconman.2020.113434.

[3]   W. Xiao, *PHOTOVOLTAIC POWER SYSTEMS:Modeling, Design,and Control*, First. Hoboken,NJ,USA: John Wiley & Sons, Incorporated, July, 2017.

[4]   G. Price, *Renewable Power and Energy*, First Edition. New York, USA: Momentum Press, 2018.

[5]   B. Carrera and K. Kim, "Comparison Analysis of Machine Learning Techniques for Photovoltaic Prediction Using Weather Sensor Data," Sensors, vol. 20, no. 11, p. 3129, Jun. 2020.

[6]   L. Li, S. Wen, M. Tseng, and C. Wang, "Renewable energy prediction : A novel short-term prediction model of photovoltaic output power," *J. Clean. Prod.*, vol. 228, pp. 359–375, 2019, doi: 10.1016/j.jclepro.2019.04.331.

[7]   A. M. K. Padiyar, K. R., *Dynamics and Control of Electric Transmission and Microgrids*, First Edition. Honoken. NJ, USA,Wiley, 2018.

[8]   G. P. Systems, A. Sangwongwanich, S. Member, Y. Yang, and S. Member, "Analysis and Modeling of Interharmonics From," *IEEE Trans. Power Electron.*, vol. 33, no. 10, pp. 8353–8364, 2018, doi: 10.1109/TPEL.2017.2778025.

[9]   Y. Yang, K. Zhou, S. Member, and F. Blaabjerg, "Current Harmonics From Single-Phase Grid-Connected Inverters — Examination and Suppression," *IEEE J. Emerg. Sel. Top. Power Electron.*, vol. 4, no. 1, pp. 221–233, 2016, doi: 10.1109/JESTPE.2015.2504845.

[10]   J. Ahmed, S. Member, and Z. Salam, "An Improved Method to Predict the Position of Maximum Power Point During Partial Shading for PV Arrays," no.

December, 2015, doi: 10.1109/TII.2015.2489579.

[11] Z. Zhu and G. Liu, "MPPT Control Method for Photovoltaic System Based on Particle Swarm Optimization and Bacterial Foraging Algorithm Multi-peaks," vol. 4, no. 1, pp. 45–49, 2018, doi: 10.11648/j.ijecec.20180401.15.

[12] J. Macaulay, "A Fuzzy Logical-Based Variable Step Size P & O MPPT Algorithm for Photovoltaic System," *Energies*, vol. 11, no. 6, p. 1340, 2018, doi: 10.3390/en11061340.

[13] G. Bayrak, "An improved step - up converter with a developed real - time fuzzy - based MPPT controller for PV - based residential applications," *Int. Trans. Electr. Energy Syst.*, vol. 29, no. 12, pp. 1–20, Dec. 2019, doi: 10.1002/2050-7038.12140.

[14] P. Kumar, G. Jain, and D. K. Palwalia, "Genetic Algorithm Based Maximum Power Tracking in Solar Power Generation," in *Proc. Int. Conf. Power Adv. Control Eng. (ICPACE),* Aug. 2015, pp. 1–6.

[15] K. Punitha, D. Devaraj, and S. Sakthivel, "Artificial neural network based modified incremental conductance algorithm for maximum power point tracking in photovoltaic system under partial shading conditions," *Energy*, vol. 62, pp. 330–340, 2013, doi: 10.1016/j.energy.2013.08.022.

[16] M. Sam, N. Ali, N. H. Ahmed, A. Junhee, H. Zong, and W. Geem, "Comprehensive Evaluation of Machine Learning MPPT Algorithms for a PV System Under Different Weather Conditions," *J. Electr. Eng. Technol.*, vol. 16, no. 1, pp. 411–427, 2021, doi: 10.1007/s42835-020-00598-0.

[17] M. Seyedmahmoudian and R. Rahmani, "Simulation and Hardware Implementation of New Maximum Power Point Tracking Technique for Partially Shaded PV System Using Hybrid DEPSO Method," *IEEE Trans. Sustain. Energy*, vol. 6, no. 3, pp. 850–862, 2015, doi: 10.1109/TSTE.2015.2413359.

[18] S. Kinattingal, S. P. Simon, and P. S. Rao, "MPPT in PV systems using ant colony optimisation with dwindling population," *IET Renew. Power Gener.*, vol. 14, no. 7, pp. 1105–1112, 2020

[19] C. González-castaño, C. Restrepo, S. Kouro, S. Member, and J. Rodríguez, "MPPT Algorithm Based on Artificial Bee Colony for PV System," Tech. Rep., 2021.

[20] S. Conditions, "An Immune Firefly Algorithm for Tracking the Maximum Power Point of PV Array under Partial," Tech. Rep., 2019.

[21] J. Ahmed and Z. Salam, "A Maximum Power Point Tracking (MPPT) for PV system using Cuckoo Search with partial shading capability," *Appl. Energy*, vol. 119, pp. 118–130, 2014, doi: 10.1016/j.apenergy.2013.12.062.

[22] K. K. T. T. Vignesh, "Soft Computing Techniques for Land Use and Land Cover Monitoring with Multispectral Remote Sensing Images : A Review," *Arch. Comput. Methods Eng.*, vol. 26, no. 2, pp. 275–301, 2019, doi: 10.1007/s11831-017-9239-y.

[23] A. Amir, A. Amir, J. Selvaraj, N. A. Rahim, and A. M. Abusorrah, "Conventional and modi fi ed MPPT techniques with direct control and dual scaled adaptive step-size," *Sol. Energy*, vol. 157, no. August, pp. 1017–1031, 2017, doi: 10.1016/j.solener.2017.09.004.

[24] R. B. Bollipo, S. Mikkili, and P. K. Bonthagorla, "Critical Review on PV MPPT Techniques : Classical , Intelligent and Optimisation," *IET Renew. Power Gener.*, vol. 14, no. 9, pp. 1433–1452, 2020.

[25] A. Ba, C. Ould, M. El, M. Ould, and M. Mahmoud, "Comparative Study of Different DC / DC Power Converter for Optimal PV System Using MPPT (P&O) Method ," *Appl. Sol. Energy (English Transl. Geliotekhnika)*, vol. 54, no. 4, pp. 235–245, 2018, doi: 10.3103/S0003701X18040047.

[26] P. Motsoeneng, "Comparison of Perturb & Observe and Hill Climbing MPPT Schemes for PV Plant Under Cloud Cover and Varying Load," *10th International Renewable Energy Congress (IREC)*, 2019, doi: 10.1109/IREC.2019.8754532.

[27] Z. Zhou, P. M. Holland, and P. Igic, "MPPT algorithm test on a photovoltaic emulating system constructed by a DC power supply and an indoor solar panel," *Energy Convers. Manag.*, vol. 85, pp. 460–469, 2014, doi: 10.1016/j.enconman.2014.06.007.

[28]   M. Shahabuddin, A. Riyaz, M. Asim, M. M. Shadab, A. Sarwar, and A. Anees, "Performance Based Analysis of Solar PV Emulators: A Review," *2018 Int. Conf. Comput. Charact. Tech. Eng. Sci. CCTES 2018*, pp. 94–99, 2019, doi: 10.1109/CCTES.2018.8674082.

[29]   I. Jayawardana, C. N. Man Ho, and M. Pokharel, "Design and Implementation of Switch-mode Solar Photovoltaic Emulator using Power-Hardware-in-the-loop Simulations for Grid Integration Studies," *2019 IEEE Energy Convers. Congr. Expo. ECCE 2019*, pp. 889–894, 2019, doi: 10.1109/ECCE.2019.8912636.

[30]   I. Moussa and A. Khedher, "Photovoltaic emulator based on PV simulator RT implementation using XSG tools for an FPGA control: Theory and experimentation," *Int. Trans. Electr. Energy Syst.*, vol. 29, no. 8, pp. 1–16, 2019, doi: 10.1002/2050-7038.12024.

[31]   R. Ayop and C. W. Tan, "Rapid prototyping of photovoltaic emulator using buck converter based on fast convergence resistance feedback method," *IEEE Trans. Power Electron.*, vol. 34, no. 9, pp. 8715–8723, 2019, doi: 10.1109/TPEL.2018.2886927.

[32]   M. GREEN *et al.*, "Solar cell efficiency tables (version 40)," *Ieee Trans Fuzzy Syst*, vol. 20, no. 6, pp. 1114–1129, 2012, doi: 10.1002/pip.

[33]   I. Moussa, A. Khedher, and A. Bouallegue, "Design of a Low-Cost PV Emulator Applied for PVECS," *Electronics*, vol. 8, no. 2, p. 232, 2019, doi: 10.3390/electronics8020232.

[34]   P. Garg, Priyanshi, and G. Bhuvaneswari, "Power electronic circuit based implementation of a solar PV emulator using a power factor corrected buck converter," *2018 IEEMA Eng. Infin. Conf. eTechNxT 2018*, pp. 1–6, 2018, doi: 10.1109/ETECHNXT.2018.8385297.

[35]   S. M. Azharuddin *et al.*, "A near accurate solar PV emulator using dSPACE controller for real-T ime control," *Energy Procedia*, vol. 61, pp. 2640–2648, 2014, doi: 10.1016/j.egypro.2014.12.266.

[36]   R. González-Medina, I. Patrao, G. Garcerá, and E. Figueres, "A low-cost photovoltaic emulator for static and dynamic evaluation of photovoltaic power converters and facilities," *Prog. Photovoltaics Res. Appl.*, vol. 22, no. 2, pp.

227–241, 2014, doi: 10.1002/pip.2243.

[37] H. Ibrahim and N. Anani, "Variations of PV module parameters with irradiance and temperature," *Energy Procedia*, vol. 134, pp. 276–285, 2017, doi: 10.1016/j.egypro.2017.09.617.

Chapter 2. References

[1] T.-K. Vu and S.-J. Seong, "Comparison of PI and PR Controller Based Current Control Schemes for Single-Phase Grid-Connected PV Inverter," *J. Korea Acad. Coop. Soc.*, vol. 11, no. 8, pp. 2968–2974, 2010.

[2] F. Blaabjerg, R. Teodorescu, S. Member, M. Liserre, A. V Timbus, and S. Member, "Overview of Control and Grid Synchronization for Distributed Power Generation Systems," vol. 53, no. 5, pp. 1398–1409, 2006.

[3] M. Ciobotaru, R. Teodorescu, F. Blaabjerg, and E. Technology, "Control of Single-Stage Single-Phase PV Inverter," *EPE J. (European Power Electron. Drives Journal)*, vol. 16, no. 3, pp. 20–26, 2006, doi: 10.1080/09398368.2006.11463624.

[4] Y. Du and D. D. C. Lu, "Harmonic Distortion Caused by Single-Phase Grid-Connected PV Inverter," in *Power System Harmonics - Analysis, Effects and Mitigation Solutions for Power Quality Improvement*, A. Zobaa, S. H. E. Abdel Aleem, and M. E. Balci, Eds. 2018, pp. 51–63.

[5] C. Khomsi, M. Bouzid, K. Jelassi, and G. Champenois, "Harmonic current conpensation in a single-phase grid connected photovoltaic system sypplying nonlinear load," *2018 9th Int. Renew. Energy Congr. IREC 2018*, no. March, pp. 1–6, 2018.

[6] M. Parvez, M. F. M. Elias, and N. A. Rahim, "Performance analysis of PR current controller for single-phase inverters," *IET Conf. Publ.*, vol. 2016, no. CP688, pp. 1–8, 2016.

[7] D. Zammit, C. Spiteri Staines, M. Apap, and J. Licari, "Design of PR current control with selective harmonic compensators using Matlab," *J. Electr. Syst.*

Inf. Technol., vol. 4, no. 3, pp. 347–358, 2017.

[8] C. Yanarates and Z. Zhou, "Symmetrical Pole Placement Method-Based Unity Proportional Gain Resonant and Gain Scheduled Proportional (PR-P) Controller With Harmonic Compensator for Single Phase Grid-Connected PV Inverters," *IEEE Access*, vol. 9, pp. 93165–93181, 2021.

[9] K. Yang, G. Wu, and X. Zhang, "The control technology of BUCK converter," *Appl. Mech. Mater.*, vol. 150, pp. 240–244, 2012.

[10] D. Rowell, "State-Space Representation of LTI Systems," in *URL: http://web. mit. edu/2.14/www/Handouts/StateSpace. pdf*, October, 2002, pp. 1–18.

[11] G. Herbst, "A Building-Block Approach to State-Space Modeling of DC-DC Converter Systems," *J*, vol. 2, no. 3, pp. 247–267, 2019.

[12] W. M. Polivka, P. R. K. Chetty, and R. D. Middlebrook, "State-Space Average modelling of converters with parasitics and storage-time modulation," *PESC Rec. - IEEE Annu. Power Electron. Spec. Conf.*, vol. 1980-Janua, pp. 119–143, 1980.

[13] P. Azer and A. Emadi, "Generalized state space average model for multi-phase interleaved buck, boost and buck-boost DC-DC converters: Transient, steady-state and switching dynamics," *IEEE Access*, vol. 8, pp. 77735–77745, 2020.

[14] G. Suman, B. V. S. P. Kumar, M. S. Kumar, B. C. Babu, and K. R. Subhashini, "Modeling, analysis and design of synchronous buck converter using state space averaging technique for PV energy system," *Proc. - 2012 Int. Symp. Electron. Syst. Des. ISED 2012*, pp. 281–285, 2012.

Chapter 3. References

[1] R. Ayop and C. W. Tan, "A comprehensive review on photovoltaic emulator," *Renew. Sustain. Energy Rev.*, vol. 80, May, pp. 430–452, 2017, doi: 10.1016/j.rser.2017.05.217.

[2] S. Seyam, I. Dincer, and M. Agelin-chaab, "Development of a clean power plant

integrated with a solar farm for a sustainable community," *Energy Convers. Manag.*, vol. 225, June, p. 113434, 2020,doi: 10.1016/j.enconman.2020.113434.

[3]   S. Paul, T. Dey, P. Saha, S. Dey, and R. Sen, "Review on the development scenario of renewable energy in different country," *2021 Innov. Energy Manag. Renew. Resour. IEMRE 2021*, vol. 2, 2021, doi: 10.1109/IEMRE52042.2021.9386748.

[4]   T. W. John Twidell, *Renewable Energy Resources*, 3rd Edition. New York, USA: Routledge,Taylor&Francis Group, 27 January 2015.

[5]   N. L. Panwar, S. C. Kaushik, and S. Kothari, "Role of renewable energy sources in environmental protection: A review," *Renewable and Sustainable Energy Reviews*, vol. 15, no. 3. pp. 1513–1524, 2011, doi: 10.1016/j.rser.2010.11.037.

[6]   I. J. Hashim, "A New Renewable Energy Index," *2021 6th Int. Conf. Renew. Energy Gener. Appl. ICREGA 2021*, pp. 229–232, 2021, doi: 10.1109/ICREGA50506.2021.9388297.

[7]   E. I. Carroll, "Power electronics for very high power applications," *ABB Rev.*, no. 2, pp. 4–11, 1999.

[8]   S. Natarajan, T. Sudhakar Babu, K. Balasubramanian, U. Subramaniam, and D. J. Almakhles, "A State-of-the-Art Review on Conducted Electromagnetic Interference in Non-Isolated DC to DC Converters," *IEEE Access*, vol. 8, pp. 2564–2577, 2020, doi: 10.1109/ACCESS.2019.2961954.

[9]   E. M. G. Rodrigues, R. Godina, and E. Pouresmaeil, "Industrial applications of power electronics," *Electron.*, vol. 9, no. 9, pp. 1–5, 2020, doi: 10.3390/electronics9091534.

[10]   R. A, "Today ' s and Tomorrow ' s Meaning of Power Electronics within the Grid Interconnection Keywords," *Defense*, pp. 1–11, 2007.

[11]   P. K. Steimer, "Enabled by high power electronics - Energy efficiency, renewables and smart grids," *2010 Int. Power Electron. Conf. - ECCE Asia -, IPEC 2010*, pp. 11–15, 2010, doi: 10.1109/IPEC.2010.5542328.

[12]   A. Q. Huang, S. Bhattacharya, M. Baran, B. Chen, and C. Han, "Active power management of electric power system using emerging power electronics technology," *2007 IEEE Power Eng. Soc. Gen. Meet. PES*, pp. 1–7, 2007, doi: 10.1109/PES.2007.386146.

[13] F. Blaabjerg, K. Ma, and D. Zhou, "Power electronics and reliability in renewable energy systems," *IEEE Int. Symp. Ind. Electron.*, pp. 19–30, 2012, doi: 10.1109/ISIE.2012.6237053.

[14] P. Singh, R. Singh, R. Sharma, and P. Agrawal, "Reliability measures for switched-mode power supplies (SMPS) with redundant fly back transformer," *Proc. - 2016 Int. Conf. Micro-Electronics Telecommun. Eng. ICMETE 2016*, pp. 587–593, 2016, doi: 10.1109/ICMETE.2016.136.

[15] Z. F. P. Supply, A. Rahnamaee, J. Milimonfared, K. Malekian, and M. Abroushan, "Reliability Consideration for a High Power," *13th International Power Electronics and Motion Control Conference (EPE-PEMC)*, pp. 373–379, 2008.

[16] J. Popović-Gerber *et al.*, "Power electronics enabling efficient energy usage: Energy savings potential and technological challenges," *IEEE Trans. Power Electron.*,vol.27, no. 5, pp.2338–2353,2012,doi: 10.1109/TPEL.2011.2171195.

[17] Q. Yin, J. Gan, T. Chen, W. Shi, X. Liu, and Z. Chang, "Research on the flyback switch power supply based on the primary feedback and the valley control," *IEEE 9th Joint International Information Technology and Artificial Intelligence Conference (ITAIC),* vol. 2020, pp. 1312–1315, 2020, doi: 10.1109/ITAIC49862.2020.9338942.

[18] B. M. Hasanien and K. F. A. Sayed, "Current source ZCS PFM DC-DC converter for magnetron power supply," *2008 12th Int. Middle East Power Syst. Conf. ME PCON 2008*, no. 1, pp. 464–469, 2008, doi: 10.1109/MEPCON.2008.4562339.

[19] J. H. Wu, W. He, J. Li, and X. K. Liu, "GaN high frequency small switching power module," *2020 IEEE 2nd Int. Conf. Circuits Syst. ICCS 2020*, no. L, pp. 101–104, 2020, doi: 10.1109/ICCS51219.2020.9336614.

[20] D. Kumar, Amarnath, R. Jain, and R. K. Singh, "Comparison of Non-Isolated Boost Converter & Isolated Flyback Converter for PV Application," *Int. Conf. Innov. Control. Commun. Inf. Syst. ICICCI 2017*, pp. 1–7, 2019, doi: 10.1109/ICICCIS.2017.8660922.

[21] B. M. Reddy and P. Samuel, "A comparative analysis of non-isolated bi-

directional dc-dc converters," *1st IEEE Int. Conf. Power Electron. Intell. Control Energy Syst. ICPEICES 2016*, 2017, doi: 10.1109/ICPEICES.2016.7853292.

[22] A. Alassi, A. Al-Aswad, A. Gastli, L. Ben Brahim, and A. Massoud, "Assessment of isolated and non-isolated DC-DC converters for medium-voltage PV applications," *2017 9th IEEE-GCC Conf. Exhib. GCCCE 2017*, pp. 1–6, 2018, doi: 10.1109/IEEEGCC.2017.8448079.

[23] B. M. Hasaneen and A. A. E. Mohammed, "Design and simulation of DC/DC boost converter," *2008 12th Int. Middle East Power Syst. Conf. MEPCON 2008*, pp. 335–340, 2008, doi: 10.1109/MEPCON.2008.4562340.

[24] S. Banerjee, A. Ghosh, and S. Padmanaban, "Modeling and analysis of complex dynamics for dSPACE controlled closed-loop DC-DC boost converter," *Int. Trans. Electr. Energy Syst.*, vol. 29, no. 4, pp. 1–17, 2019, doi: 10.1002/etep.2813.

[25] H. Li, X. Liu, and J. Lu, "Research on linear active disturbance rejection control in dc/dc boost converter," *Electron.*, vol. 8, no. 11, 2019, doi: 10.3390/electronics8111249.

[26] S. Ahmad and A. Ali, "Active disturbance rejection control of DC–DC boost converter: A review with modifications for improved performance," *IET Power Electron.*, vol. 12, no. 8, pp. 2095–2107, 2019, doi: 10.1049/iet-pel.2018.5767.

[27] Y. Zhang, H. Liu, J. Li, M. Sumner, and C. Xia, "DC-DC Boost Converter with a Wide Input Range and High Voltage Gain for Fuel Cell Vehicles," *IEEE Trans. Power Electron.*, vol. 34, no. 5, pp. 4100–4111, 2019, doi: 10.1109/TPEL.2018.2858443.

[28] A. Özdemir and Z. Erdem, "Double-loop PI controller design of the DC-DC boost converter with a proposed approach for calculation of the controller parameters," *Proc. Inst. Mech. Eng. Part I J. Syst. Control Eng.*, vol. 232, no. 2, pp. 137–148, 2018, doi: 10.1177/0959651817740006.

[29] K. Yang, G. Wu, and X. Zhang, "The control technology of BUCK converter," *Appl. Mech. Mater.*, vol.150, pp. 240–244, 2012, doi: 10.4028/www.scientific.net/AMM.150.240.

[30] D. Rowell, "State-space Representation of LTI Systems," in *URL: http://web. mit. edu/2.14/www/Handouts/StateSpace. pdf*, October, 2002, pp. 1–18.

[31] G. Herbst, "A Building-Block Approach to State-Space Modeling of DC-DC Converter Systems," *J*, vol. 2, no. 3, pp. 247–267, 2019, doi: 10.3390/j2030018.

[32] Q. Xu, N. Vafamand, L. Chen, T. Dragicevic, L. Xie, and F. Blaabjerg, "Review on Advanced Control Technologies for Bidirectional DC/DC Converters in DC Microgrids," *IEEE J. Emerg. Sel. Top. Power Electron.*, vol. 9, no. 2, pp. 1205–1221, 2021, doi: 10.1109/JESTPE.2020.2978064.

[33] A. R. Nikhar, S. M. Apte, and R. Somalwar, "Review of various control techniques for DC-DC interleaved boost converters," *Proc. - Int. Conf. Glob. Trends Signal Process. Inf. Comput. Commun. ICGTSPICC 2016*, pp. 432–437, 2017, doi: 10.1109/ICGTSPICC.2016.7955340.

[34] Mirza Fuad Adnan, Mohammad Abdul Moin Oninda, Mirza Muntasir Nishat, and Nafiul Islam, "Design and Simulation of a DC - DC Boost Converter with PID Controller for Enhanced Performance," *Int. J. Eng. Res.*, vol. V6, no. 09, 2017, doi: 10.17577/ijertv6is090029.

[35] B. Hekimoğlu, S. Ekinci, and S. Kaya, "Optimal PID Controller Design of DC-DC Buck Converter using Whale Optimization Algorithm," *2018 Int. Conf. Artif. Intell. Data Process. IDAP 2018*, September 2018, 2019, doi: 10.1109/IDAP.2018.8620833.

[36] F. Mumtaz, N. Zaihar Yahaya, S. Tanzim Meraj, B. Singh, R. Kannan, and O. Ibrahim, "Sliding Mode Control and Chattering : The Concept," *Ain Shams Eng. J.*, March 2, 2021, doi: 10.1016/j.asej.2021.03.022.

[37] V. Utkin, A. Poznyak, Y. Orlov, and A. Polyakov, "Conventional and high order sliding mode control," *J. Franklin Inst.*, vol. 357, no. 15, pp. 10244–10261, 2020, doi: 10.1016/j.jfranklin.2020.06.018.

[38] H. Fatoorehchi and S. A. Ghorbanian, "Sliding Mode Control for Heartbeat Electrocardiogram Tracking Problem," *Journal of Chemical and Petroleum Engineering*, vol. 53, no. 2, pp. 265–272, 2019, doi: 10.22059/jchpe.2019.286911.1292.

[39] F. M. Zaihidee, S. Mekhilef, and M. Mubin, "Robust speed control of pmsm using sliding mode control (smc)-a review," *Energies*, vol. 12, no. 9, 2019, doi: 10.3390/en12091669.

[40] M. Augustine, "Sliding Mode Control and Chattering : The Concept," Preprint, March 11, 2019, doi: 10.13140/RG.2.2.35872.23042.

[41] Q. Wei, B. Wu, D. Xu, and N. R. Zargari, "Model Predictive Control of Capacitor Voltage Balancing for Cascaded Modular DC-DC Converters," *IEEE Trans. Power Electron.*, vol. 32, no. 1, pp. 752–761, 2017, doi: 10.1109/TPEL.2016.2530869.

[42] F. An, W. Song, K. Yang, N. Hou, and J. Ma, "Improved dynamic performance of dual active bridge dc-dc converters using MPC scheme," *IET Power Electron.*, vol. 11, no. 11, pp. 1756–1765, 2018, doi: 10.1049/iet-pel.2017.0707.

[43] E. Irmak and N. Güler, "A model predictive control-based hybrid MPPT method for boost converters," *Int. J. Electron.*, vol. 107, no. 1, pp. 1–16, 2020, doi: 10.1080/00207217.2019.1582715.

[44] O. Ibrahim, N. Z. Yahaya, and N. Saad, "State-space Modelling and Digital Controller Design for DC-DC Converter," *Telkomnika (Telecommunication Comput. Electron. Control.*, vol. 14, no. 2, pp. 497–506, 2016, doi: 10.12928/TELKOMNIKA.v14i1.3042.

[45] S. Tahir, J. Wang, M. H. Baloch, and G. S. Kaloi, "Digital control techniques based on voltage source inverters in renewable energy applications: A review," *Electron.*, vol. 7, no. 2, 2018, doi: 10.3390/electronics7020018.

[46] J. Freytes, G. Bergna, J. Are Suul, S. D'Arco, H. Saad, and X. Guillaud, "State-space modelling with steady-state time invariant representation of energy based controllers for modular multilevel converters," *2017 IEEE Manchester PowerTech, Powertech 2017*, vol. 2, no. 2, pp. 1–7, 2017, doi: 10.1109/PTC.2017.7981011.

[47] P. Azer and A. Emadi, "Generalized state space average model for multi-phase interleaved buck, boost and buck-boost DC-DC converters: Transient, steady-state and switching dynamics," *IEEE Access*, vol. 8, pp. 77735–77745, 2020, doi: 10.1109/ACCESS.2020.2987277.

[48] Q. A. Tarbosh *et al.*, "Review and Investigation of Simplified Rules Fuzzy Logic Speed Controller of High Performance Induction Motor Drives," *IEEE Access*, vol. 8, pp. 49377–49394, 2020, doi: 10.1109/ACCESS.2020.2977115.

[49] R. Araria, A. Berkani, K. Negadi, F. Marignetti, and M. Boudiaf, "Performance analysis of DC-DC converter and DTC based fuzzy logic control for power management in electric vehicle application," *J. Eur. des Syst. Autom.*, vol. 53, no. 1, pp. 1–9, 2020, doi: 10.18280/jesa.530101.

[50] M. A. Soliman, H. M. Hasanien, H. Z. Azazi, E. E. El-Kholy, and S. A. Mahmoud, "An adaptive fuzzy logic control strategy for performance enhancement of a grid-connected PMSG-Based wind turbine," *IEEE Trans. Ind. Informatics*, vol. 15, no. 6, pp. 3163–3173, 2019, doi: 10.1109/TII.2018.2875922.

[51] N. Santos, J. F. Silva, and V. Soares, "Control of single-phase electrolytic capacitor-less isolated converter for DC low voltage residential networks," *Electron.*, vol. 9, no. 9, pp. 1–19, 2020, doi: 10.3390/electronics9091401.

[52] S. Coman, C. Boldisor, and C. Ciusdel, "Combining the MIT and Lyapunov stability adaptive methods for second order systems," 2018 14th Int. Conf. Dev. Appl. Syst. DAS 2018 - Proc., pp. 31–37, 2018.

[53] P. M, J. Jacob, and P. Joseph K, "Design of model reference adaptive–PID controller for automated portable duodopa pump in Parkinson's disease patients," *Biomed. Signal Process. Control,* vol. 68, March, p. 102590, 2021.

[54] J. Rothe, J. Zevering, M. Strohmeier, and S. Montenegro, "A modified model reference adaptive controller (M-MRAC) using an updated MIT-rule for the altitude of a UAV," *Electron.*, vol. 9, no. 7, pp. 1–15, 2020.

[55] D. Gezer, Y. Taşcıoğlu, and K. Çelebioğlu, "Frequency containment control of hydropower plants using different adaptive methods," *Energies*, vol. 14, no. 8, 2021, doi: 10.3390/en14082082.

[56] M. Swathi and P. Ramesh, "Modeling and analysis of model reference adaptive control by using MIT and modified MIT rule for speed control of DC motor," *Proc. - 7th IEEE Int. Adv. Comput. Conf. IACC 2017*, pp. 482–486, 2017.

[57]   M. I. Mosaad, "Model reference adaptive control of STATCOM for grid integration of wind energy systems," *IET Electr. Power Appl.*, vol. 12, no. 5, pp. 605–613, 2018.

[58]   W. Netto, R. Lakhani, and S. Meenatchi Sundaram, "Design and performance comparison of different adaptive control schemes for pitch angle control in a Twin-Rotor-MIMO-System," *Int. J. Electr. Comput. Eng.*, vol. 9, no. 5, pp. 4114–4129, 2019.

Chapter 4. References

[1]   R. Ayop and C. W. Tan, "A comprehensive review on photovoltaic emulator," *Renew. Sustain. Energy Rev.*, vol. 80, no. May, pp. 430–452, 2017, doi: 10.1016/j.rser.2017.05.217.

[2]   S. Seyam, I. Dincer, and M. Agelin-chaab, "Development of a clean power plant integrated with a solar farm for a sustainable community," *Energy Convers. Manag.*, vol. 225, no. June, p. 113434, 2020, doi: 10.1016/j.enconman.2020.113434.

[3]   W. Xiao, *PHOTOVOLTAIC POWER SYSTEMS:Modeling, Design,and Control*, First Edition. Hoboken, NJ, USA: John Wiley & Sons, Incorporated, 2017.

[4]   G. Price, *Renewable Power and Energy*, First Edition. New York, USA: Momentum Press, 2018.

[5]   B. Carrera and K. Kim, "Comparison Analysis of Machine Learning Techniques for Photovoltaic Prediction Using Weather Sensor Data," *Sensors,* vol. 20, no. 11, p. 3129, Jun. 2020.

[6]   L. Li, S. Wen, M. Tseng, and C. Wang, "Renewable energy prediction : A novel short-term prediction model of photovoltaic output power," *J. Clean. Prod.*, vol. 228, pp. 359–375, 2019, doi: 10.1016/j.jclepro.2019.04.331.

[7]   J. Ahmed, S. Member, and Z. Salam, "An Improved Method to Predict the Position of Maximum Power Point During Partial Shading for PV Arrays," *IEEE Trans. Ind. Informatics*, vol. 11, no. 6, pp. 1378–1387, 2015, doi:

10.1109/TII.2015.2489579.

[8]   Z. Zhu and G. Liu, "MPPT Control Method for Photovoltaic System Based on Particle Swarm Optimization and Bacterial Foraging Algorithm Multi-peaks," *Int. J. Electr. Components Energy Convers.*, vol. 4, no. 1, p. 45, 2018, doi: 10.11648/j.ijecec.20180401.15.

[9]   J. Macaulay, "A Fuzzy Logical-Based Variable Step Size P & O MPPT Algorithm for Photovoltaic System," *Energies*, vol. 11, no. 6, p. 1340, 2018, doi: 10.3390/en11061340.

[10]   G. Bayrak, "An improved step - up converter with a developed real - time fuzzy - based MPPT controller for PV - based residential applications," Int. Trans. Electr. Energy Syst., vol. 29, no. 12, pp. 1–20, Dec. 2019, doi: 10.1002/2050-7038.12140.

[11]   P. Kumar, G. Jain, and D. K. Palwalia, "Genetic Algorithm Based Maximum Power Tracking in Solar Power Generation," in *Proceedings of the 2015 IEEE International Conference on Power and Advanced Control Engineering, ICPACE 2015*, 2015, pp. 1–6, doi: 10.1109/ICPACE.2015.7274907.

[12]   K. Punitha, D. Devaraj, and S. Sakthivel, "Artificial neural network based modified incremental conductance algorithm for maximum power point tracking in photovoltaic system under partial shading conditions," *Energy*, vol. 62, pp. 330–340, 2013, doi: 10.1016/j.energy.2013.08.022.

[13]   M. Sam, N. Ali, N. H. Ahmed, A. Junhee, H. Zong, and W. Geem, "Comprehensive Evaluation of Machine Learning MPPT Algorithms for a PV System Under Different Weather Conditions," *J. Electr. Eng. Technol.*, vol. 16, no. 1, pp. 411–427, 2021, doi: 10.1007/s42835-020-00598-0.

[14]   M. Seyedmahmoudian and R. Rahmani, "Simulation and Hardware Implementation of New Maximum Power Point Tracking Technique for Partially Shaded PV System Using Hybrid DEPSO Method," *IEEE Trans. Sustain. Energy*, vol. 6, no. 3, pp. 850–862, 2015, doi: 10.1109/TSTE.2015.2413359.

[15]   S. Kinattingal, S. P. Simon, and P. S. Rao, "MPPT in PV systems using ant colony optimisation with dwindling population," *IET Renew. Power Gener.*,

vol. 14, no. 7, pp. 1105–1112, 2020, doi: 10.1049/iet-rpg.2019.0875.

[16]   C. González-castaño, C. Restrepo, S. Kouro, S. Member, and J. Rodríguez, "MPPT Algorithm Based on Artificial Bee Colony for PV System," *IEEE Access*, vol. 9, pp. 43121–43133, 2021, doi: 10.1109/ACCESS.2021.3066281.

[17]   S. Conditions, "An Immune Firefly Algorithm for Tracking the Maximum Power Point of PV Array under Partial," *Energies*, vol. 12, no. 16, 2019, doi: 10.3390/en12163083.

[18]   J. Ahmed and Z. Salam, "A Maximum Power Point Tracking (MPPT) for PV system using Cuckoo Search with partial shading capability," *Appl. Energy*, vol. 119, pp. 118–130, 2014, doi: 10.1016/j.apenergy.2013.12.062.

[19]   K. K. T. T. Vignesh, "Soft Computing Techniques for Land Use and Land Cover Monitoring with Multispectral Remote Sensing Images : A Review," *Arch. Comput. Methods Eng.*, vol. 26, no. 2, pp. 275–301, 2019, doi: 10.1007/s11831-017-9239-y.

[20]   A. Amir, A. Amir, J. Selvaraj, N. A. Rahim, and A. M. Abusorrah, "Conventional and modi fi ed MPPT techniques with direct control and dual scaled adaptive step-size," *Sol. Energy*, vol. 157, no. August, pp. 1017–1031, 2017, doi: 10.1016/j.solener.2017.09.004.

[21]   R. B. Bollipo, S. Mikkili, and P. K. Bonthagorla, "Critical Review on PV MPPT Techniques : Classical , Intelligent and Optimisation," *IET Renewable Power Generation*, vol. 14, no. 9. pp. 1433–1452, 2020, doi: 10.1049/iet-rpg.2019.1163.

[22]   A. Ba, C. Ould, M. El, M. Ould, and M. Mahmoud, "Comparative Study of Different DC / DC Power Converter for Optimal PV System Using MPPT(P&O) Method," *Appl. Sol. Energy (English Transl. Geliotekhnika)*, vol. 54, no. 4, pp. 235–245, 2018, doi: 10.3103/S0003701X18040047.

[23]   P. Motsoeneng, "Comparison of Perturb & Observe and Hill Climbing MPPT Schemes for PV Plant Under Cloud Cover and Varying Load,"

10th International Renewable Energy Congress (IREC), 2019, doi: 10.1109/IREC.2019.8754532.

[24] Z. Zhou, P. M. Holland, and P. Igic, "MPPT algorithm test on a photovoltaic emulating system constructed by a DC power supply and an indoor solar panel," *Energy Convers. Manag.*, vol. 85, pp. 460–469, 2014, doi: 10.1016/j.enconman.2014.06.007.

[25] T.-K. Vu and S.-J. Seong, "Comparison of PI and PR Controller Based Current Control Schemes for Single-Phase Grid-Connected PV Inverter," *J. Korea Acad. Coop. Soc.*, vol. 11, no. 8, pp. 2968–2974, 2010, doi: 10.5762/kais.2010.11.8.2968.

[26] F. Blaabjerg, R. Teodorescu, S. Member, M. Liserre, A. V Timbus, and S. Member, "Overview of Control and Grid Synchronization for Distributed Power Generation Systems," *IEEE Transactions on Industrial Electronics*, vol. 53, no. 5. pp. 1398–1409, 2006, doi: 10.1109/TIE.2006.881997.

[27] M. Ciobotaru, R. Teodorescu, F. Blaabjerg, and E. Technology, "Control of Single-Stage Single-Phase PV Inverter," *EPE J. (European Power Electron. Drives Journal)*, vol. 16, no. 3, pp. 20–26, 2006, doi: 10.1080/09398368.2006.11463624.

[28] S. M. Fatemi, M. S. Shadlu, and A. Talebkhah, "A New Method for Maximum Power Point Tracking in Solar PV Systems by Combining Extremum Seeking Method (ESM) and Model Predictive Control (MPC)," *2020 11th Power Electron. Drive Syst. Technol. Conf. PEDSTC 2020*, pp. 5–9, 2020, doi: 10.1109/PEDSTC49159.2020.9088424.

[29] R. Zaitsu and P. M. P. Ppm, "Voltage Mode Boost Converter Small Signal Control Loop Analysis Using the TPS61030," *Converter*, Report, pp. 1–21 (2007).

[30] Texas Instruments, "Working with Boost Converters," *Texas Instruments Appl. Rep*, June 2015, pp. 1-11 [Online]. Available: http://www.ti.com/lit/an/snva731/snva731.pdf, Ed.

[31] V. Michal, "Dynamic duty-cycle limitation of the boost DC/DC converter allowing maximal output power operations," *Int. Conf. Appl. Electron.*, vol. 2016-Septe, no. 2, pp. 177–182, 2016, doi: 10.1109/AE.2016.7577268.

[32]   TI, "How the Switching Frequency Affects the Performance of a Buck Converter," *Texas Instruments Appl. Rep.*, vol. SLVAED3, no. Texas Instruments Incorporated, pp. 1–8, 2019.

Chapter 5. References

[1]   M. Höök and X. Tang, "Depletion of fossil fuels and anthropogenic climate change-A review," *Energy Policy*, vol. 52, pp. 797–809, 2013, doi: 10.1016/j.enpol.2012.10.046.

[2]   J. M. Andujar, F. Segura, and T. Dominguez, "Study of a renewable energy sources-based smart grid. requirements, targets and solutions," *in 2016 3rd Conference on Power Engineering and Renewable Energy (ICPERE)*, 2016, pp. 45–50, doi: 10.1109/ICPERE.2016.7904849.

[3]   D. J. MacKay, Sustainable Energy-Without The Hot Air. Cambridge, England: UIT Cambridge Ltd., 2012.

[4]   M. Shahabuddin, A. Riyaz, M. Asim, M. M. Shadab, A. Sarwar, and A. Anees, "Performance Based Analysis of Solar PV Emulators: A Review," 2018 Int. Conf. Comput. Charact. Tech. Eng. Sci. CCTES 2018, pp. 94–99, 2019, doi: 10.1109/CCTES.2018.8674082.

[5]   N. K. Shrestha and J. Wang, "Water quality management of a cold climate region watershed in changing climate," J. Environ. Informatics, vol. 35, no. 1, pp. 56–80, 2020, doi: 10.3808/jei.201900407.

[6]   N. Ullah, F. Nisar, and A. A. Alahmadi, "Closed Loop Control of Photo Voltaic Emulator Using Fractional Calculus," IEEE Access, vol. 8, pp. 28880–28887, 2020, doi: 10.1109/ACCESS.2020.2971676.

[7]   J. P. Ram, H. Manghani, D. S. Pillai, T. S. Babu, M. Miyatake, and N. Rajasekar, "Analysis on solar PV emulators: A review," Renew. Sustain. Energy Rev., vol. 81, no. July 2017, pp. 149–160, 2018, doi: 10.1016/j.rser.2017.07.039.

[8]   I. Moussa and A. Khedher, "Photovoltaic emulator based on PV simulator RT implementation using XSG tools for an FPGA control: Theory and

experimentation," Int. Trans. Electr. Energy Syst., vol. 29, no. 8, pp. 1–16, 2019, doi: 10.1002/2050-7038.12024.

[9]   L. Ji, G. H. Huang, D. X. Niu, Y. P. Cai, and J. G. Yin, "A stochastic optimization model for carbon-emission reduction investment and sustainable energy planning under cost-risk control," J. Environ. Informatics, vol. 36, no. 2, pp. 107–118, 2020, doi: 10.3808/jei.202000428.

[10]   T. W. John Twidell, Renewable Energy Resources, 3rd Edition. New York, USA: Routledge,Taylor&Francis Group, 2015.

[11]   A. Haque and Zaheeruddin, "Research on solar photovoltaic (PV) energy conversion system: An overview," in IET Conference Publications, 2013, vol. 2013, no. CP646, pp. 605–611, doi: 10.1049/cp.2013.2653.

[12]   A. R. Prasad, S. Singh, and H. Nagar, "Importance of Solar Energy Technologies for Development of Rural Area in India," *Int. J. Sci. Res. Sci. Technol.*, vol. 3, no. 6, pp. 585–599, 2017.

[13]   E. Kabir, P. Kumar, S. Kumar, A. A. Adelodun, and K. H. Kim, "Solar energy: Potential and future prospects," Renew. Sustain. Energy Rev., vol. 82, no. August 2017, pp. 894–900, 2018, doi: 10.1016/j.rser.2017.09.094.

[14]   M. R. S. Shaikh, "A Review Paper on Electricity Generation from Solar Energy," Int. J. Res. Appl. Sci. Eng. Technol., vol. V, no. IX, pp. 1884–1889, 2017, doi: 10.22214/ijraset.2017.9272.

[15]   R. González-Medina, I. Patrao, G. Garcerá, and E. Figueres, "A low-cost photovoltaic emulator for static and dynamic evaluation of photovoltaic power converters and facilities," Prog. Photovoltaics Res. Appl., vol. 22, no. 2, pp. 227–241, 2014, doi: 10.1002/pip.2243.

[16]   R. Ayop and C. W. Tan, "Rapid prototyping of photovoltaic emulator using buck converter based on fast convergence resistance feedback method," IEEE Trans. Power Electron., vol. 34, no. 9, pp. 8715–8723, 2019, doi: 10.1109/TPEL.2018.2886927.

[17]   I. Moussa, A. Khedher, and A. Bouallegue, "Design of a Low-Cost PV Emulator Applied for PVECS," Electronics, vol. 8, no. 2, p. 232, 2019, doi:

10.3390/electronics8020232.

[18]   Z. Zhou, P. M. Holland, and P. Igic, "MPPT algorithm test on a photovoltaic emulating system constructed by a DC power supply and an indoor solar panel," Energy Convers. Manag., vol. 85, pp. 460–469, 2014, doi: 10.1016/j.enconman.2014.06.007.

[19]   P. Garg, Priyanshi, and G. Bhuvaneswari, "Power electronic circuit based implementation of a solar PV emulator using a power factor corrected buck converter," 2018 IEEMA Eng. Infin. Conf. eTechNxT 2018, pp. 1–6, 2018, doi: 10.1109/ETECHNXT.2018.8385297.

[20]   C. Yanarates, Y. Wang, and Z. Zhou, "Unity Proportional Gain Resonant and Gain Scheduled Proportional (PR-P) Controller-Based Variable Perturbation Size Real-Time Adaptive Perturb and Observe (P & O) MPPT Algorithm for PV Systems," IEEE Access, vol. 9, pp. 138468–138482, 2021, doi: 10.1109/ACCESS.2021.3119042 Unity.

[21]   I. Jayawardana, C. N. Man Ho, and M. Pokharel, "Design and Implementation of Switch-mode Solar Photovoltaic Emulator using Power-Hardware-in-the-loop Simulations for Grid Integration Studies," 2019 IEEE Energy Convers. Congr. Expo. ECCE 2019, pp. 889–894, 2019, doi: 10.1109/ECCE.2019.8912636.

[22]   M. GREEN et al., "Solar cell efficiency tables (version 40)," IEEE Trans. Fuzzy Syst., vol. 20, no. 6, pp. 1114–1129, 2012, doi: 10.1002/pip.

[23]   S. M. Azharuddin et al., "A near accurate solar PV emulator using dSPACE controller for real-T ime control," Energy Procedia, vol. 61, pp. 2640–2648, 2014, doi: 10.1016/j.egypro.2014.12.266.

[24]   H. Ibrahim and N. Anani, "Variations of PV module parameters with irradiance and temperature," Energy Procedia, vol. 134, pp. 276–285, 2017, doi: 10.1016/j.egypro.2017.09.617.

[25]   C. Parisi, "Multiphase Buck Design From Start to Finish (Part 1)," no. May, pp. 1–20, 2019, [Online]. Available: www.ti.com.

[26]   D. Baba, "Benefits of a multiphase buck converter," Texas Instruments Application Report, no. 1, pp. 8–13, 2012.

[27] M. Kanzian, H. Gietler, M. Agostinelli, R. Priewasser, and M. Huemer, "Vergleichsstudie digitaler Regelkonzepte für mehrphasige Abwärtswandler," Elektrotechnik und Informationstechnik, vol. 135, no. 1, pp. 54–60, 2018, doi: 10.1007/s00502-017-0574-3.

[28] J. T. Lin, K. Y. Hu, and C. H. Tsai, "Digital multiphase buck converter with current balance/phase shedding control," IEEE Reg. 10 Annu. Int. Conf. Proceedings/TENCON, vol. 2016-Janua, pp. 5–9, 2016, doi: 10.1109/TENCON.2015.7372778.

[29] L. Silva, V. Mendes, S. I. Seleme, and M. Cousineau, "Distributed Control for the Current Balancing of a Multiphase Converter using a Single Voltage Sensor," PCIM Eur. Digit. days 2021; Int. Exhib. Conf. Power Electron. Intell. Motion, Renew. Energy Energy Manag., no. May, pp. 1–7, 2021.

[30] Z. Yuan, P. Wen, H. Xu, and Z. Yuan, "Multi-loop current control strategy based on predictive control for multiphase pulse power supplies," J. Power Electron., vol. 21, no. 3, pp. 553–562, 2021, doi: 10.1007/s43236-020-00210-8.

[31] C. Yanarates and Z. Zhou, "Symmetrical Pole Placement Method-Based Unity Proportional Gain Resonant and Gain Scheduled Proportional (PR-P) Controller With Harmonic Compensator for Single Phase Grid-Connected PV Inverters," IEEE Access, vol. 9, pp. 93165–93181, 2021, doi: 10.1109/access.2021.3092827.

[32] W. Lu, X. Qu, and J. Ma, "Auxiliary bridge arm–based switching control for optimal unloading transient performance of multiphase buck converters," Int. J. Circuit Theory Appl., vol. 48, no. 6, pp. 919–933, 2020, doi: 10.1002/cta.2780.

[33] Q. Xu, N. Vafamand, L. Chen, T. Dragicevic, L. Xie, and F. Blaabjerg, "Review on Advanced Control Technologies for Bidirectional DC/DC Converters in DC Microgrids," IEEE J. Emerg. Sel. Top. Power Electron., vol. 9, no. 2, pp. 1205–1221, 2021, doi: 10.1109/JESTPE.2020.2978064.

[34] A. R. Nikhar, S. M. Apte, and R. Somalwar, "Review of various control techniques for DC-DC interleaved boost converters," Proc. - Int. Conf. Glob. Trends Signal Process. Inf. Comput. Commun. ICGTSPICC 2016, pp. 432–437, 2017, doi: 10.1109/ICGTSPICC.2016.7955340.

[35] Mirza Fuad Adnan, Mohammad Abdul Moin Oninda, Mirza Muntasir Nishat,

and Nafiul Islam, "Design and Simulation of a DC - DC Boost Converter with PID Controller for Enhanced Performance," Int. J. Eng. Res., vol. V6, no. 09, 2017, doi: 10.17577/ijertv6is090029.

[36] B. Hekimoğlu, S. Ekinci, and S. Kaya, "Optimal PID Controller Design of DC-DC Buck Converter using Whale Optimization Algorithm," 2018 Int. Conf. Artif. Intell. Data Process. IDAP 2018, no. September 2018, 2019, doi: 10.1109/IDAP.2018.8620833.

[37] F. Mumtaz, N. Zaihar Yahaya, S. Tanzim Meraj, B. Singh, R. Kannan, and O. Ibrahim, "Sliding Mode Control and Chattering : The Concept," Ain Shams Eng. J., March 2, 2021, doi: 10.1016/j.asej.2021.03.022.

[38] V. Utkin, A. Poznyak, Y. Orlov, and A. Polyakov, "Conventional and high order sliding mode control," J. Franklin Inst., vol. 357, no. 15, pp. 10244–10261, 2020, doi: 10.1016/j.jfranklin.2020.06.018.

[39] H. Fatoorehchi and S. A. Ghorbanian, "Sliding Mode Control for Heartbeat Electrocardiogram Tracking Problem," *Journal of Chemical and Petroleum Engineering*, vol. 53, no. 2, pp. 265–272, 2019, doi: 10.22059/jchpe.2019.286911.1292.

[40] F. M. Zaihidee, S. Mekhilef, and M. Mubin, "Robust speed control of pmsm using sliding mode control (smc)-a review," Energies, vol. 12, no. 9, 2019, doi: 10.3390/en12091669.

[41] M. Augustine, "Sliding Mode Control and Chattering : The Concept," no. March, 2019, doi: 10.13140/RG.2.2.35872.23042.

[42] Q. Wei, B. Wu, D. Xu, and N. R. Zargari, "Model Predictive Control of Capacitor Voltage Balancing for Cascaded Modular DC-DC Converters," IEEE Trans. Power Electron., vol. 32, no. 1, pp. 752–761, 2017, doi: 10.1109/TPEL.2016.2530869.

[43] F. An, W. Song, K. Yang, N. Hou, and J. Ma, "Improved dynamic performance of dual active bridge dc-dc converters using MPC scheme," IET Power Electron., vol. 11, no. 11, pp. 1756–1765, 2018, doi: 10.1049/iet-pel.2017.0707.

[44] E. Irmak and N. Güler, "A model predictive control-based hybrid MPPT method

for boost converters," Int. J. Electron., vol. 107, no. 1, pp. 1–16, 2020, doi: 10.1080/00207217.2019.1582715.

[45] O. Ibrahim, N. Z. Yahaya, and N. Saad, "State-space Modelling and Digital Controller Design for DC-DC Converter," Telkomnika (Telecommunication Comput. Electron. Control., vol. 14, no. 2, pp. 497–506, 2016, doi: 10.12928/TELKOMNIKA.v14i1.3042.

[46] S. Tahir, J. Wang, M. H. Baloch, and G. S. Kaloi, "Digital control techniques based on voltage source inverters in renewable energy applications: A review," Electron., vol. 7, no. 2, 2018, doi: 10.3390/electronics7020018.

[47] J. Freytes, G. Bergna, J. Are Suul, S. D'Arco, H. Saad, and X. Guillaud, "State-space modelling with steady-state time invariant representation of energy based controllers for modular multilevel converters," 2017 IEEE Manchester PowerTech, Powertech 2017, vol. 2, no. 2, pp. 1–7, 2017, doi: 10.1109/PTC.2017.7981011.

[48] P. Azer and A. Emadi, "Generalized state space average model for multi-phase interleaved buck, boost and buck-boost DC-DC converters: Transient, steady-state and switching dynamics," IEEE Access, vol. 8, pp. 77735–77745, 2020, doi: 10.1109/ACCESS.2020.2987277.

[49] Q. A. Tarbosh et al., "Review and Investigation of Simplified Rules Fuzzy Logic Speed Controller of High Performance Induction Motor Drives," IEEE Access, vol. 8, pp. 49377–49394, 2020, doi: 10.1109/ACCESS.2020.2977115.

[50] R. Araria, A. Berkani, K. Negadi, F. Marignetti, and M. Boudiaf, "Performance analysis of DC-DC converter and DTC based fuzzy logic control for power management in electric vehicle application," J. Eur. des Syst. Autom., vol. 53, no. 1, pp. 1–9, 2020, doi: 10.18280/jesa.530101.

[51] M. A. Soliman, H. M. Hasanien, H. Z. Azazi, E. E. El-Kholy, and S. A. Mahmoud, "An adaptive fuzzy logic control strategy for performance enhancement of a grid-connected PMSG-Based wind turbine," IEEE Trans. Ind. Informatics, vol. 15, no. 6, pp. 3163–3173, 2019, doi: 10.1109/TII.2018.2875922.

[52] N. Santos, J. F. Silva, and V. Soares, "Control of single-phase electrolytic capacitor-less isolated converter for DC low voltage residential networks,"

Electron., vol. 9, no. 9, pp. 1–19, 2020, doi: 10.3390/electronics9091401.

Chapter 6. References

[1]   R. Ayop and C. W. Tan, "A comprehensive review on photovoltaic emulator," *Renew. Sustain. Energy Rev.*, vol. 80, May, pp. 430–452, 2017, doi: 10.1016/j.rser.2017.05.217.

[2]   S. Seyam, I. Dincer, and M. Agelin-chaab, "Development of a clean power plant integrated with a solar farm for a sustainable community," *Energy Convers. Manag.*, vol. 225, no. June, p. 113434, 2020, doi: 10.1016/j.enconman.2020.113434.

[3]   W. Xiao, *PHOTOVOLTAIC POWER SYSTEMS:Modeling, Design,and Control*, First Edition. Hoboken, NJ, USA: John Wiley & Sons, Incorporated, 2017.

[4]   G. Price, *Renewable Power and Energy*, First Edition. New York, USA: Momentum Press, 2018.

[5]   B. Carrera and K. Kim, "Comparison Analysis of Machine Learning Techniques for Photovoltaic Prediction Using Weather Sensor Data," Sensors, vol. 20, no. 11, p. 3129, Jun. 2020.

[6]   L. Li, S. Wen, M. Tseng, and C. Wang, "Renewable energy prediction : A novel short-term prediction model of photovoltaic output power," *J. Clean. Prod.*, vol. 228, pp. 359–375, 2019, doi: 10.1016/j.jclepro.2019.04.331.

[7]   A. M. K. Padiyar, K. R., *Dynamics and Control of Electric Transmission and Microgrids*, First Edition. Honoken. NJ, USA,Wiley, 2018.

[8]   G. P. Systems, A. Sangwongwanich, S. Member, Y. Yang, and S. Member, "Analysis and Modeling of Interharmonics From," *IEEE Trans. Power Electron.*, vol. 33, no. 10, pp. 8353–8364, 2018, doi: 10.1109/TPEL.2017.2778025.

[9]   Y. Yang, K. Zhou, S. Member, and F. Blaabjerg, "Current Harmonics From Single-Phase Grid-Connected Inverters — Examination and Suppression," *IEEE J. Emerg. Sel. Top. Power Electron.*, vol. 4, no. 1, pp. 221–233, 2016, doi:

10.1109/JESTPE.2015.2504845.

[10]   W. P. Mohan, N., Undeland, T. M., & Robbins, *Power electronics: Converters, applications, and design*, 3rd Edition. Hoboken, NJ ; : Wiley, 2003.

[11]   J.-M. Hwang, Seon-Hwan & Kim, "Dead Time Compensation Method for Voltage-Fed PWM Inverter.," *Energy Conversion, IEEE Trans.*, vol. 25, no. 1, pp. 1–10, 2010, doi: 10.1109/TEC.2009.2031811.

[12]   IEEE Standards Coordinating Committee 21 on "Fuel Cells Photovoltaics Dispersed Generation and Energy Storage," *IEEE Recommended Practice for Utility Interface of Photovoltaic (PV) Systems*, vol. 2000. 2000.

[13]   M. Shahabuddin, A. Riyaz, M. Asim, M. M. Shadab, A. Sarwar, and A. Anees, "Performance Based Analysis of Solar PV Emulators: A Review," *2018 Int. Conf. Comput. Charact. Tech. Eng. Sci. CCTES 2018*, pp. 94–99, 2019, doi: 10.1109/CCTES.2018.8674082.

[14]   I. Moussa and A. Khedher, "Photovoltaic emulator based on PV simulator RT implementation using XSG tools for an FPGA control: Theory and experimentation," *Int. Trans. Electr. Energy Syst.*, vol. 29, no. 8, pp. 1–16, 2019, doi: 10.1002/2050-7038.12024.

[15]   I. Jayawardana, C. N. Man Ho, and M. Pokharel, "Design and Implementation of Switch-mode Solar Photovoltaic Emulator using Power-Hardware-in-the-loop Simulations for Grid Integration Studies," *2019 IEEE Energy Convers. Congr. Expo. ECCE 2019*, pp. 889–894, 2019, doi: 10.1109/ECCE.2019.8912636.

[16]   S. Silwal and M. Karimi-Ghartemani, "On the design of proportional resonant controllers for single-phase grid-connected inverters," *IEEE Int. Conf. Control Autom. ICCA*, vol. 2016-July, pp. 797–803, 2016, doi: 10.1109/ICCA.2016.7505376.

[17]   A. A. Nazeri, P. Zacharias, F. M. Ibanez, and S. Somkun, "Design of proportional-resonant controller with zero steady-state error for a single-phase grid-connected voltage source inverter with an LCL output filter," *2019 IEEE Milan PowerTech, PowerTech 2019*, pp. 2–7, 2019, doi: 10.1109/PTC.2019.8810554.

[18]   M. Parvez, M. F. M. Elias, and N. A. Rahim, "Performance analysis of PR

current controller for single-phase inverters," *IET Conf. Publ.*, vol. 2016, no. CP688, pp. 1–8, 2016, doi: 10.1049/cp.2016.1311.

[19]   D. Zammit, C. Spiteri Staines, M. Apap, and J. Licari, "Design of PR current control with selective harmonic compensators using Matlab," *J. Electr. Syst. Inf. Technol.*, vol. 4, no. 3, pp. 347–358, 2017, doi: 10.1016/j.jesit.2017.01.003.

[20]   H. Oruganti, S. S. Dash, C. Nallaperumal, and S. Ramasamy, "A Proportional Resonant controller for suppressing resonance in grid tied multilevel inverter," *Energies*, vol. 11, no. 5, 2018, doi: 10.3390/en11051024.

[21]   E. N. Chaves *et al.*, "A Control Strategy Design Applied To Single-Phase Grid-Connected Inverters," *Renew. Energy Power Qual.*, vol. 1, no. 14, pp. 731–735, 2016, doi: 10.24084/repqj14.441.

[22]   T.-K. Vu and S.-J. Seong, "Comparison of PI and PR Controller Based Current Control Schemes for Single-Phase Grid-Connected PV Inverter," *J. Korea Acad. Coop. Soc.*, vol. 11, no. 8, pp. 2968–2974, 2010, doi: 10.5762/kais.2010.11.8.2968.

[23]   T. Sathiyanarayanan and S. Mishra, "ScienceDirect Synchronous Reference Frame Theory based Model Predictive Control for Grid Model Grid Systems Model Grid Systems Systems," *IFAC-PapersOnLine*, vol. 49, no. 1, pp. 766–771, 2016, doi: 10.1016/j.ifacol.2016.03.149.

[24]   R. S. Herrera, P. Salmerón, and H. Kim, "Instantaneous Reactive Power Theory Applied to Active Power Filter Compensation: Different Approaches, Assessment, and Experimental Results," *IEEE Trans. Ind. Electron.*, vol. 55, no. 1, pp. 184–196, 2008, doi: 10.1109/TIE.2007.905959.

[25]   C. Khomsi, M. Bouzid, K. Jelassi, and G. Champenois, "Harmonic current conpensation in a single-phase grid connected photovoltaic system sypplying nonlinear load," *2018 9th Int. Renew. Energy Congr. IREC 2018*, no. March, pp. 1–6, 2018, doi: 10.1109/IREC.2018.8362520.

[26]   A. Kulkarni and V. John, "Mitigation of lower order harmonics in a grid-connected single-phase PV inverter," *IEEE Trans. Power Electron.*, vol. 28, no. 11, pp. 5024–5037, 2013, doi: 10.1109/TPEL.2013.2238557.

[27] S. Pradhan, S. Member, I. Hussain, B. Singh, B. K. Panigrahi, and S. Member, "Performance Improvement of Grid Integrated Solar PV System using DNLMS Control Algorithm," *IEEE Trans. Ind. Appl.*, vol. 55, no. 1, pp. 78–91, 2019, doi: 10.1109/TIA.2018.2863652.

[28] C. Khomsi, M. Bouzid, K. Jelassi, and G. Champenois, "Harmonic Current Conpensation in a Single-Phase Grid Connected Photovoltaic System Sypplying Nonlinear Load," *2018 9th Int. Renew. Energy Congr. IREC 2018*, no. March, pp. 1–6, 2018, doi: 10.1109/IREC.2018.8362520.

[29] J. A. Suul, K. Ljøkelsøy, T. Midtsund, and T. Undeland, "Synchronous Reference Frame Hysteresis Current Control for Grid Converter Applications," *IEEE Trans. Ind. Appl.*, vol. 47, no. 5, pp. 2183–2194, 2011, doi: 10.1109/TIA.2011.2161738.

[30] U. Tamrakar *et al.*, "Comparative analysis of current control techniques to support virtual inertia applications," *Appl. Sci.*, vol. 8, no. 12, 2018, doi: 10.3390/app8122695.

[31] H. Mohomad, S. A. Saleh, and L. Chang, "Disturbance Estimator-Based Predictive Current Controller for Single-Phase Interconnected PV Systems," *IEEE Trans. Ind. Appl.*, vol. 53, no. 5, pp. 4201–4209, 2017, doi: 10.1109/TIA.2017.2716363.

[32] H. M. A. R, S. A. Saleh, R. Shao, and L. Chang, "Robust Current Controller for Grid-Connected Voltage Source Inverter." *2017 IEEE 8th International Symposium on Power Electronics for Distributed Generation Systems, PEDG (2017)*

[33] F. Blaabjerg, R. Teodorescu, S. Member, M. Liserre, A. V Timbus, and S. Member, "Overview of Control and Grid Synchronization for Distributed Power Generation Systems," *IEEE Transactions on Industrial Electronics*, vol. 53, no. 5. pp. 1398–1409, 2006, doi: 10.1109/TIE.2006.881997.

[34] M. Ciobotaru, R. Teodorescu, F. Blaabjerg, and E. Technology, "Control of Single-Stage Single-Phase PV Inverter," *EPE J. (European Power Electron. Drives Journal)*, vol. 16, no. 3, pp. 20–26, 2006, doi:

10.1080/09398368.2006.11463624.

[35] Y. Du and D. D. C. Lu, "Harmonic Distortion Caused by Single-Phase Grid-Connected PV Inverter," in *Power System Harmonics - Analysis, Effects and Mitigation Solutions for Power Quality Improvement*, A. Zobaa, S. H. E. Abdel Aleem, and M. E. Balci, Eds. 2018, pp. 51–63.

[36] M. Castilla, J. Miret, J. Matas, L. G. De Vicuña, J. M. Guerrero, and S. Member, "Control Design Guidelines for Single-Phase Grid-Connected Photovoltaic Inverters With Damped Resonant Harmonic Compensators," *IEEE Trans. Ind. Electron.*, vol. 56, no. 11, pp. 4492–4501, 2009, doi: 10.1109/TIE.2009.2017820.

[37] A. I. Bacha, Seddik, Munteanu, Iulian, Bratcu, *Power Electronic Converters Modeling and Control with Case Studies, Advanced Textbooks in Control and Signal Processing*. London: Springer Science & Business Media, 2014.

[38] S. Silwal, S. Member, S. Taghizadeh, and S. Member, "An Enhanced Control System for Single-Phase Inverters Interfaced With Weak and Distorted Grids," *IEEE Trans. Power Electron.*, vol. 34, no. 12, pp. 12538–12551, 2019, doi: 10.1109/TPEL.2019.2909532.

[39] T. Davi, C. Busarello, and M. G. Simões, "Design Procedure for a Digital Proportional-Resonant Current Controller in a Grid Connected Inverter," IEEE 4th Southern Power Electronics Conference, SPEC 2018.

[40] D. Zammit, C. S. Staines, M. Apap, and J. Licari, "Design of PR current control with selective harmonic compensators using Matlab," *J. Electr. Syst. Inf. Technol.*, vol. 4, no. 3, pp. 347–358, 2017, doi: 10.1016/j.jesit.2017.01.003.

[41] R. B. Bollipo, S. Mikkili, and P. K. Bonthagorla, "Critical Review on PV MPPT Techniques : Classical , Intelligent and Optimisation," *IET Renewable Power Generation*, vol. 14, no. 9. pp. 1433–1452, 2020, doi: 10.1049/iet-rpg.2019.1163.

[42] G. Bayrak, "An improved step - up converter with a developed real - time fuzzy

- based MPPT controller for PV - based residential applications," *Int. Trans. Electr. Energy Syst.*, vol. 29, no. 12, pp. 1–20, Dec. 2019, doi: 10.1002/2050-7038.12140.

[43]   A. Ba, C. Ould, M. El, M. Ould, and M. Mahmoud, "Comparative Study of Different DC / DC Power Converter for Optimal PV System Using MPPT (P & O) Method ," *Appl. Sol. Energy (English Transl. Geliotekhnika)*, vol. 54, no. 4, pp. 235–245, 2018, doi: 10.3103/S0003701X18040047.

[44]   M. A. Ghasemi, "MPPT Method for PV Systems Under Partially Shaded Conditions by Approximating I – V Curve," *IEEE Trans. Ind. Electron.*, vol. 65, no. 5, pp. 3966–3975, 2018, doi: 10.1109/TIE.2017.2764840.

[45]   A. Lashab, S. Member, D. Sera, and S. Member, "A Dual-Discrete Model Predictive Control-Based MPPT for PV Systems," *IEEE Trans. Power Electron.*, vol. 34, no. 10, pp. 9686–9697, 2019, doi: 10.1109/TPEL.2019.2892809.

[46]   A. Amir, A. Amir, J. Selvaraj, N. A. Rahim, and A. M. Abusorrah, "Conventional and modi fi ed MPPT techniques with direct control and dual scaled adaptive step-size," *Sol. Energy*, vol. 157, no. August, pp. 1017–1031, 2017, doi: 10.1016/j.solener.2017.09.004.

[47]   R. González-Medina, I. Patrao, G. Garcerá, and E. Figueres, "A low-cost photovoltaic emulator for static and dynamic evaluation of photovoltaic power converters and facilities," *Prog. Photovoltaics Res. Appl.*, vol. 22, no. 2, pp. 227–241, 2014, doi: 10.1002/pip.2243.

[48]   S. M. Azharuddin *et al.*, "A near accurate solar PV emulator using dSPACE controller for real-T ime control," *Energy Procedia*, vol. 61, pp. 2640–2648, 2014, doi: 10.1016/j.egypro.2014.12.266.

[49]   R. Ayop and C. W. Tan, "A novel photovoltaic emulator based on current-resistor model using binary search computation," *Sol. Energy*, vol. 160, no. July 2017, pp. 186–199, 2018, doi: 10.1016/j.solener.2017.12.005.

[50]   J. P. Ram, H. Manghani, D. S. Pillai, T. S. Babu, M. Miyatake, and N. Rajasekar, "Analysis on solar PV emulators: A review," *Renew. Sustain. Energy*

Rev., vol. 81, no. January, pp. 149–160, 2018, doi: 10.1016/j.rser.2017.07.039.

[51] J. P. Ram, H. Manghani, D. S. Pillai, T. S. Babu, M. Miyatake, and N. Rajasekar, "Analysis on solar PV emulators: A review," *Renew. Sustain. Energy Rev.*, vol. 81, no. July 2017, pp. 149–160, 2018, doi: 10.1016/j.rser.2017.07.039.

[52] H. Patel and V. Agarwal, "MATLAB-based modeling to study the effects of partial shading on PV array characteristics," *IEEE Trans. Energy Convers.*, vol. 23, no. 1, pp. 302–310, 2008, doi: 10.1109/TEC.2007.914308.

[53] I. Moussa, A. Khedher, and A. Bouallegue, "Design of a Low-Cost PV Emulator Applied for PVECS," *Electronics*, vol. 8, no. 2, p. 232, 2019, doi: 10.3390/electronics8020232.

[54] P. Motsoeneng, "Comparison of Perturb & Observe and Hill Climbing MPPT Schemes for PV Plant Under Cloud Cover and Varying Load," *10th International Renewable Energy Congress (IREC)*, 2019, doi: 10.1109/IREC.2019.8754532.